CHARACTERIZATION OF BETA PHASE GROWTH AND EXPERIMENTAL VALIDATION OF LONG TERM THERMAL EXPOSURE SENSITIZATION OF AA5XXX ALLOYS

by

Yakun Zhu

A dissertation submitted to the faculty of
The University of Utah
in partial fulfillment of the requirements for the degree of

Master of Science

Department of Metallurgical Engineering

The University of Utah

May 2013

The University of Utah Graduate School

STATEMENT OF THESIS APPROVAL

The thesis of Yakun Zhu

has been approved by the following supervisory committee members:

Michael L. Free	, Chair	August 21, 2012 Date Approved
Hong Yong Sohn	, Member	August 21, 2012 Date Approved
Manoranjan Misra	, Member	August 21, 2012 Date Approved

and by Jan D. Miller , Chair of

the Department of Metallurgical Engineering

and by Donna M. White, Interim Dean of The Graduate School.

ABSTRACT

The United States Navy has a need for fast, light-weight ships to provide rapid deployment in its operations. Strong and corrosion-resistant aluminum alloys, such as AA5083 (UNS A95083) as well as other AA5XXX alloys, have properties that are well-suited for such applications. However, AA5XXX alloys are susceptible to intergranular corrosion (IGC) and stress corrosion cracking (SCC) because of sensitization which is a consequence of the formation of the grain boundary β-phase, Al_3Mg_2, and the anodic dissolution of the β-phase. Significant research has been performed to measure and understand the effects of time, temperature, stress, and sea water on sensitization and associated intergranular corrosion and stress corrosion cracking under steady-state conditions.

In the present work, the behaviors of β-phase nucleation and growth were characterized using optical and electron microscopy, the relationship between preexisting particles and β-phase, as well as the effect of different heat treatment times and temperatures on IGC and SCC susceptibility of 5XXX alloys were investigated. Grain boundary β-phase thickness was measured with high resolution transmission electron microscopy (TEM). The corrosion sensitization susceptibility was evaluated according to

the American Society for Testing and Materials (ASTM) standard G67 tests, that is, nitric acid mass-loss testing (NAMLT).

Diffusion of Mg is manifested by the thickening of β-phase along the grainboundary because the grain boundary is considered as the preferential site for β-phase nucleation. The β-phase growth rate was monitored using high resolution TEM.

The variety of precipitates and their subsequent effects on β-phase nucleation and growth kinetics was investigated. The existence of various intermetallic particles was observed in both baseline and thermally exposed (70°C and 175°C) samples. These particles are usually either rod-shaped or equiaxed, and rich in Mn, Fe, and Cr. Indexing of lattice planes observed in a few of these particles suggested the composition is Al_6Mn or Al_6(Mn, Fe, Cr). This research also shows that the β-phase precipitation occurs between the preexisting Mn rich particles.

The basic model for the determination of diffusivity values, the prediction of β-phase thickness growth, and corrosion sensitization prediction have been improved by new data from this research.

TABLE OF CONTENTS

LIST OF TABLES

LIST OF FIGURES

Figure **Page**

ACKNOWLEDGEMENTS

The work presented in this thesis was carried out in the Department of Metallurgical Engineering, The University of Utah, under the supervision of Dr. Michael L. Free. Thanks to the Office of Naval Research for providing funding under Award Number: N000140810178.

Firstly, I would like to give great thanks to my supervisor, Prof. Michael L. Free, for the chance to work on this project, and for his help, support, discussions, and encouragement over the last two years. Working with him is my great opportunity to learn that enthusiasm and devotion are a key to success. I would also like to thank Prof. H. Y. Sohn and Prof. Manoranjan Misra for their guidance for the completion of my thesis.

I would like to thank my senior lab mate, Dr. Soumya Kar, for his encouragement, training, invaluable suggestions, and discussion throughout this whole project.

Microscopy research at the Oak Ridge National Laboratory's High Temperature Materials Laboratory was sponsored by the U.S. Department of Energy, Office of Energy Efficiency and Renewable Energy, Vehicle Technologies Program. Great thanks should

be delivered to Dr. David Cullen, Dr. Larry Allard, and Dr. Karen More for the success of the TEM imaging work and the subsequent data processing.

Thanks also to Dr. Kurt A. Langworthy at the University of Oregon, Dr. Brian van Devener at The University of Utah, and Dr. Jeff Farrer at Brigham Young University for their support and discussion on TEM imaging work.

Thanks also to everyone in Dr. Free's group, for their encouragement, discussions, and suggestions throughout my master's thesis project.

Last but not least, I would like to express sincere appreciation and love to my grandparents, my parents, and my sister, and my aunts and uncles, as well as all the other family members for their support and encouragement along all the years of my education.

CHAPTER 1

INTRODUCTION

1.1 Background

The United States Navy has an urgent need for fast, light-weight ships, such as the Littoral Combat Ship (LCS), shown in Figure 1.1, to provide rapid deployment in its operations. Strong, ductile, and corrosion-resistant aluminum alloys, AA5083 (UNS A95083) as well as other AA5XXX alloys, for instance, have demonstrated properties that are well-suited for such applications [1-2].

However, AA5XXX alloys are susceptible to sensitization in which Mg diffuses from the bulk to grain boundaries. The process is shown in Figure 1.2. This process results in β-phase (Al_3Mg_2) formation that makes these alloys vulnerable to intergranular corrosion (IGC) and stress corrosion cracking (SCC) [3-5], which will be discussed in detail later. With a corrosion potential of around -1.29V (SCE), the β-phase is typically more active than the 5083 Al matrix, which has a potential of -0.73V (SCE). The β-phase is thus, preferentially attacked by corrosive environments, which results in anodic dissolution of β-phase from the grain boundaries [4, 6-8].

Considerable research has been conducted to understand the mechanism behind

the β-phase-related corrosion phenomena [4-14], but most of these studies were based on elevated temperatures that are much higher than actual application temperatures. It is well accepted that the decomposition of Al-Mg supersaturated solid-solution follows a four-stage process: solid solution to Guinier-Preston (GP) zones to β″ to β′ to β [15-16]. In Al-Mg alloy aged between 100°C and 250°C, the β′-phase forms first around 100°C and β-phase appears around 200°C in the matrix of the nearly complete depletion of Mg [17-18]. However, it has been observed that β-phase precipitates below 200°C [9-12]. In addition, there is a controversy regarding whether defects, such as dislocations, provide nucleation sites for β′-phase precipitation [19-20].

1.2 Objectives

We have developed a deterministic mathematical model that predicts the degree of sensitization as measured by ASTM G-67 as a function of exposure temperature and time. This model produces excellent predictions of sensitization at elevated temperatures and short exposure times for 5083-H131. It is based primarily on exposures between 100°C and 175°C for 1 to 200 hours. Extrapolation of the existing model shows reasonable data fitting at longer times (2,500 hours) and lower temperatures (70°C) based on a limited set of samples. However, for the predictions of much longer times (20,000 hours) and much lower temperatures (40-70°C), there is a limitation on the existing model. Therefore, more work needs to be performed on much longer times and much lower temperatures. In our present work, we will focus on several areas of research: 1)

the properties of β-phase precipitation and growth; 2) the variety of precipitates and their subsequent effects on β-phase nucleation and growth kinetics; 3) the effects of alloying composition, processing, and variability on the degree of sensitization of 5XXX aluminum alloys; 4) improvement of the long-term, low-temperature sensitization prediction accuracy of the existing model using long-term, low-temperature testing data; 5) improvement of the understanding of beta phase properties and the effects of these properties on sensitization as well as the incorporation of these effects in the existing model.

Figure 1.1 Littoral Combat Ship (LCS).

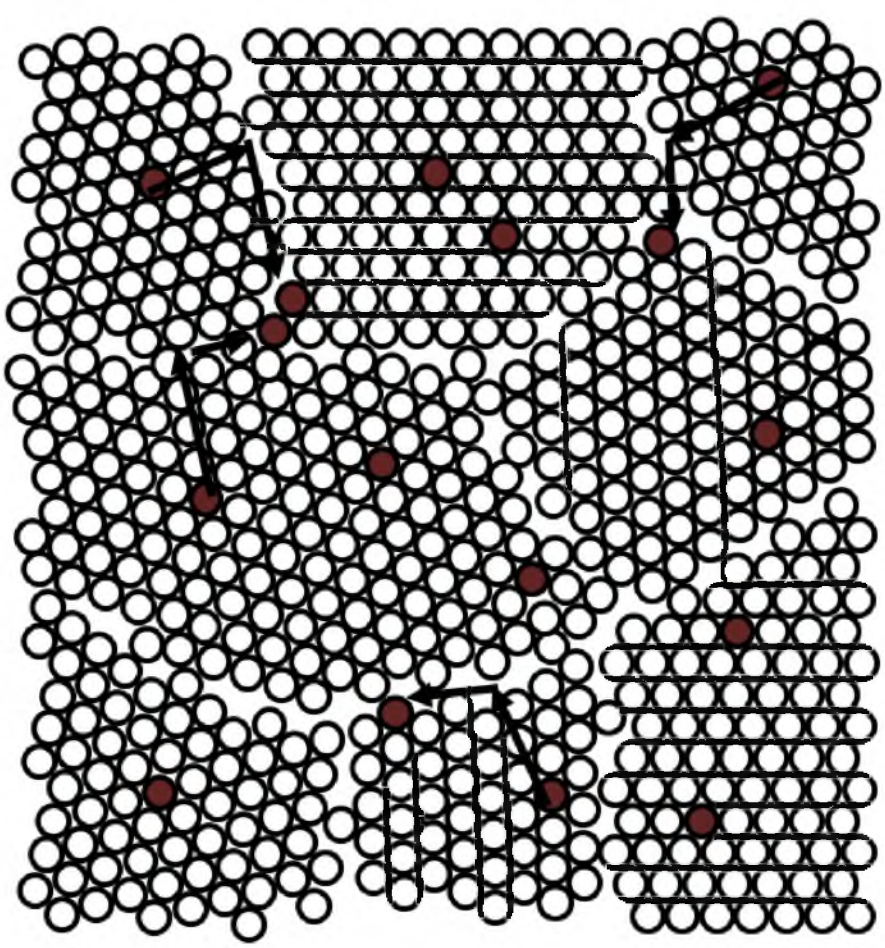

Figure 1.2 Grain boundaries form natural paths for easy magnesium diffusion. Magnesium (red circles) can diffuse and form compounds along grain boundaries. Aluminum atoms are represented by open circles.

CHAPTER 2

REVIEW OF THE LITERATURE

2.1 Introduction

This chapter begins with a short introduction to the 5XXX aluminum alloys. Secondly, the precipitation mechanism and growth kinetics of β-phase in Al-Mg alloys as a function of time, temperature, alloying elements, temper states, as well as other factors affecting the nucleation and growth will be presented in detail. In the third section, the types of corrosion of Al-Mg alloys will be reviewed. This chapter will conclude with a discussion of the corrosion mechanism and testing method with respect to each type of corrosion.

2.2 5XXX Aluminum Alloys

The compositions (wt. %) of two common 5XXX alloys, AA5083 and AA5456, are given in Table 2.1 [21]. As we can see from the table, the three primary components of 5XXX alloys are aluminum (Al), magnesium (Mg), and manganese (Mn). The AA5XXX alloys attribute their strength primarily to cold-working and secondarily to solid-solution-strengthening by the dissolution of Mg in Al matrix and, to a lesser extent, to dispersion-hardening by Al_6Mn particles [22-23].

2.3 β-phase Precipitation

2.3.1 Phase Diagram

Most AA5XXX alloys are produced keeping the Mg in supersaturated solid solution (SSSS), where more Mg is in solution in the alloy than is thermodynamically stable at service temperatures. The Al-Mg binary phase diagram is shown in Figure 2.1 [24]. The area in the solid-red box presents Mg concentration in commercial alloys, typically in the range of 4.0 - 4.5 wt. %. Temperatures experienced by the alloys for this range of Mg concentration are well below the solvus line, indicating that both α- and β-phases are present when the system is at equilibrium. That means Mg needs to diffuse out of the bulk and β-phase precipitates when the temperature is below 200-240°C. These low to modest temperatures are readily experienced by the components of ships in service, which contributes to the susceptibility of IGC and SCC over the entire life of the ship [25-26]. The precipitation of β-phase occurs primarily along grain boundaries because of a low diffusion barrier due to the presence of defects, such as dislocations, vacancies, and faults at grain boundary areas [27-28].

2.3.2 Precipitation Sequence

However, the kinetics of β-phase precipitation is quite complex, especially the precipitation process at low temperatures [29]. It is well accepted that the decomposition of Al-Mg SSSS follows a four-stage process [15-16, 30-34]:

$$\text{GP zones} \rightarrow \beta''\text{-phase} \rightarrow \beta'\text{-phase} \rightarrow \beta\text{-phase},$$

where β″ is an $L1_2$ ordered phase (composition Al_3Mg) [34], β′ is a semicoherent hexagonal intermediate phase (approximate composition Al_3Mg_2) with lattice parameters a = 1.002 nm and c = 1.636 nm [32, 35].

Although considerable research has been conducted regarding precipitation in binary Al-Mg alloy systems, several questions remain to be solved, including the nucleation of β′/β, the kinetics of β′/β formation, and the transformation from β′ to β, and the time and temperature dependences of β′/β formation.

Kurtasova *et al.* reported that GP zones forms under natural aging below 50°C [36], which is followed by the formation of a metastable $L1_2$ structure of β″-phase out of GP zones at longer times. β′-phase will precipitate at even longer aging times and equilibrium β-phase precipitation in the end [26, 37]. The β′-phase and β-phase can precipitate directly from the Al matrix at temperatures above 100°C because of enhanced diffusion according to the research conducted by Kurtasova [36]. The reason why β′-phase precipitates need higher temperature and longer time compared to GP zones is that it has a large unit cell [26, 29, and 38]. The precipitation preferentially occurs at triple points, α/Al_6Mn boundaries, and grain boundaries, where enough dislocations are available to accommodate the semicoherent β′-phase [25, 37]. As β′ particles coarsen, Mg around grain boundary areas is gradually depleted[36] and it is difficult for the continued growth because of the diffusion distance for Mg to travel from bulk to grain boundaries [39]. Therefore, the transformation from semicoherent β′-phase to noncoherent β-phase becomes favored due to increased misfit between β′-phase and matrix, and due to lower Mg concentration in

β-phase compared to β′-phase [37]. It is also reported that this phase transformation occurs around 200°C in the matrix of the nearly complete Mg depletion [17-18].

2.3.3 Effects of Dislocation on Precipitation

Itoh *et al.* concluded, based on a TEM study on precipitation in Al-8.3 wt. % Mg alloy, that nucleation of β′ did not occur on dislocation loops. Instead, the nucleation on tetrahedron shaped voids was observed [40]. This is in agreement with the work conducted by Eikum and Thomas [41]. However, this view is at odds with the TEM study performed by Bouchear *et al.* in Al-8.8 wt. % Mg and Al-9.9 wt. % alloys in which β′ precipitated around dislocation loops [16], which is in agreement with the work done by Embury and Nicholson [19].

2.3.4 Time and Temperature Dependence of Precipitation

In AA5083, Goswami *et al.* concluded that no GP zones, β″, or β′ precipitates form based on TEM imaging of the as-received samples or the samples heat treated at 175°C for 10 days [42]. It is believed, however, that heat treatment time and temperature do have an effect on the compositions of precipitates along grain boundary areas. Heat treatment performed at low temperatures may produce a more varied composition at the grain boundaries than what is reported by Goswami *et al.* because of the formation of GP zones and metastable phases; β″, for example, at low temperatures [18].

The continuous/semicontinuous film formed with the increase in sensitization time. At even longer times, hundreds of days, for example, the amount of intragranular

β-phase increases rapidly, which enhances the corrosion resistance of that alloy based on C-shaped time/temperature diagram[43]. It is also reported that the corrosion resistance is also increased to some extent through Ostwald ripening of grain boundary precipitates which may destroy the continuous diffusion path along grain boundaries [44].

In addition, heat treatment temperature also influences precipitation behavior very much. When the temperature is above 100°C, the precipitation rate is increased because of increased diffusivity. At even higher temperature, above 200°C, for example, globular-shaped β-phase forms throughout the structure [45]. On one hand, the precipitation process is accelerated by dislocations. On the other hand, dislocations may be recovered at higher temperatures, which in turn reduces the precipitation rate [45].

2.3.5 Effect of Alloying Additions on Precipitations

Research has been extensively performed to see if minor alloying additions can modify or even change the precipitation behaviors of β-phase along grain boundary areas in AA5XXX alloy systems. An early study by Yukawa *et al.*[44] based on the measurement of Mg concentration near β-phase in Al-8 wt. % Mg system with and without 0.13 wt. % Cu or 0.11 wt. % Zn additions, revealed that Cu addition did not modify the steep Mg concentration profile near β-phase. Zn addition, however, made the concentration profile of Mg gentler. D.O. Sprowls *et al.* found that a level of 1-2 wt. % Zn additions to Al-Mg alloys accelerated the rate of precipitates within the grains, and thus reduced the amount of β-phase along grain boundary areas [29].

The addition of Zn up to 0.68 - 0.70 wt. % to one AA5083 alloy was investigated by Carroll *et al.* They found that one ternary phase, $Mg_{32}(Al, Zn)_{49}$, formed along grain/subgrain boundaries instead of β-phase precipitation [4]. Further research showed that with the addition of Cu even in a very minor amount, 0.073 wt. %, for example, Zn in the above ternary phase was replaced by Cu [46-47]. The crystal structure of this Cu-containing phase is not only limited to BCC matrix structure, but also precipitated as icosahedral quasicrystalline phase [46].

Al_6Mg_4Cu was claimed to form by Tsuchida *et al.* with the addition of Cu alone, and it seems to make the distribution of β precipitates more homogeneous in the matrix [48].

In summary, the addition of minor alloying elements to AA5083 alloys changes the precipitation behavior of β-phase in the matrix.

2.4 Corrosion of Al and Al-Mg Alloys

2.4.1 Thermodynamics of Al and Mg in Aqueous Environments

Although Al is thermodynamically reactive and very easily oxidized, this metal has excellent corrosion resistance because of a thin oxide film which forms on its surface. This oxide film is only around 1 nm thick but is very resistant to corrosion and can reform immediately in many environments if damaged [49]. It has been reported that several factors influence the oxide structure, including material composition, crystal structure, the degree of noncrystallinity of the oxide, and presence and distribution of

microdefects (vacancies, voids, etc.) as well as macrodefects (inclusions, second phase particles, etc.) [50].

As can be seen in Figure 2.2, aluminum generally dissolves as Al^{3+} ions in acidic environments and as AlO^{2-} ions in alkaline environments [51]. Beyond the range of passivation, aluminum corrodes due to the solubility of its oxides in many acids and bases, producing $A1^{3+}$ ions, and $Al(OH)^{4-}$ ions respectively. The following is a list of main reactions that occur with respect to corrosion:

Dissolution: $Al \rightarrow A1^{3+} + 3e^-$ 2.1

Passivation: $2Al + 3H_2O \rightarrow A1_2O_3 + 6H^+ + 3e^-$ 2.2

Dissolution of oxide in acid: $A1_2O_3 + 6H^+ \rightarrow 2Al^{3+} + 3H_2O$ 2.3

Dissolution of oxide in alkaline media: $A1_2O_3 + 3H_2O + 2OH^- \rightarrow 2Al(OH)^{4-}$ 2.4

Cathodic reaction: $O_2 + H_2O + 4e^- \rightarrow 4OH^-$ 2.5

Magnesium generally exists in the form of $Mg(OH)_2$ in alkaline environments, whereas it will dissolve as Mg^{2+} in all but alkaline environments as indicated by Figure 2.3 [51].

Comparison of Figures 2.2 and 2.3 reveals that: (1) both Al and Mg dissolve at low pHs (~4); (2) Al is dissolving as AlO^{2-} at high pH levels (>10.5), whereas Mg is stable in the form of $Mg(OH)_2$; (3) At neutral pH levels Mg dissolves as Mg^{2+} while

aluminum oxide is stable.

2.4.2 Pitting Corrosion of Al Alloys

Pitting corrosion is a highly localized form of corrosion in which cavities or "holes" occur on the surface of material. Pitting is believed to be more dangerous than uniform corrosion due to the fact that it is more difficult to detect, predict and design against. Usually, a small pit with minimal metal loss may result in the failure of an entire structural system. Pitting usually occurs as a process of the local dissolution of anode where the corrosion of metal with lower electrochemical potential is enhanced by the presence of a relatively large cathode [50, 52], as indicated in Figure 2.4 [53]. Typically the extent of pitting depends on the exposure and surface conditions of the metals.

The mechanism of pitting corrosion is illustrated by Figure 2.4. Localized rupturing of the passive film allows localized corrosion of the metal and an increase in the local concentration of dissolved species - in particular the metal ions and the chloride ions that follow to maintain charge neutrality. The interior of the pit is a net anode, which is Al matrix, while the exterior are dissolved aluminum and oxide thin films (Al_2O_3). In the interior of the pit as the dissolution of aluminium is taking place, hydrolysis of $A1^{3+}$ decreases the pH as indicated by equation 2.2, which promotes further dissolution of anode. Ion conductivity is also increased in the localized zone, facilitating corrosion. The presence of metal ions and chloride ions in forming pits leads to hydrolysis reactions that form hydrochloric acid that further accelerates pitting growth [54-55].

It has been reported that pitting corrosion will be accelerated and become more severe when localized galvanic cells form between intermetallic particles and the surrounding aluminium matrix [50, 56-57]. The behavior of this type of localized corrosion is mainly determined by the potential difference between intermetallic particles and aluminium matrix [50]. N. Birbilis *et al.* summarized the corrosion potentials of multiple intermetallic particles typically present in Al alloys and of several pure metals in NaCl solutions [56] as listed in Table 2.2. Typically, the intermetallic particles such as Al_3Fe and Al_2Cu with higher electrochemical potential than the matrix act as cathodes and make the matrix dissolve [54, 58-61]. The intermetallic particles such as Al_2CuMg, Al_3Mg_2, and Mg_2Si with lower electrochemical potential than the matrix act as anodes and undergo dissolution [61-64]. In addition, when these particles are present in grain boundary areas, intergranular corrosion will occur as a result of the anodic dissolution of phase with lower electrochemical potentials.

2.4.3 Intergranular Corrosion (IGC) of 5XXX Al Alloys

2.4.3.1 Description of IGC

IGC, also known as intergranular attack (IGA), is a type of selective attack of grain boundary regions of crystalline materials which are more susceptible to corrosive environments than the interiors of grains. It usually develops in cast and wrought structures [49]. In 5XXX series aluminum alloys, β-phase precipitates upon ageing and forms a semicontinuous/continuous film along grain boundary planes [65]. This film is

anodic to the surrounding aluminum matrix and experiences anodic dissolution [43, 65], because the open circuit potential (OCP) of β-phase is much more active than the Al-Mg solid solution [43]. In a solution of 0.9M NaCl and 3% H_2O_2, for example, the OCP of β-phase was measured to be -1.24V SCE, whereas the OCP of Al-Mg solid solution is within the range of -0.870 and -0.890V SCE [66].

2.4.3.2 Mechanism of IGC

Most IGC mechanisms reported in the literature are based on the alloy systems of interest. The description of IGC often requires a continuous active path, which is usually developed by the alloy composition variations perpendicular to the grain boundary plane. This active path is usually composed by a region of the depletion of corrosion resistant elements, formation of anodic regions due to cathodic precipitate formation with corresponding precipitate free zones (PFZ), formation of anodic precipitates with the corresponding PFZ, segregation of anodic elements, or formation of anodic precipitates in a continuous path [67].

Several stages must occur before the development of IGC along grain boundary areas. At the first, the localized passivation film should break. Secondly, the surface of the metal without the coverage of passivation film will be exposed to an electrolyte layer which promotes the dissolution of the exposed surface metal. As corrosion process penetrates into the material, the electrolyte composition changes followed by the change of penetration rate. Finally, at some penetration into the materials, IGC rate may slow

significantly. In the next few paragraphs the anodic dissolution of $MgZn_2$ (η-phase) precipitates at the grain boundaries of AA7010, examined by Wloka and Virtanen [67], will be discussed as an example to illustrate the IGC process and mechanism.

2.4.3.2.1 Passive Film Breakdown

Several theories of how oxide breakdown occurs have been proposed so far. Wloka and Virtanen reported the passivation oxide layer in AA7010 alloy is weakened due to the inhomogeneous substrate at grain boundaries and thus, higher electric fields developed [67]. Chloride ions are easily accumulated at the grain boundary and promote the damage of passivation film. Since the surface of sample is still in the passive range, only a small passive current (i_p) was measured as shown by Figure 2.5. However, the extent that grain boundary is exposed to electrolyte caused by the passive film breakdown is enough for IGC to occur.

2.4.3.2.2 Surface Dissolution

The η-phase is readily dissolved in the electrolyte upon the contact with the electrolyte, resulting in a current transient, as shown in Figure 2.6. It is reported that because no stable pit growth was observed, it is reasonable to assume that non-oxide covered cavity left by the dissolution of the η-phase immediately repassivates [67].

2.4.3.2.3 IGC Penetration

The movement of dissolution front should be a function of the electrolyte composition and the material present. The penetration rate of continuous path of β-phase/η-phase should be higher than that of discontinuous path of β-phase/η-phase along the boundary, indicated by the longer and stronger current transient (the second spike) in Figure 2.7 in the case of dissolution of $MgZn_2$. In addition, the discontinuity of the grain boundary precipitates usually results in several current transients over time as shown in Figure 2.7. If all of the grain boundary precipitates dissolve, the current is expected to return to the same levels as that at the initial stage of the IGC. It also has been shown that the pH of electrolyte in a pit or crevice will drop when the electrolyte penetrates deeper into the material [68].

2.4.3.2.4 IGC Stifling

Elissa Bumiller reported that, on one hand, the rate of IGC may change as a function of penetration depth into the material [69]. The rate could remain the same as found in the dissolution of sub-surface β-phase or the rate could slow significantly. On the other hand, the rate of IGC penetration is also a function of width of the dissolution of the grain boundary [69]. IGC may slow down dramatically and penetration may be stopped, but the exact conditions for IGC inhibition to occur need more investigation.

2.4.3.3 Testing Methods on IGC

Testing methods to characterize IGC have been well established using electrochemistry and etchants. Some of these test methods have been standardized by the ASTM. In this section a brief review of the common test methods is provided.

For the characterization of IGC of 5XXX series Al-Mg alloys, ASTM G67 is widely accepted as a standard method. This test is also known as the NAMLT. This test provides a quantitative measurement of the degree of sensitization (DoS) to intergranular attack of these alloys [69]. The method consists of immersing samples in concentrated (70%) nitric acid at 30°C (85°F) for 24 hours and determining the mass-loss per unit area as the measure of DoS. When β-phase precipitates form a relatively continuous network along grain boundaries, the preferential attack of β-phase network releases the whole grain out of the samples. If the mass-loss is higher than 25 mg/cm^2, the sample should be classified as sensitive or non-resistant to IGC, whereas samples resistant to IGC lose only up to 15 mg/cm^2. When mass-loss is in between 15-25 mg/cm^2 the DoS is classified as indeterminate to IGC.

Additionally, a phosphoric acid etching method is adopted to quantitatively determine DoS. Basically, phosphoric acid etching works on the similar principle as NAMLT does, based on the large differences between the matrix and grain boundary β-phase dissolution kinetics under the condition of acidic pH [70].

The application of current/potential in neutral chloride solutions is another way to assess the DoS to intergranular attack when it is combined with a microscopic

examination of metallographic sections [71-73]. This method will be introduced through an example of the research by Stephenson [73]. Stephenson conducted research on the relationship between ageing time and DoS of AA5083 alloys using a chronoamperometric method [73]. He applied a constant potential to the sample exposed to pH 3 buffer solutions of 2.0 g/l Na_2SO_4 and 1.5% H_2O_2, by which β-phase networks along the grain boundary areas are preferentially dissolved. The charge passed (Q) is correlated to the DoS by the following equations:

$$DoS\ (C/cm^2) = Q/GBA, \qquad 2.6$$

$$GBA\ (cm^2) = A_s\,[5.1 \times 10^{-3} e^{0.35G}], \qquad 2.7$$

where A_s is the surface area (cm^2) of sample and G is grain size number according to ASTM. Using the samples of AA5083 aged at 150°C for different times, Stephenson found a linear relationship between ageing time and DoS. The amount of β-phase precipitated increased with the prolonged ageing times, which resulted in higher DoS [73]. However, Stephenson did not present the surface morphology of the samples after the electrochemical tests.

2.4.4 Stress Corrosion Cracking (IGC) of 5XXX Al Alloys

2.4.4.1 Description of SCC

It is well reported and accepted that the susceptibility of 5XXX alloys to intergranular stress corrosion cracking (IGSCC) can be attributed to the β-phase

precipitates along grain boundaries [6, 29, 63, 74, 75, 76, 77-81]. The β-phase corrodes selectively at a higher rate when exposed to various electrolytes, due to the very narrow semicontinuous/continuous path of anodic phase present along the grain boundaries.

The precipitation process of β-phase is sluggish at room temperatures. However, this process can be accelerated through exposure to elevated temperatures and extended ageing time, and deformation, and the increase of magnesium compositions. All of these factors mentioned above play important roles in the determination of the susceptibility of Al-Mg alloys to SCC. Here, we mainly focus on the review of the effect of ageing time and temperature on the susceptibility to SCC.

The dependence of the susceptibility of 5XXX aluminum alloys to SCC on ageing temperature and time was further illustrated by Dif *et al.*[75, 82]. In their work the SCC susceptibility was assessed by constant load alternate immersion tests in a solution of 3.5% NaCl and by slow strain rate tests (SSRT) in a solution of 3% NaCl plus 0.3% H_2O_2. It was found that cold-deformed AA5182 alloy is not sensitive to stress corrosion cracking, even after 100-hour ageing at 80°C. However, with ageing at more extensive temperatures ranging from 100°C to 140°C, this alloy was sensitized. They found that the susceptibility to SCC is related to the amount of magnesium precipitated at the grain boundary areas, which was calculated through a simple Fick's diffusion model. Dif *et al.* claimed the stress along grain boundaries accelerated stress corrosion cracking of the aged AA5182 alloy, which is anodic to the matrix. The results from static loading alternative immersion testing with respect to the threshold stress for SCC, and dynamic

SSRT with respect to elongation ratio of solution over air, were consistent with each other [75].

Searles *et al.* found similar dependence of SCC susceptibility on ageing time and temperature [6]. They found that the ductility measured by constant-extension-rate-test (CERTs) in 3.5% NaCl solution depended strongly on sensitization time and obtained a minimum value after 189 hours ageing at 150°C, followed by a slight recovery at longer times because of a decomposition of the continuous β-phase precipitates into discrete precipitates. They claimed that the β-phase precipitation along grain boundaries correlated well with the ductility measured by CERTs in solution over the entire range of sensitization times in their studies.

2.4.4.2 Mechanism of SCC

The SCC mechanism of Al alloys has been extensively investigated and two basic theories have been well accepted: anodic dissolution of β-phase and hydrogen induced embrittlement [29, 49, 83-90].

Basically, the anodic dissolution mechanism is based on the assumption that an increase in current flow would develop at the crack tip due to the fact that the freshly exposed metal is more anodic to the contiguous metal, and thus, the corrosion is accelerated till the reformation of a protective film. For 5XXX aluminum alloys, it is the anodic dissolution of Al_3Mg_2 along grain boundaries.

The mechanism of hydrogen embrittlement is based on the assumption that crack

propagation develops with corresponding embrittlement as hydrogen penetrates into the metal. Film-induced cleavage, intergranular separation or a highly localized plastic fracture will result from absorption of hydrogen by the metal. It is well accepted that hydrogen embrittlement is a dominant SCC mechanism in Al-based alloys, especially in 7XXX series alloys [83, 88, 85, 86, and 90]. The formation of brittle hydrides in some metals is part of the fracture mechanism [91]. Dissolution of hydrogen ions always plays an important role in the process of SCC. Electrons produced from anodic dissolution promote the hydrogen formation in water. The cation-hydrolysis-induced acidification also favors hydrogen discharge and absorption [83].

2.4.4.3 Testing Methods on SCC

Stress corrosion cracking (SCC) is a well investigated phenomenon in aluminum alloy systems, such as Al-Cu, Al-Zn-Mg-Cu, Al-Zn-Mg, and Al-Mg systems. The conduction of testing experiments using constant load or strain performed on smooth or pre-cracked samples have been established. Basically, SCC experiments are classified into three different categories: tests on statically loaded smooth samples; tests on statically loaded pre-cracked samples; and tests using slowly strained samples. Details of these testing methods are out of the scope of the present research. More information is available in other studies [92-93].

2.5 Summary of the Current Work

This chapter has attempted to outline the behavior of β-phase precipitation in Al-Mg alloys and their dependence on minor alloying elements, macro/micro defects, and ageing time and temperatures etc.

Minor alloying additions do have an enormous effect on the mechanical properties of Al-Mg-Mn alloys, especially in the refinement of grain size. However, the resistance of Al-Mg alloys to SCC remains a problem even after alloying efforts. The addition of small amounts of Zn promotes competitive precipitation of a ternary phase along grain boundaries which has demonstrated better SCC resistance than β-phase.

The major part of this chapter has focused on the introduction to IGC and SCC of Al-Mg alloys, including their initiation process, dominant mechanisms, and well-accepted testing methods.

Basically, the susceptibility to IGC often requires a continuous active path which is usually developed by the alloy composition variations perpendicular to the grain boundary plane. This active path is usually composed by a region of the depletion of corrosion resistant elements, formation of anodic regions due to cathodic precipitate formation with corresponding precipitate free zones (PFZ), formation of anodic precipitates with the corresponding PFZ, segregation of anodic elements, or formation of anodic precipitates in a continuous path.

The classical SCC mechanisms usually include anodic dissolution of β-phase and hydrogen induced embrittlement. Basically, the anodic dissolution mechanism is based

on the assumption that the crack tip grows from extremely localized β-phase anodic dissolution. The surface of metal at the crack tip is fresh and exposed to the corrosive environment. It is believed that anodic dissolution is initiated in the presence of sufficient stress against the base of the localized corrosion pits. Of particular interest is the hydrogen embrittlement mechanism, where absorbed hydrogen is primarily responsible for SCC. The mechanism of hydrogen embrittlement is based on the assumption that crack propagation develops with corresponding embrittlement as hydrogen penetrates into the metal.

Regardless of which mechanism is most strongly at play in the IGC and SCC of Al-Mg alloys, the degree of β-phase precipitation on the grain boundaries lies at the heart of each.

Table 2.1 Compositions of 5083 and 5456 aluminum alloys (wt. %) [21]

Alloys	Si	Fe	Cu	Mn	Mg	Cr	Zn	Ti	Others (< 0.15)	Al
5083	Max 0.4	Max 0.4	Max 0.1	0.4-1.0	4.0-4.9	0.05-0.25	Max 0.25	Max 0.15	0.05	remainder
5456	Max 0.25	Max 0.4	Max 0.1	0.5-1.0	4.7-5.5	0.05-0.20	Max 0.25	Max 0.2	0.05	remainder

Table 2.2 Corrosion potentials of various intermetallic particles in aluminium alloys and pure metals [56]

Particles/Metals	Corrosion Potential (mV, SCE) in NaCl solutions		
	0.01 M	0.1 M	0.6 M
Mg_2Si	-1355	-1538	-1536
Al_3Mg_2	-1124	-1013	-1162
$MgZn_2$	-1001	-1029	-1095
Al_2CuMg	-956	-883	-1061
Al_6Mn	-839	-779	-913
Al_2Cu	-592	-665	-695
Al_3Fe	-493	-539	-566
Al	-679	-823	-849
Mg	-1601	-1586	-1688
Zn	-985	-1000	-1028
Cu	-177	-232	-220
Si	-450	-441	-452

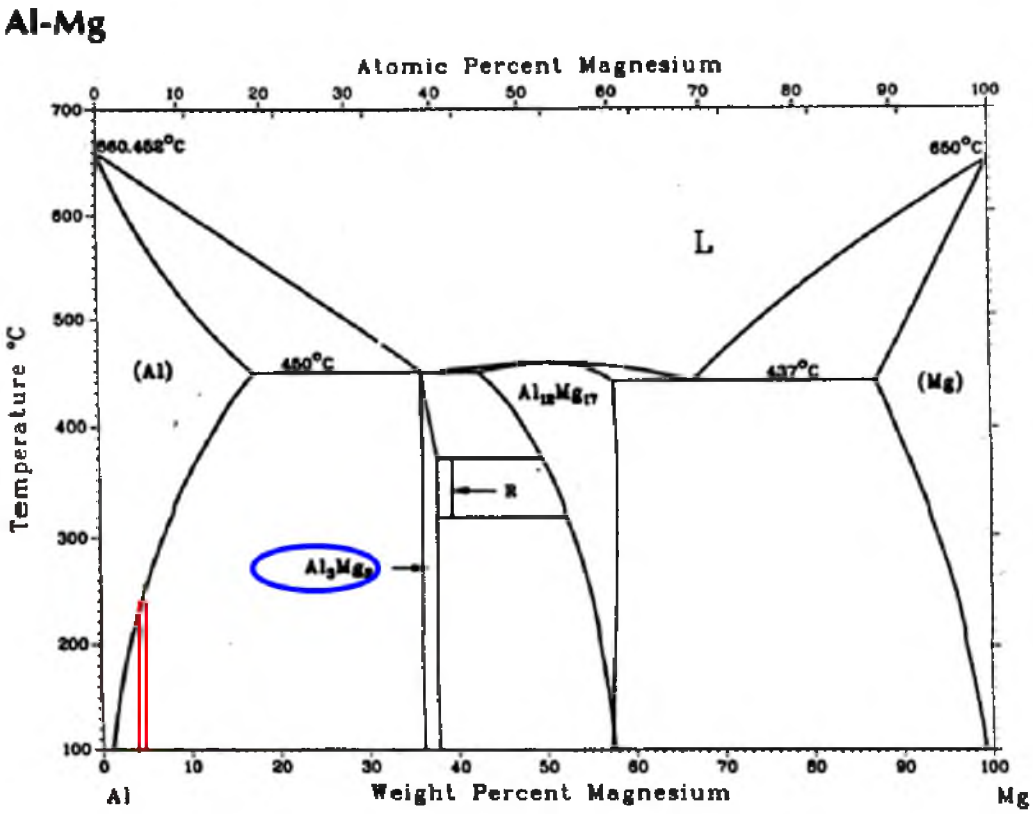

Figure 2.1 Al-Mg binary phase diagram.

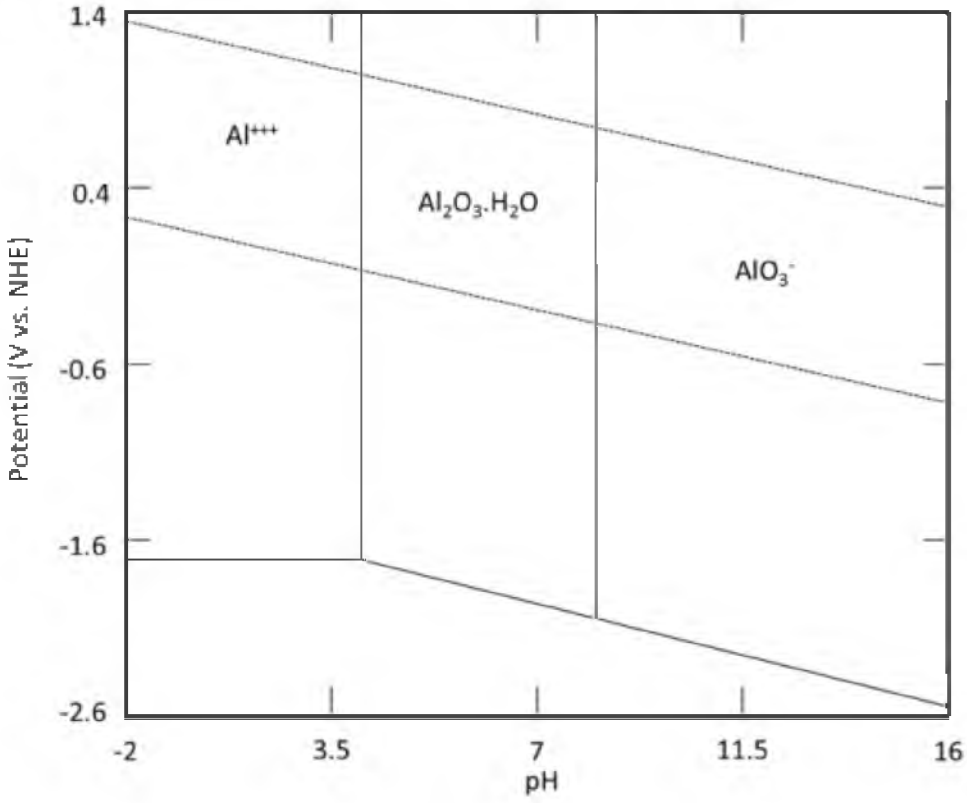

Figure 2.2 Potential-pH equilibrium diagrams for the system aluminum-water at room temperature.

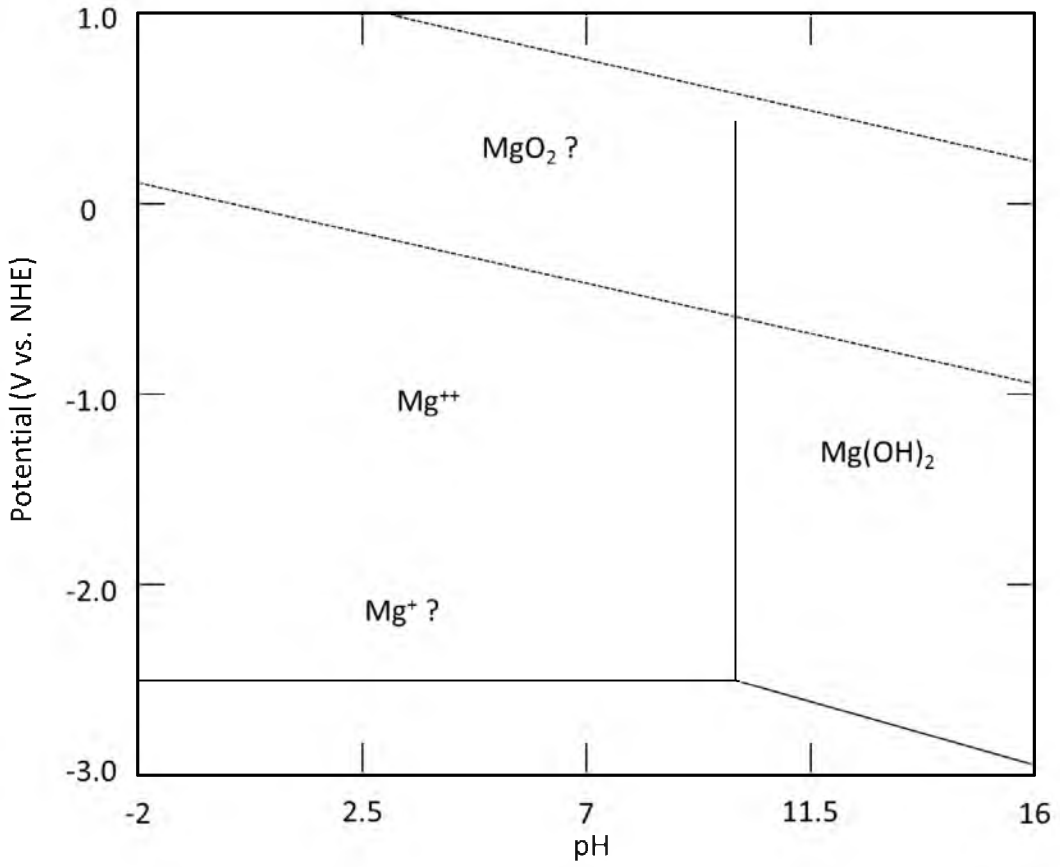

Figure 2.3 Potential-pH equilibrium diagrams for the system magnesium-water at room temperature.

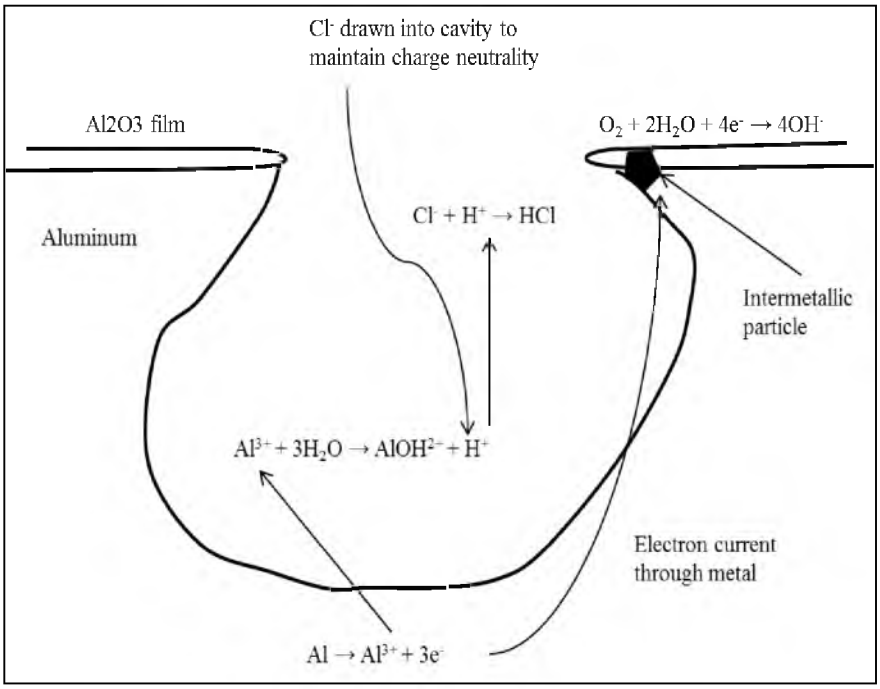

Figure 2.4 Diagram of the mechanism of corrosion of aluminium in aqueous environment including chloride ions. Aluminium dissolves through the anodic reaction and hydrolysis lowers the pH. Intermetallic particles act as cathodic sites to consume the electrons produced in the dissolution of the aluminium matrix.

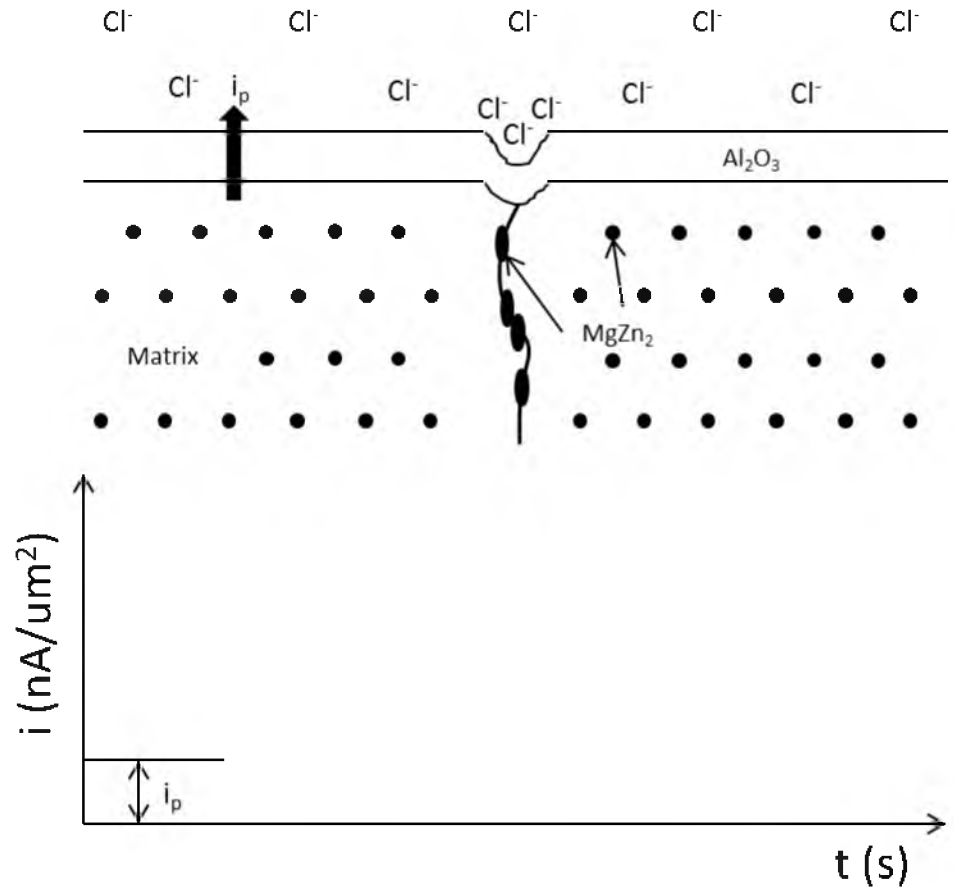

Figure 2.5 Schematic of passive film breakdown promoted by concentrated chloride ions.

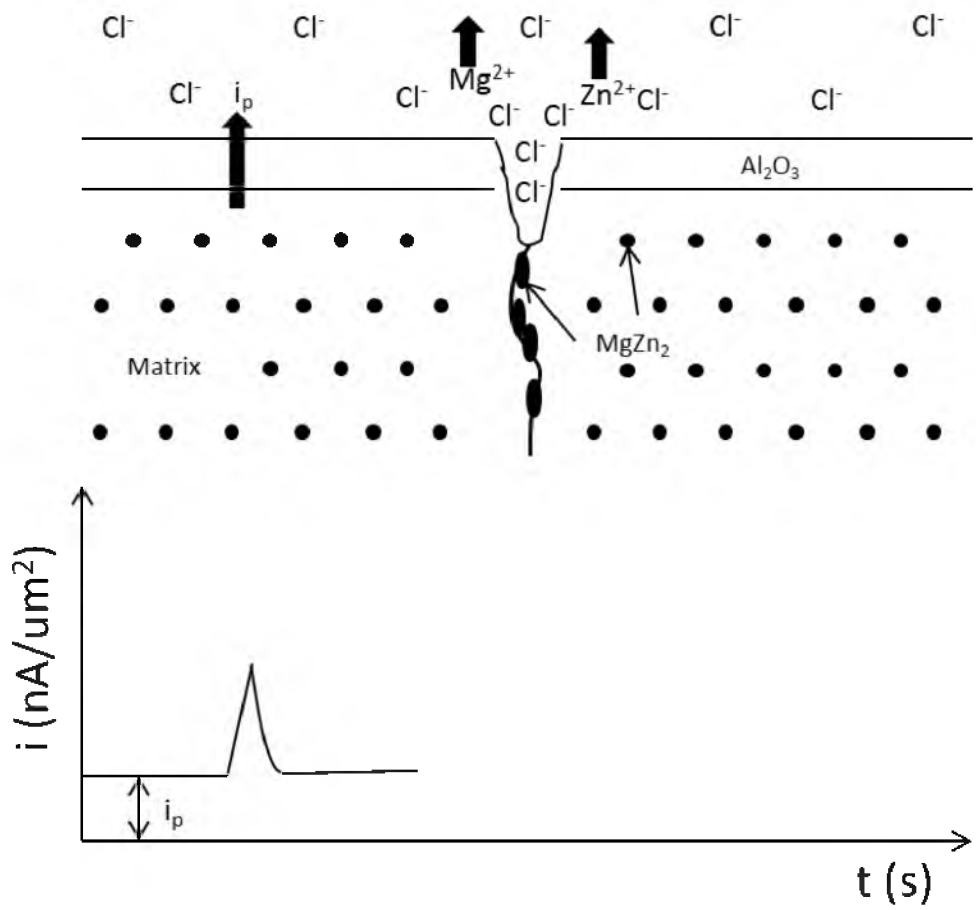

Figure 2.6 Schematic of surface dissolution of $MgZn_2$ in AA7010 alloy.

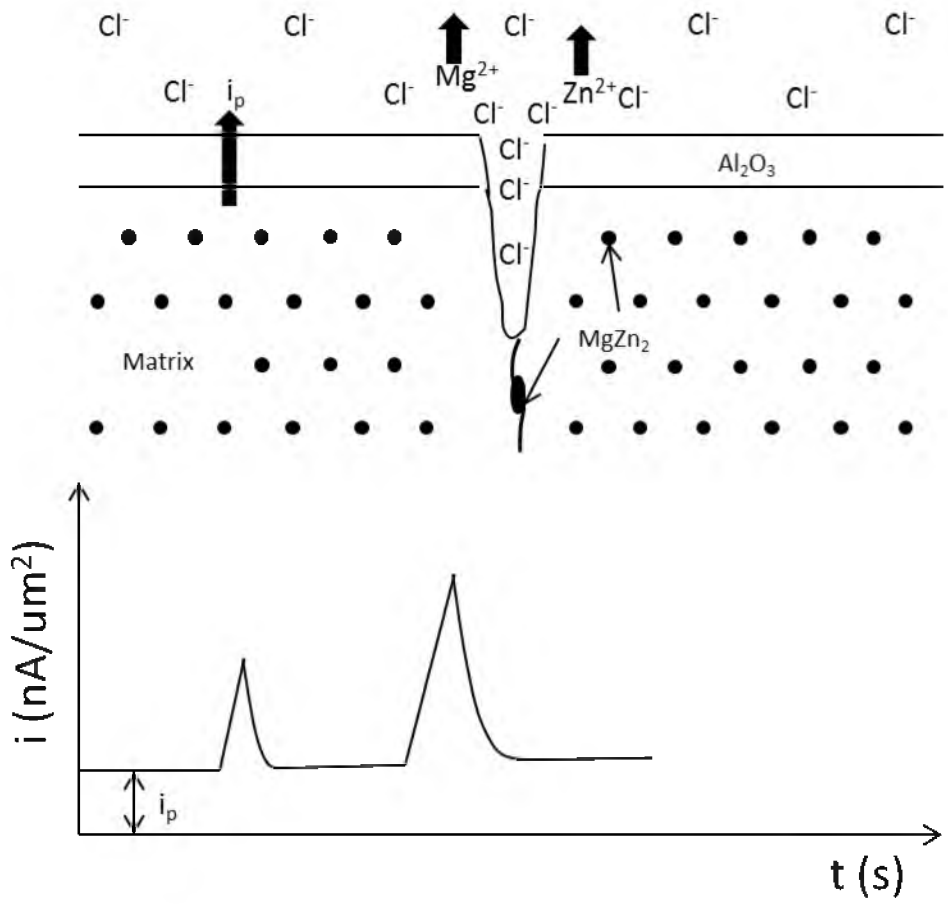

Figure 2.7 Schematic of the dissolution of subsurface $MgZn_2$ precipitates in AA7010.

CHAPTER 3

EXPERIMENTAL METHOD

3.1 Materials

3.1.1 As-received Alloys

Commercial Al-Mg AA5083-H131 and AA5083-H116 alloys supplied by Alcoa, and AA5083-H321 and AA5456-H116 alloys supplied by Pierce Aluminum were used in this work. The nominal compositions of AA5083 and AA5456 alloy were given in Table 2.1. However, Table 2.1 just lists estimated compositions of AA5083 and AA 5456 alloys. For the accuracy of the present work, STEM-EDS and ICP (inductively coupled plasma) were used to determine the composition of 5083-H131alloy.

3.1.2 Heat Treatment

In order to induce the segregation of Mg to grain boundaries and precipitation of β-phase, the above four alloys were aged both at constant and cyclic temperature for various times, including short term and long term, as shown in Tables 3.1 - 3.3.

In constant thermal exposure tests, samples were placed in four ovens and the oven temperatures were held constant at 40°C, 50°C, 60°C and 70°C. Our earlier work showed evidence of sensitization at high thermal exposure temperature for short

time [3]. However, no such data has yet been reported based on the sensitization at low thermal exposure for a long time. For this, low thermal exposure temperatures were chosen. Figure 3.1 shows the thermal exposure ovens running at four different constant temperatures.

The long term cyclical thermal exposure is based on the data collected by the Navy on a Sea Fighter starting at San Diego, CA and ending at Panama City, FL via the Panama Canal (provided by Naval Surface Warfare Center (NSWC)). Figure 3.2 shows the set-up used for cyclic thermal exposure tests. In our lab, two ovens and a supporting computer are operated for cyclic thermal exposure tests. A temperature monitoring device, NI USBTCO-1, was purchased from National Instruments which is able to measure the accurate temperature of the ovens. Labview is used to control the furnace temperature. A relay is connected to the ovens to control the heating rate of the ovens based on the command from Labview software. Furnace temperature is varied in a cyclic manner to correlate experimental results with actual ship exposure temperatures in a sea environment. The exposure temperature was chosen based on the data collected by the Navy as indicated previously.

The exposure temperature obtained from NSWC was analyzed and the average temperature profile (19th March - 22nd March) is shown in Figure 3.3, which is a plot of cyclical oven temperature, fitting temperature, and real temperature versus exposure time. The real data was fit first to obtain a continuous profile of the data. Then, a program was written and applied to the thermal exposure ovens and related devices to represent the

heating and cooling cycles experienced by naval ships during the hottest 6-hour period of the day. We can see that the plot of oven data, matches the real data and fitting data very well in the temperature cycle. The upper limit temperature and lower limit temperature of the plot of oven data are estimated at 45°C and 40°C based on NSWC data (shown in Figure 3.3). On a typical dry-season day in Panama City, Panama, the highest temperature recorded on an aluminum sample was measured to be 70°C. So, for the higher temperature cyclic thermal exposure, the upper limit temperature and lower limit temperature are estimated at 70°C and 50°C, respectively. Figure 3.4 shows the thermal cycling at these two different temperature ranges.

3.2 Sample Preparation

3.2.1 Samples for Metallographic Observation

Specimens of commercial AA5083 were sectioned in the longitudinal (L), long-transverse (T), and short-transverse (ST) directions with approximate dimensions of 8 x 8 x 8 mm. After cyclic and thermal exposure test, the sample was cut and mounted with epoxy mixture (epoxy resin with epoxy hardener in the ratio of 10:4). To achieve a proper hard mount, the sample along with the epoxy mixture was left untouched for 24 hours. The mounted samples were then polished using a series of polishing clothes (up to 0.05 μm colloidal silica) to get a smooth and clean surface. Polishing was carried out in five different steps. First, samples were polished using (P240-P4000) SiC polishing papers. Ultra-pol cloth and 9 μ m diamond suspension abrasive were used for subsequent

polishing stage. In the following two stages Trident clothes were used with 3 μm diamond suspension abrasive and 1 μm diamond paste, respectively. In the final stage microcloth was used with 0.05 μ m colloidal silica abrasive. The polished samples were then etched and analyzed using light microscopy. Phosphoric acid solution (10 vol. % phosphoric acid) was used to etch samples at 50°C for 2 minutes to make the β-phase visible as etch trenches. For comparison, ammonium persulfate solution (20 mg+200ml water) was also used to etch samples at room temperature for about 25 minutes.

3.2.2 Samples for Electron Microscopy

For STEM/TEM sample preparation after heat treatment at various times and temperatures, thin foils were prepared for observation in the electron microscope by dimple grinding and ion milling. First, 3 mm discs were cut from the foils using a disc punch. The discs were then mechanically ground and polished using a dimple grinder to a thickness of less than 30 microns. The dimpled discs were then thinned to electron transparency using an argon ion mill operating at 5 keV with an incidence angle of 15°. Final cleaning was performed at 1 keV with an incidence angle of 10°.

3.2.3 Samples for Nitric Acid Mass-loss Testing

Samples for ASTM G67 mass-loss tests were sectioned from bulk materials with a dimension of 51mm x 7mm 26mm as shown in Figure 3.5. The samples were then polished to obtain a smooth surface. After that, all three dimensions of each sample were accurately measured to calculate the total surface area. The sample was then immersed in

5% NaOH solution at 80°C for 1 minute, followed by a water rinse. Next, the specimen was immersed in 70 wt. % HNO_3 for 30 seconds, followed by a water rinse. The weight of the specimen was taken after air drying for 1 hour, and the dried sample was immersed in the test solution (nitric acid with 70 wt. %) for 24 hours. After a water rinse, scrubbing with a brush, and air drying, the sample was weighed to calculate the mass-loss per unit area (mg/cm^2).

3.2.4 Samples for ICP-AES Testing

To evaluate the Mg concentration of baseline samples ICP tests were performed. One baseline sample was well polished using 6 um polishing clothes. Some powder was moved from the baseline sample and then dissolved in 5 wt. % phosphoric acid followed by ICP analysis of the solution.

3.2.5 Samples for EBSD Characterization

Electron backscattered diffraction (EBSD) patterns were obtained using a JEOL 840A scanning electron microscope operating at 20 kV with the sample tilted at 70° to the horizontal. The EBSD pattern was captured via a phosphor screen interfaced to a low-light TV camera and control unit. With this arrangement, the orientation of crystal can be obtained and analyzed to generate crystal orientation maps (COMs) using fully automated computer control software.

3.2.6 Samples for AFM Imaging

Before imaging, the samples were polished using the same procedures as that in Section 3.2.1 but without etching. The sample was further etched using an argon ion milling gun. The working conditions for the ion gun were set as indicated in Table 3.4. Note that these parameters are estimated values and they may change with respect to specific samples.

3.3 Microstructural Characterization

3.3.1 Optical Microscopy

A NMM-800RF system metallurgical microscope with a digital image capture system was used for characterization and observation of the surfaces.

3.3.2 Scanning Electron Microscopy

Nova™ Nano scanning electron microscope equipped with energy dispersive X-ray spectroscopy (EDS) system was used to observe the surface morphology using both secondary electrons and back scattering electrons, and also to identify constituent particles/phases.

3.3.3 Transmission/Scanning Transmission Electron Microscopy

For transmission/scanning transmission electron microscopy (STEM/TEM) imaging, several types of TEM were used. One is a JEOL 2200FS probe-corrected STEM equipped with a Bruker X-Flash detector used to acquire EDS spectra and high-angle

annular dark-field (HAADF) and bright-field (BF) images. EDS quantification was performed using the Cliff-Lorimer quantification routine built into the Bruker Esprit software package, which calls on the theoretical k-factors from the standard library. The k factors used for the Al and Mg K edges were 0.957 and 0.911, respectively.

3.3.4 Atomic Force Microscopy

The surface topography of the samples was examined using a Dimension ICON-PT atomic force microscope (AFM) equipped with Nanoscope v8.1 Controller Software, operating in contact mode. The maximum scan area was 90 um x 90 um and the maximum depth reached by the scanner was approximately 10 um.

3.4 IGC Susceptibility Detection

3.4.1 Phosphoric Acid Etching

Phosphoric acid etching is used to qualitatively assess the DoS to IGC. The sensitized samples were etched in a solution of 10 vol. % phosphoric acid at 50°C for 2 minutes. Grain boundary etch trench is believed to be an indication of the amount of β-phase precipitated.

3.4.2 Nitric Acid Mass-loss Testing

Nitric acid mass-loss test (NAMLT) is established as a standard method (ASTM G67-93) to quantitatively measure the susceptibility of Al-Mg alloys to IGC[107]. The sample is first immersed in concentrated (around 70%) nitric acid at 30°C (85°F) for 24

hours, followed by the calculation of the mass-loss per unit area, as an indication of intergranular susceptibility (for details see Section 3.2.3). If the mass-loss is higher than 25 mg/cm^2, the sample is classified as sensitive to IGC, whereas if the mass-loss is below 15 mg/cm^2, the sample is insensitive to IGC. When the mass-loss is in between 15 - 25 mg/cm^2, the sensitivity is undetermined.

3.4.3 Ammonium Persulfate Etching

For SEM imaging of intergranular β-phase, ammonium persulfate etching (20 mg+200ml water) is another method that is used to attack β-phase and measure susceptibility to IGC. Basically, the sample is immersed in the solution for 20 - 30 minutes at room temperature.

3.5 The β-phase Thickness Measurement

For the measurement of β-phase thickness along grain boundaries, one grain boundary filled with β-phase was first chosen, as shown in Figure 4.4 (a). The electron image, either from SEM or TEM, was printed out, and then the equi-spaced, 0.5 cm in this case, lines were drawn in a grid pattern on the image. The thickness of either the etch trench in the case of SEM image, or the β-phase in the case of TEM image, was measured perpendicular to the grain boundary at each point where the line intersects the grain boundary. The average thickness distribution profile was constructed using this data and the corresponding average thickness was determined from the distribution profile.

Table 3.1 Short-term ageing of AA5083-H131 and AA5456-H116 alloys

Alloy	Heat treatment conditions				
AA5083-H131	120°C and 175°C for different times (days)				
	120°C			175°C	
AA5456-H116	1	2	3	10	15

Table 3.2 Long-term ageing of AA5083-H131, AA5083-H321, AA5083-H116 and AA5456-H116 alloys at constant temperatures of 40°C, 50°C, 60°C, and 70°C

Time (month)	**Temperature (°C)**	**Status**
1.5	70, 40	Completed
2	70, 60, 50	Completed
3	70, 60, 40	Completed
4.5	70, 50	Completed
6	70, 60, 40	Completed
9	70, 60, 50	Completed
12	70, 60, 40	Completed
15	60, 50	Completed
18	70, 60, 50, 40	Completed
24	70, 60, 50, 40	Completed
30	70, 60, 50, 40	Completed

Table 3.3 Long-term ageing of AA5083-H131, AA5083-H321, AA5083-H116 and AA5456-H116 alloys at cyclic temperatures of 40-45°C, and 50-70°C

Time (month)	Timeline of heat treatment (mm/dd/yy)		Status
	50°C-70°C	40°C-45°C	
1	11/22/10-12/22/10		Completed
2	09/22/10-11/22/10	09/22/10-11/22/10	Completed
3	09/22/10-12/22/10	09/22/10-12/22/10	Completed
4	09/22/10-01/22/11	09/22/10-01/22/11	Completed
6	09/22/10-03/22/11	09/22/10-03/22/11	Completed
9	09/22/10-06/22/11	09/22/10-06/22/11	Completed
12	09/22/10-09/22/11	09/22/10-09/22/11	Completed
15	09/22/10-12/22/11	09/22/10-12/22/11	Completed
18	09/22/10-03/22/12	09/22/10-03/22/12	Completed
24	09/22/10-09/22/12	09/22/10-09/22/12	Completed
30	09/22/10-03/22/13	09/22/10-03/22/13	Completed

Table 3.4 Working conditions of the argon ion milling gun for AFM sample preparation

Parameters	Values
Chamber pressure	10-7 Torr
Beam energy	7 KeV
Beam current	300 +/- 20 uA
Spot size	7 – 10 mm^2
Etching rate	300 nm/min
Etching time	2 minutes

Figure 3.1 Constant thermal exposure (40°C, 50°C, 60°C and 70°C) heat treatment is in progress for 5083-H131, 5083-H116, 5083-H321 and 5456-H116 alloy specimens.

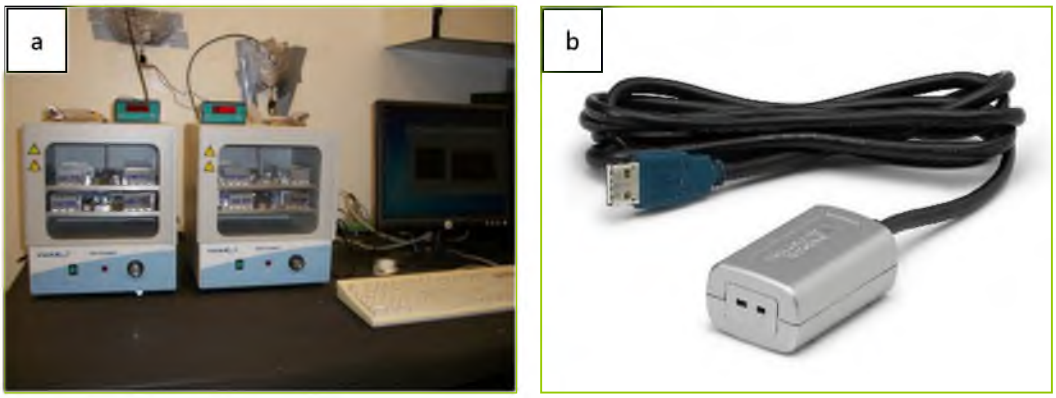

Figure 3.2 Cyclic thermal exposure test set-up: (a) two ovens and a supporting computer; (b) NI USBTCO-1.

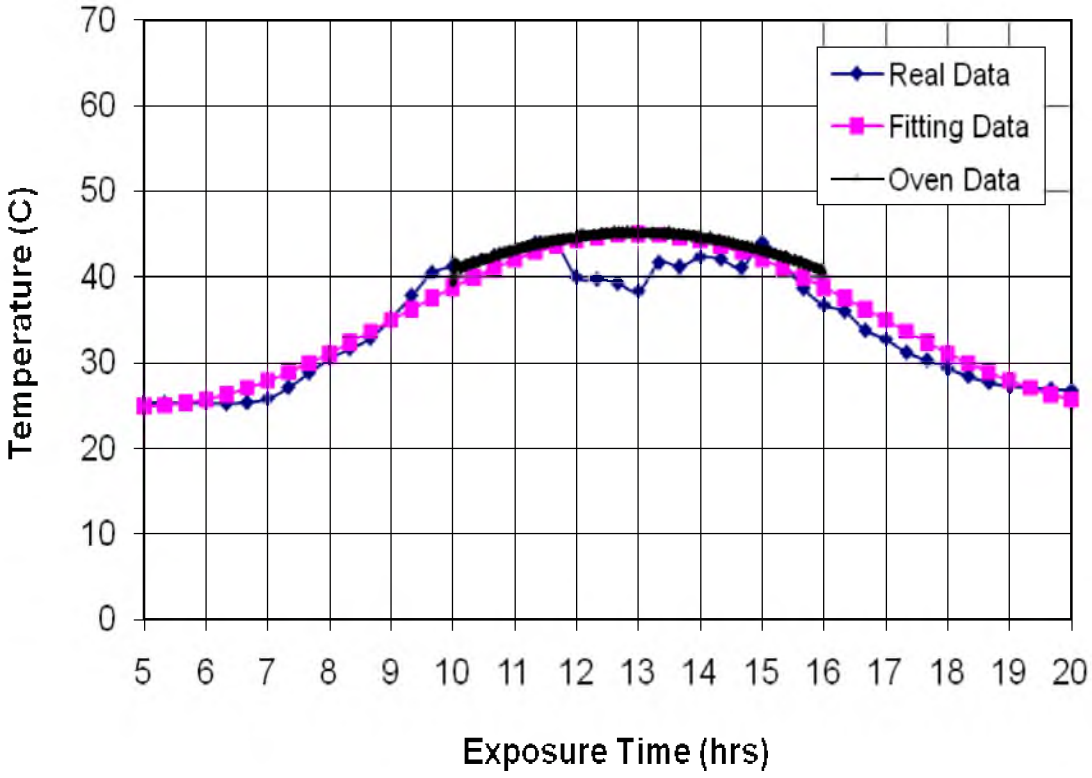

Figure 3.3 Comparison of real temperature versus lab scale oven temperature profile.

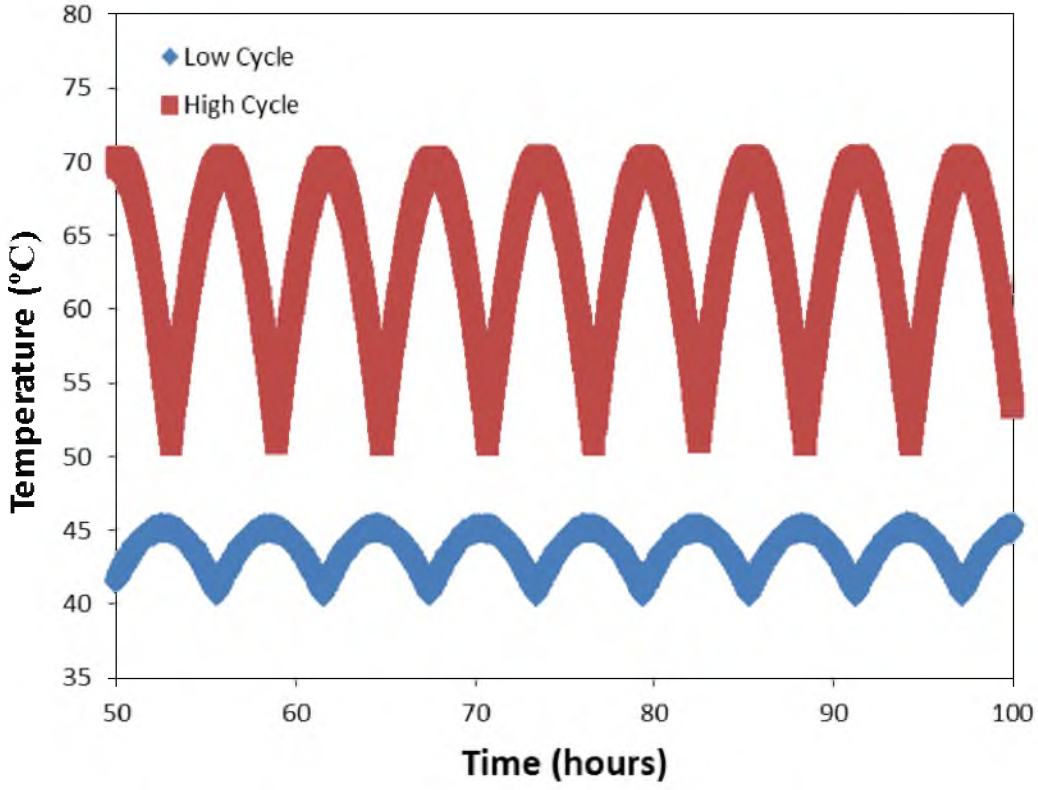

Figure 3.4 Thermal cycling at two different temperature ranges: low cycle 40-45°C; high cycle 50-70°C.

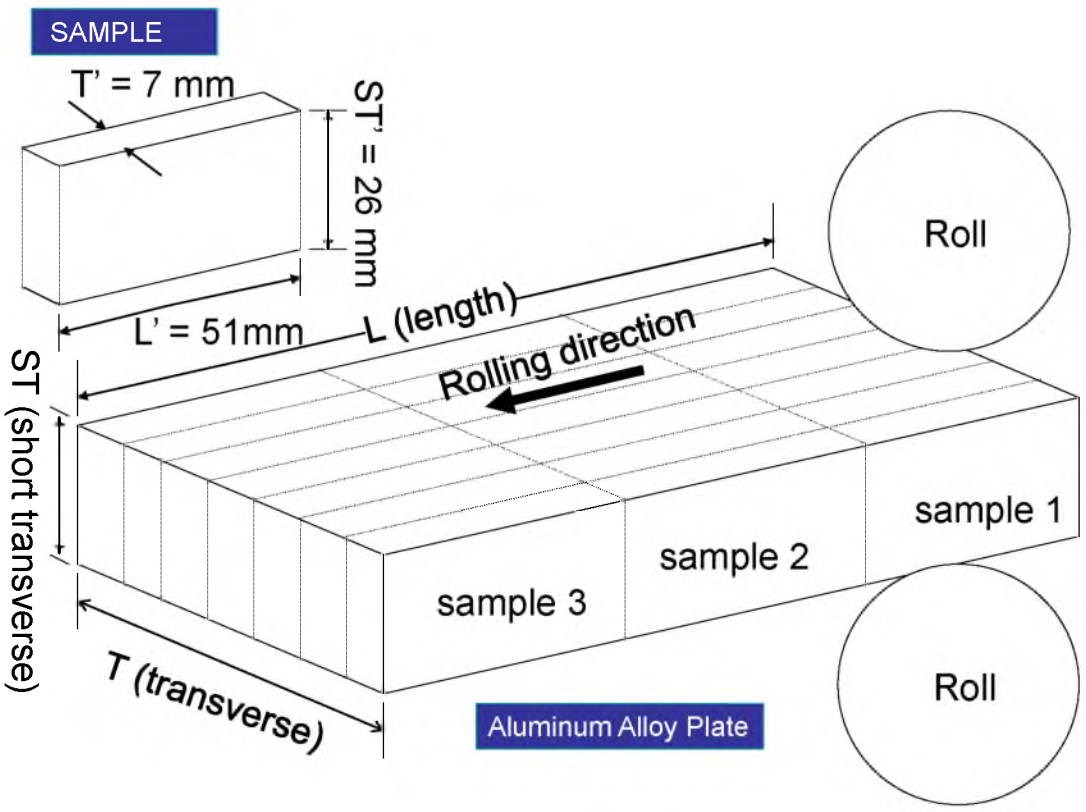

Figure 3.5 Schematic diagrams showing the as-received alloy plates and the sectioned piece suitable for ASTM G67 mass-loss tests.

CHAPTER 4

MICROSTRUCTURAL CHARACTERIZATION OF ALLOYS

4.1 Optical Metallography

The grain structure after sensitization of the as-received 5083-H131 alloy samples at 150°C is shown in Figure 4.1. Since the etchant preferentially attacked the β-phase, β-phase accumulated abundantly along the grain boundary as evidenced by the phosphoric acid etch trench in both figures. However, the sample in Figure 4.1(b) was more sensitized because of longer aging time. In the sensitized samples, non-metallic phases (faded dark color) were also visible, which will be discussed later in detail.

4.2 Grain Structure Based on EBSD

The grain structure of the as-received sample of 5083-H131 alloy was further shown in Figure 4.2 by electron back scattering diffraction (EBSD) image. The EBSD revealed an equiaxed microstructure on the LT (longitudinal-transverse) surface and an elongated microstructure on the LST (longitudinal-short transverse) surface, as shown in Figures 4.2(a) and 4.2(b), respectively. Measurements of β-phase growth that are needed

to determine modeling constants, which will be discussed in detail later, are made by examining the LST surface because the LST surface offers the most parallel grain boundaries and it is easier for the one-dimensional (1D) measurements of Mg diffusion to grain boundaries rather than two-dimensional (2D) or three-dimensional (3D).

4.3 Comparison of Etching Solutions Based on SEM

As mentioned in Chapter 3, two etching solutions were used to etch the alloy samples before optical imaging and SEM imaging so that the β-phase precipitated along grain boundaries will be removed or etched and the etch trench is believed to be equal to the β-phase thickness. Figure 4.3 shows the comparison of effects of the two solutions on β-phase dissolution along grain boundaries in the sample of 5083-H131 aged at 70°C for 1 year. As can be seen, the etch trench visible in Figure 4.3(a) is much thicker than that in Figure 4.3(b), which is estimated to be around 11 nm and is equivalent to the grain boundary β-phase thickness measured by high resolution TEM. Therefore, it is concluded that phosphoric acid solution over etches the sample, whereas ammonium persulfate etching provides results and that are comparable to TEM measurement.

4.4 SEM Imaging of 5083-H131 and 5456-H116 Alloys Samples

The comparison and contrast of microstructures of 5083-H131 and 5456-H116 are shown in Figure 4.4 based on SEM imaging. Rod-shaped and equiaxed bright particles are present in both samples and they are believed to be rich in Mn, Fe, or Cr.

The images in Figure 4.4 were collected based on secondary electron signals, and the brightness of such images are proportional to the atomic number of the elements in the materials. Actually, TEM will confirm these particles are rich in Mn, Fe, and Cr in later discussions. The width of grain boundaries visible as etch trenches is believed to be equal to the β-phase thickness. Under the same heat treatment history and same imaging conditions, the average grain boundary β-phase thickness of 5083-H131 is much thinner than that of 5456-H116, as indicated in Figure 4.4. This statement is supported by the measurement of β-phase thickness of these two samples, 11 nm and 34 nm, respectively, and the corresponding thickness distribution plot in Figure 4.5. The β-phase thickness of 5456-H116 sample falls in the range of 30 - 70 nm, much higher than that of 5083-H131 sample. This is likely due to the higher Mg composition, namely 4.7 - 5.5 wt. %, in 5456-H116 alloy and thus, more Mg is available to form β-phase precipitates.

4.5 Grain Size Measurement

4.5.1 Grain Size Measurement Using AFM

Due to the limited resolution of SEM and EBSD used in the present research, damaging effects from etching solutions on the grain boundaries, and the fine grain size of the as-received alloys partially indicated by the EBSD images in Figure 4.2, AFM was adopted as one method to measure the grain size. Two AFM images from the as-received sample and one aged sample are shown in Figure 4.6. The average grain/sub-grain size estimated from both samples is around 1 um, and this value will be used in the β-phase

thickness prediction model in Chapter 6. In addition, it also reveals that the ageing has no effect on grain growth.

4.5.2 Grain Size Measurement Using TEM

To confirm the grain size measurement by AFM, a high resolution TEM was also used to measure grain size. Two representative images captured from two samples, respectively, are shown in Figure 4.7. The average grain/sub-grain size was estimated from both samples to be around 1 um, which is consistent with the AFM measurement, and will be used in the modeling work in Chapter 6.

4.6 Determination of Mg Composition in the As-received Sample

It is important to measure Mg concentration in the Al matrix because the amount of Mg determines how much β-phase will form. ICP-AES and STEM-EDS measurements gave average Mg concentrations of 4.85 ± 0.05 wt. % and 5.00 ± 0.15 wt. %, respectively, for AA5083-H131, as listed in Table 4.1. These results indicate that the concentration measurement from these two techniques match well. The previous work[12] in this field failed to provide sufficient experimental information about the presence of Fe, Mn, and Cr in α-matrix. However, our results as obtained from EDS quantification reveal that the Al matrix (α-phase) also contains Fe, Mn, and Cr, ranging from 0.5 wt. % to 1.5 wt. %.

4.7 Pre-existing Particles Characterized by TEM

The behavior of β-phase precipitates and some pre-existing particles were characterized by observation in the as-received sample and the aged samples. These particles are found to be associated with β-phase precipitates behaviors, which will be discussed in detail in this section.

4.7.1 Pre-existing Particles in the As-received Sample

While no β-phase precipitates were observed in the baseline sample, some of the pre-existing particles, either rod-shaped or needle-shaped, in the as-received samples were observed, as shown in Figures 4.8 and 4.9 accompanied by the corresponding STEM-EDS line scan. These two particles are around 50 nm wide and are rich in Mn, Fe, and Cr, indicated by the EDS line scan composition profiles. EDS quantification of the particle in Figure 4.8 indicates that this particle contains around 8.6 wt. % Mn, 1.3 wt. % Cr, and 1 wt. % Fe.

One such type of particle, shown in Figure 4.10, was indexed and identified to be Al_6(Mn-Fe-Cr) with a prototype of Al_6Mn (Cmcm, a = 7.5518 Å, b = 6.4978 Å, and c = 8.8703 Å). These preexisting particles and grain boundaries provide potential nucleation sites for β-phase formation due to the low activation barrier for nucleation. It should be noted that no attempt was made to locate Mg_2Si particles because many researchers have reported the existence of Mg_2Si in AA 5083 alloy [10-11, 94-95].

4.7.2 Pre-existing Particles in the Aged Sample

The pre-existing particles mentioned above were also observed in aged samples. Figure 4.11 presents some equiaxed particles in the sample aged at 70°C for 1 year. These two images were captured under high-angle annular dark-field (HAADF) mode under which the brighter regions correspond to heavier atoms, as the scattering cross-section is proportional to Z^2. The areas in the yellow box were quantified by STEM-EDS and the corresponding results were listed in Tables 4.2 and 4.3. As is indicated, these particles are also rich in Mn, Fe, and Cr, which is consistent with previous discussions, whereas the Mg composition is lower than the average matrix level.

4.8 β-phase Precipitates

4.8.1 Intergranular β-phase Precipitates

Mg tends to form precipitates along grain boundaries upon heat treatment to form a thin layer of β-phase, as shown in Figures 4.12(a) and 4.12(b), which are high-angle annular dark-field (HAADF) images of grain boundaries of a sample heat treated at 175°C for 15 days and of a sample heat treated at 70°C for 1 year, respectively. The measured thicknesses of β-phase in Figures 4.12(a) and 4.12(b) are around 45 nm and 7 nm, respectively. The difference in β-phase thickness of these two samples is mainly attributed to the temperature effect on β-phase growth. Evidence of β-phase formation on the grain boundaries is provided by the EDS line scan results in Figure 4.12(c). An

estimation of Al to Mg atomic ratio is about 3:2 based on the EDS line profile in Figure 4.12(c). This ratio was confirmed by quantifying the Al and Mg peaks in EDS spectra collected from the middle of the grain boundary. The result listed in Table 4.4, 59 at. % Al, 41 at. % Mg, was consistent with the line profile. To check the accuracy of the quantification, EDS spectra taken of the matrix in this same region were also quantified, and gave 95 at. % Al and 5 at. % Mg, as expected.

In addition, thickness of 45 nm in heat-treated sample at 175°C for 15 days is much smaller than the reported value of 50 - 190 nm of a 5083-H131 alloy sample heat treated for 10 days at 175°C[12], even though the thermal treatment time was longer. Following the Zener-Hillert diffusion-controlled growth model for estimating the distance of growth interface [12, 96-97], the β-phase thickness of the sample heat treated for 15 days at 175°C should be 50-55 nm, which is thicker than all the observed β-phase thicknesses (~ 45 nm) along grain boundaries except the thickness of β-phase that is connected with dislocations which will be discussed later.

Goswami *et al.* explained the thickening behavior using the Zener-Hillert diffusion model[12]. However, the Zener-Hillert diffusion model assumes a semi-infinite system, whereas in this work diffusion takes place in a finite system, and the bulk concentration of Mg decreases with time. The conventional error function solution of Fick's second law for a semi-infinite/infinite system cannot be accurately used in the present scenario. The solution of this problem can be obtained by a variable separation technique using Fourier's law which is beyond the scope of the present paper. Another

potential reason for the discrepancy relates to the inherent stress in this heavily cold worked structure along grain boundary/phase interfaces, for which significant research has been conducted [98-100]. The stress may prevent β-phase from growing thicker once stress effects are balanced with the driving force for diffusion.

4.8.2 Intragranular β-phase Precipitates

In addition to intergranular β-phase formation, intragranular β-phase precipitation was observed around rod-shaped and equiaxed preexisting particles, which were also present in the as-received sample and were shown to be rich in Mn, Fe, and Cr. Evidence is provided by Figure 4.13(a) which presents a HAADF image of intragranular precipitates. EDS mapping suggests that the bright particle is rich in Mn, Fe, and Cr, whereas the arrowed dark region is rich in Mg. Contrast is consistent with average atomic number; the Mn-Fe-Cr precipitates are brighter than the Al matrix, while the Mg precipitate is darker. Further, EDS quantification of the area in the solid red box reveals that this region is composed of Al and Mg at an atomic ratio of 3:2, which suggests that it is β-phase. Quantification of the area marked by the dotted green box suggests that the composition of this region matches a chemical formula of Al_6(Mn-Fe-Cr), which is consistent with the analysis of the baseline sample and reported results [10, 12]. EDS quantification results are listed in Tables 4.5 and 4.6. More intragranular β-phase precipitates are shown in Figures 4.13(b) and 4.13(c). A noteworthy point is the preferential tendency of precipitation for Mn-rich particles and β-phase along grain

boundaries, which is evident from Figure 4.13(b). Mn-rich particles were preexisting. Although it is believed that they provided nucleation sites for β-phase, the lengthening kinetics of β allotriomorphs was retarded due to the unavailability of grain boundary nucleation sites which were already occupied by Mn rich particles.

It was also discovered that some β-phase had precipitated between Mn-rich particles, as shown in Figure 4.14. The bright particle in Figure 4.14(a) is rich in Al, Mn and Fe, and is surrounded by an Mg-rich phase (dark contrast), which can be seen clearly in the corresponding EDS mapping in Figure 4.14(c). EDS quantification of these Mn-rich and Mg-rich regions (areas in the dotted-green and solid-red boxes in Figure 4.14(b)) suggests that they are Al_6(Mn, Fe, Cr) phase and Al_3Mg_2 phase (β-phase), respectively. Figure 4.14(d) is a HAADF image, with corresponding Fast-Fourier Transform (FFT) as an inset, and accompanied by an EDS line scan of a similar area in this sample. The pattern was indexed and matches well the simulated d-spacings for Al_3Mg_2 [101]. The EDS line scan indicates that the two bright particles are both rich in Mn, and that the dark region is rich in Mg. Quantification of the area marked by the solid red box gives an atomic ratio of 3:2 (Al:Mg). Similar β-phase precipitation was also observed in the sample heat treated at 70°C for 1 year, which is presented in Figure 4.15, including electron image and maps. The Mn-rich zones are dispersed into several pieces, between which the volume is filled with β-phase. STEM-EDS quantification results are listed in Tables 4.7 - 4.12.

4.9 Effects of Dislocations on β-phase Precipitates

Compared to the β-phase along grain boundaries discussed above, the β-phase in some regions grew much thicker, even thicker than the Zener-Hillert diffusion model predicted value which is 50-55 nm in the present condition, which suggests an alternative diffusion mechanism besides volume diffusion to account for the rapid growth of this type of β-phase. Evidence is provided by the observation of a high density of dislocations connected to the thicker β-phase precipitates in the matrix of the sample exposed for 15 days at 175°C. In Figure 4.16(a) a group of dislocation loops partially enclosed by the dotted-green rectangle/box is present starting from the node (diameter is 170-230 nm based on measurement in Figure 4.16(b)) at the top-left corner, across the elongated particle (around 100 nm thick and 470 nm long) with slightly darker contrast, and ending beyond the images. EDS quantification of the composition of the node (see the area in the solid red box Figure 4.16(b)) showed that Mg concentration is around 27 wt. %, which is slightly lower than the 37 wt. % Mg concentration in β-phase. This node is believed to be β′-phase, which is a semicoherent intermediate phase with hexagonal structure (a = 1.002 nm and c = 1.636 nm) [35]. This is consistent with the reports that β′-phase begins with nucleation at around 100°C and accelerates growth at around 150°C [17-18], and that dislocation loops in Al-Mg alloys provide nucleation sites for β′-phase [16, 19]. Quantification of the elongated particle (see the area marked by the solid red box in Figure 4.16(c)) showed that this particle is intragranular β-phase. There are no Mn-rich particles around it and the potential nucleation site should be dislocations that surround it.

The particles circled by the dashed yellow line in Figure 4.16 are rich in Mn, Fe and Cr. These particles are all connected to dislocation networks. The arrowed grain boundary in Figures 4.16(e) and 4.16(f) is filled with β-phase that is connected to dislocations. Its thickness is around 65 nm, which is much thicker than the value reported earlier (~45 nm). Therefore, it is concluded that dislocations make an important contribution to the diffusion of alloying elements (Mg, Mn, Fe, and Cr, etc.) and growth of β-phase. EDS quantification results of Figure 4.16 are listed in Tables 4.13 and 4.14.

A Zener–Hillert diffusion controlled growth model of planar interfaces in references[11, 25-26] is listed as follows:

$$T = \left[\frac{C_0 - C_e}{(C_p - C_e)^{1/2} \times (C_p - C_0)^{1/2}}\right] \times \sqrt{Dt}$$

$$D = D_0 \, exp(-Q/RT)$$

where,

T - Distance of interface growth, which in this case is the half thickness of the β-phase along planar grain boundary.

C_0 - Mg concentration in the matrix of the as-received sample, which is around 5 wt. %.

C_e - Equilibrium Mg concentration in the matrix of the heat treated sample, which in this case is the concentration in the matrix of the sample heat treated at 175°C for 15 days,

around 2.6 wt. % according to Al-Mg binary phase diagram.

C_p - Mg concentration in the β-phase, which is around 37.4 wt. %.

t - Diffusion time, which in this case is equal to 15 days.

D - Diffusion coefficient.

D_0 - $1.5\times10^{-5}m^2\ s^{-1}$.

Q - Activation energy, taken as 120 kJ. mol^{-1}.

R - The universal gas constant, which is 8.314 $J.mol^{-1}.K^{-1}$.

Based on the above equations and values of parameters, the thickness of β-phase along planar grain boundary is calculated to be:

$$2*T = 50 - 55 \text{ nm at } C_e = 3\text{-}3.2 \text{ wt. \%}$$

This is thicker than all the observed β-phase thickness (up to 45 nm) along grain boundaries except the thickness of β-phase that is connected with dislocations. The dislocation-connected intragranular β-phase is much thicker.

In addition, it has been reported that β′-phase precipitates first between 100°C - 250°C and then β-phase begins nucleation at around 200°C [17-18, 102]. However, in the present research, β-phase formed at 70°C and 175°C based on STEM imaging, EDS quantification and simulated diffraction pattern. Theoretically, β-phase formation at low temperature is a feasible process provided that the exposure time is sufficient. Figure 4.17 shows some non-equilibrium phase along grain boundary. As can be seen, there is grain boundary precipitate. The composition of it, based on the STEM-EDS line scan, is

mostly Mg and Al at a ratio of 1: 2, which is in between the composition of β′-phase and β-phase.

4.10 Pre-imaging and Pre-analysis of Orientation Relationship

Figure 4.18 shows dark-field image and selected area diffraction (SAD) images of the 5083-H131 alloy sample heat treated for 20 months at 70°C. The phase along grain boundary, the bright area in Figure 4.18(a), is believed to be β-phase. The thickness of this grain boundary β-phase is around 30 nm, higher than the reported thickness value of around 15 nm from the 5083-H131 alloy sample heat treated for 12 months at 70°C. For a FCC Al matrix with its [011] crystal face being normal to the electron beam, several diffraction spots obtained from Al matrix were well indexed as shown in Figure 4.18(b). The one in the solid-red circle has a d-spacing of 1.976 Å, which is an exact match for Al_3Mg_2 (2 10 10) or (2 2 14) plane, however, the matrix has a spot at 2.02 Å, so it is likely a combination of the two (we would not expect the spot to be so intense and broad if it was only from the Al_3Mg_2). To make a convincing conclusion regarding orientation relationship between β-phase and Al matrix, more supporting evidence is needed.

4.11 Mg Composition Profile Based on EELS

Mg composition profiles away from grain boundary in one 5083-H131 alloy sample were measured and plotted as shown in Figures 4.19(a) and 1(b), and Table 4.15. The Mg composition was measured away from grain boundary area as indicated by the red arrow in Figure 4.19(a). Along that direction one point was selected for measurement

each 50 nm. As can be seen from Figure 19(b), the Mg composition decreases away from the grain boundary. The highest Mg composition is at the grain boundary area with the value of 31 wt. %, which is lower than that of pure β-phase. The Mg composition away from the grain boundary is even lower, but higher than that in Al matrix. It is believed that the area selected for Mg composition profile measurement is rich in Mg and the precipitate here is most probably non-equilibrium phase. Therefore, more EELS measurements are needed to obtain better Mg composition profiles, which can be used to compare to the model.

4.12 β-phase Measurement in 5083 and 5456 Alloys

The measurement results of β-phase thickness of 5083-H131 alloy samples using both SEM and TEM techniques are listed in Table 4.16. As is shown, SEM and TEM measurement results match each other pretty well for 5083-H131 samples.

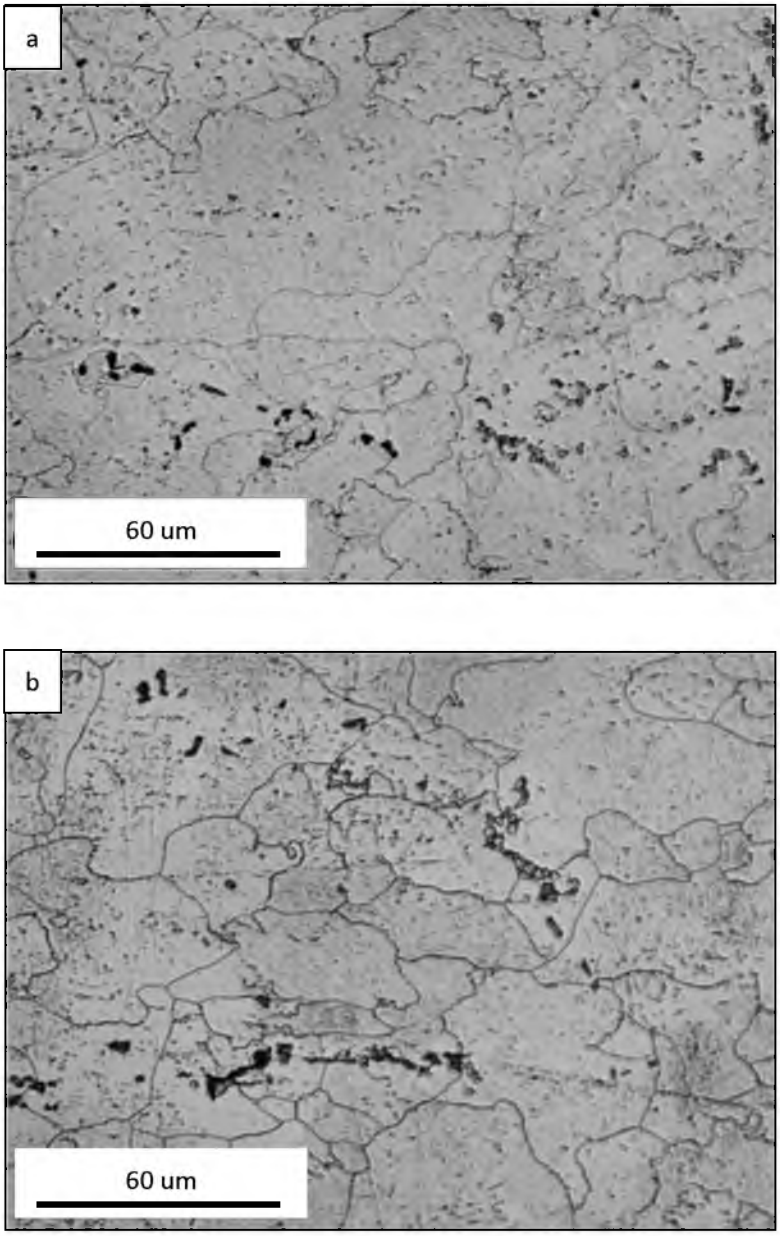

Figure 4.1 Optical images of 5083-H131 samples exposed at 150°C for (a) 48 hours and (b) 72 hours. Etching was carried out with 10 vol. % phosphoric acid at 50°C for 2 minutes.

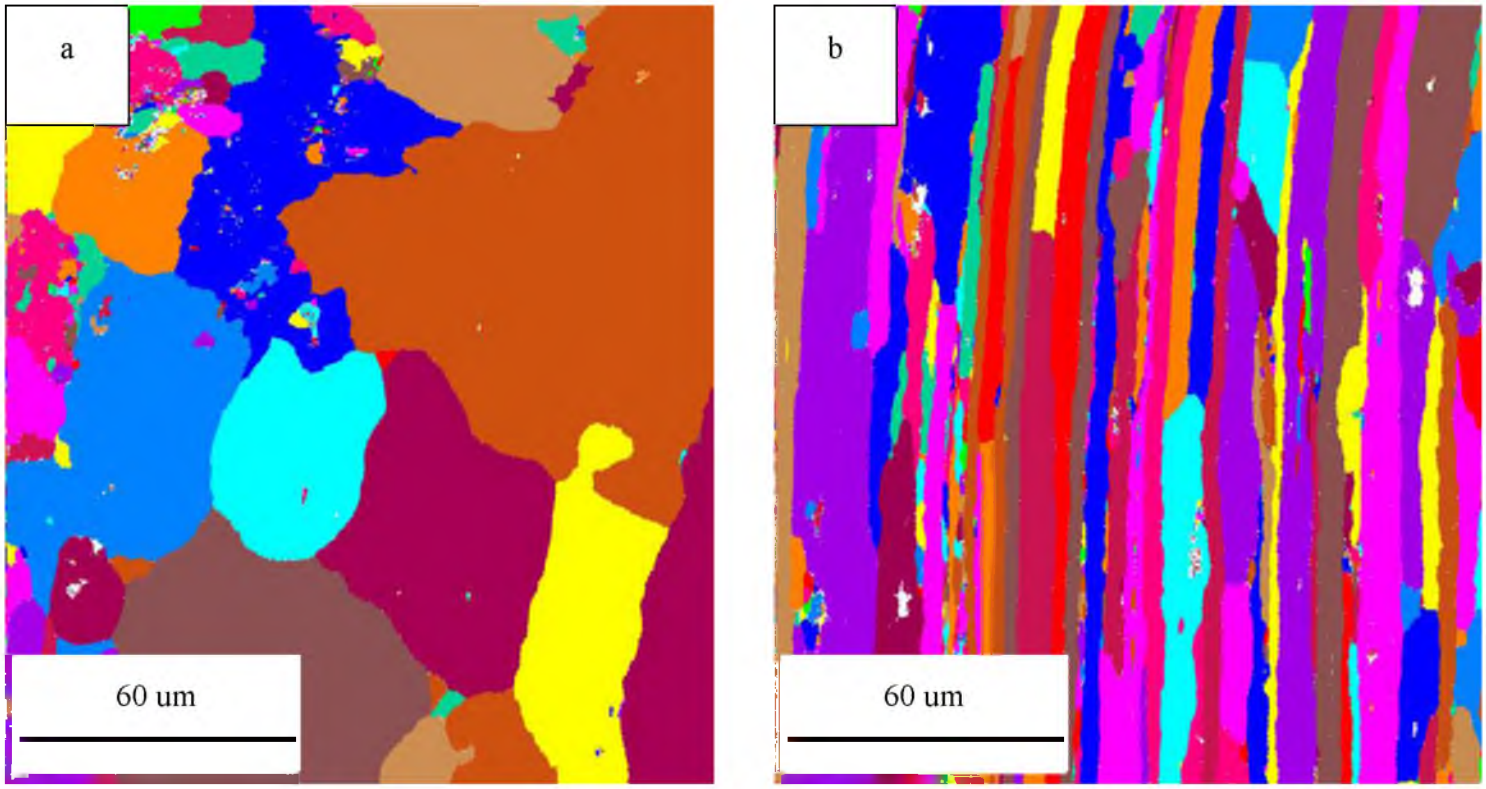

Figure 4.2 Different orientation view of the as-received rolled plate based on EBSD (a) LT surface (b) LST surface.

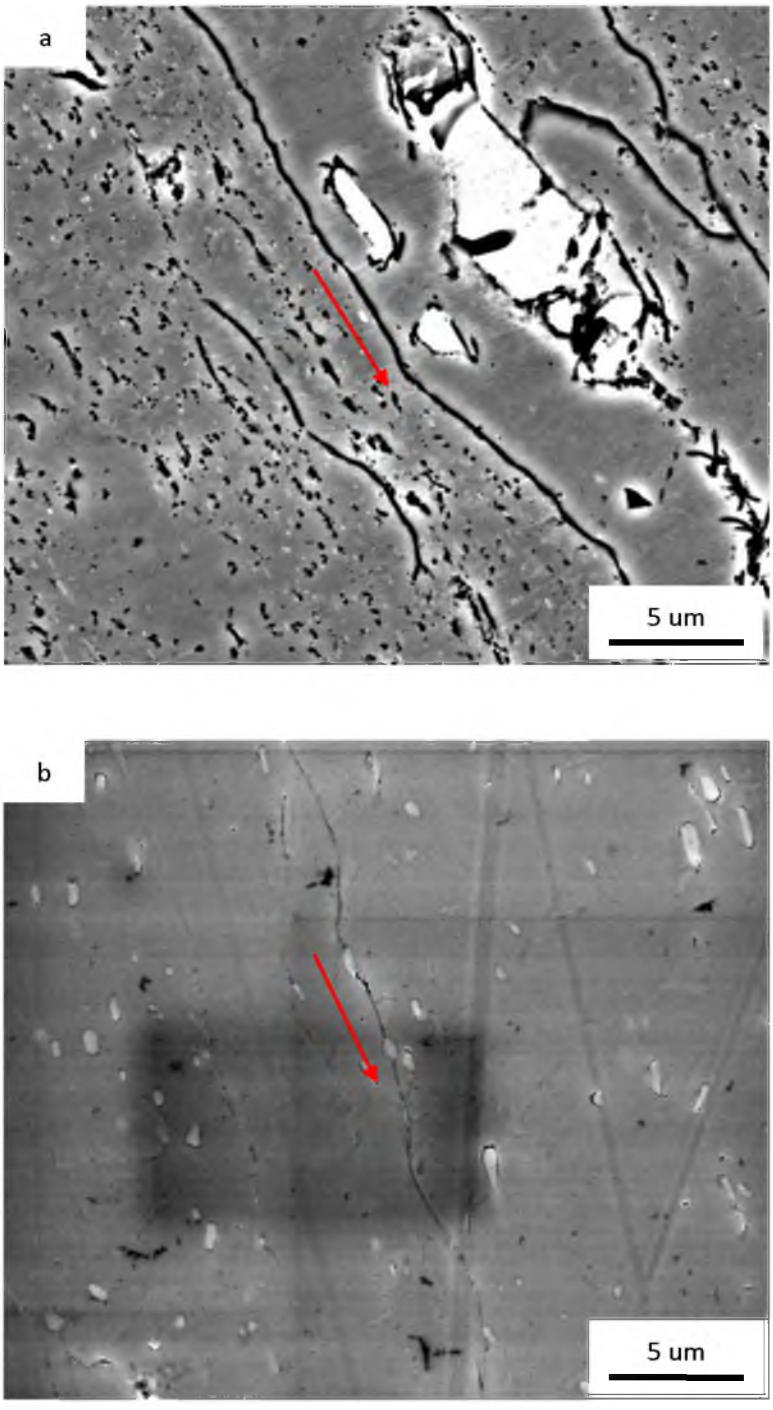

Figure 4.3 SEM images of 5083-H131 alloy sample aged at 70°C for 1 year; (a) phosphoric acid etching (b) ammonium persulfate etching. The red arrows are located parallel to and point along grain boundaries.

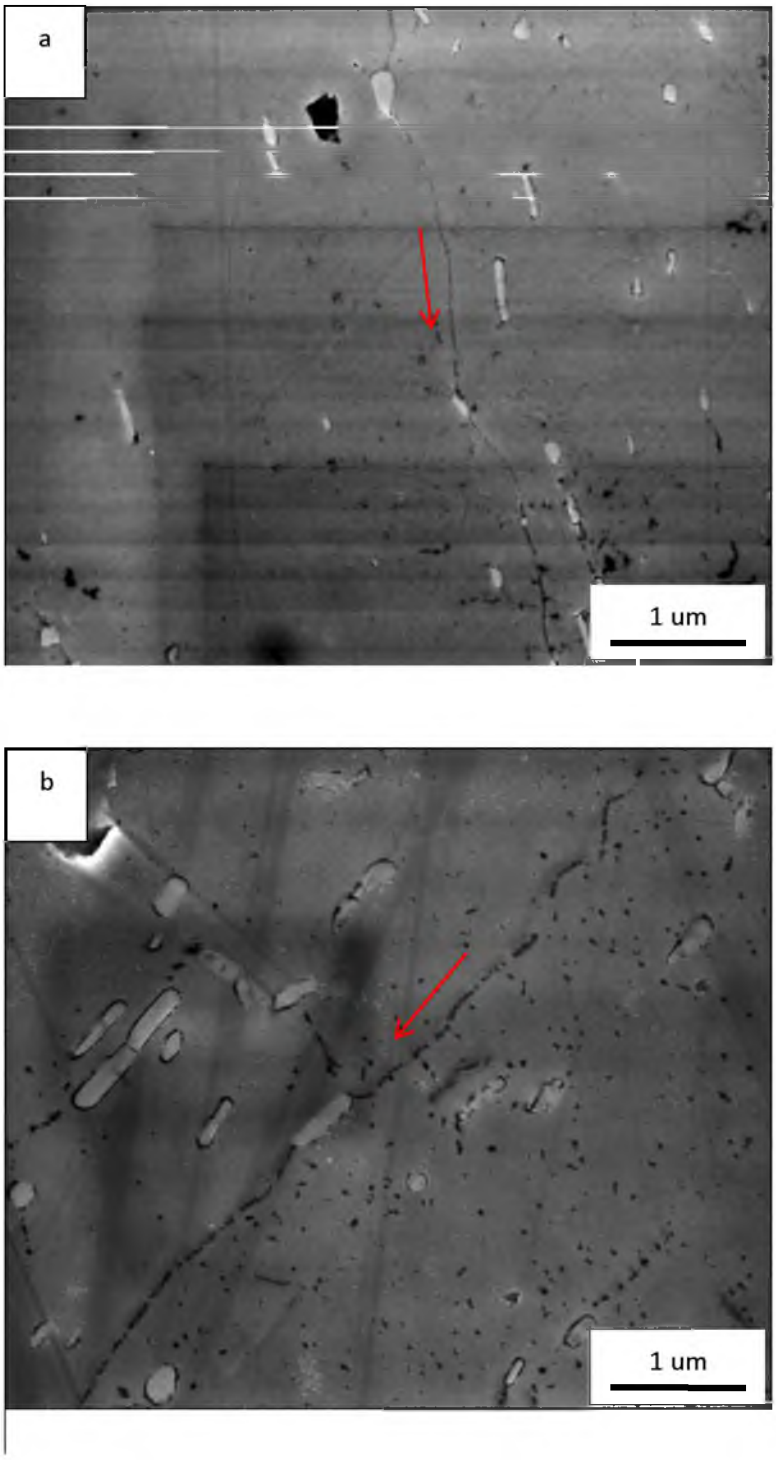

Figure 4.4 SEM images of the samples of (a) 5083-H131 alloy and (b) 5456-H116 alloy which were aged at 70°C for 1 year and etched using ammonium persulfate solution. White lines in Figure 4.4(a) are measurement grid lines. The red arrows are located parallel to and point along grain boundaries.

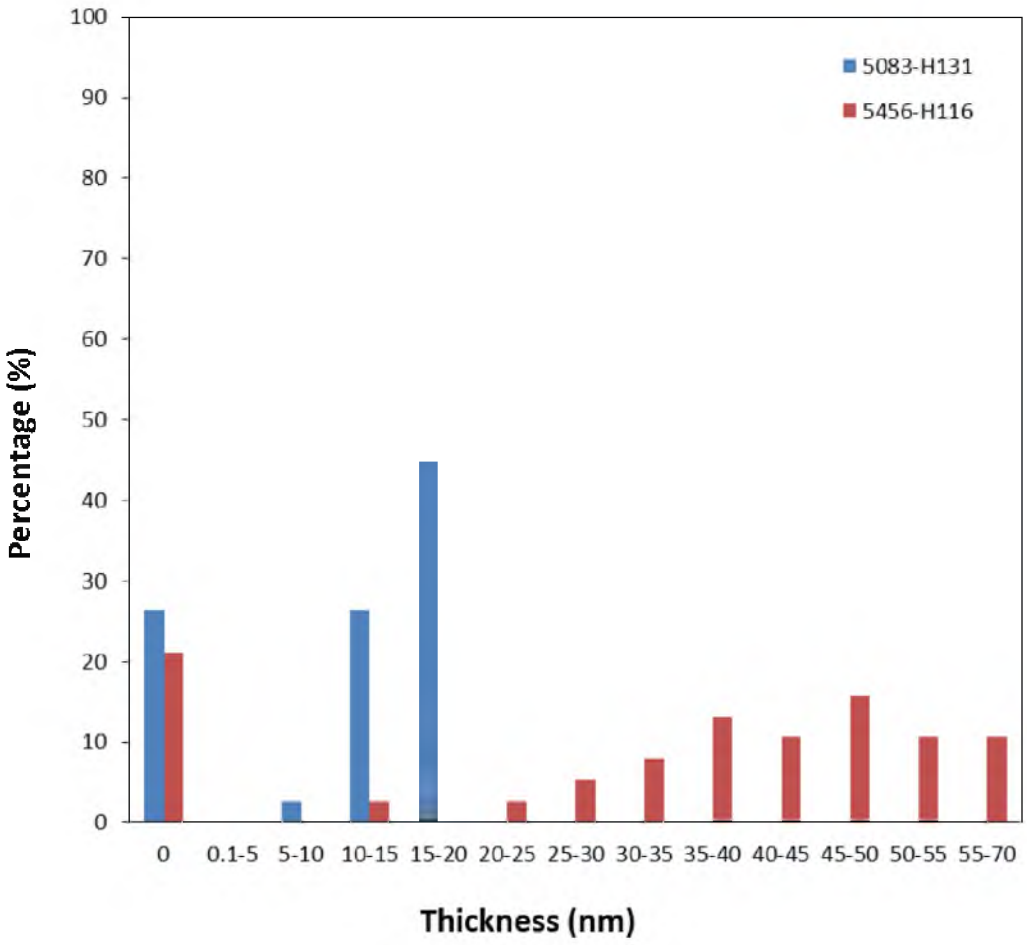

Figure 4.5 Thickness distribution profile of the β-phase corresponding to the two samples in Figure 4.4.

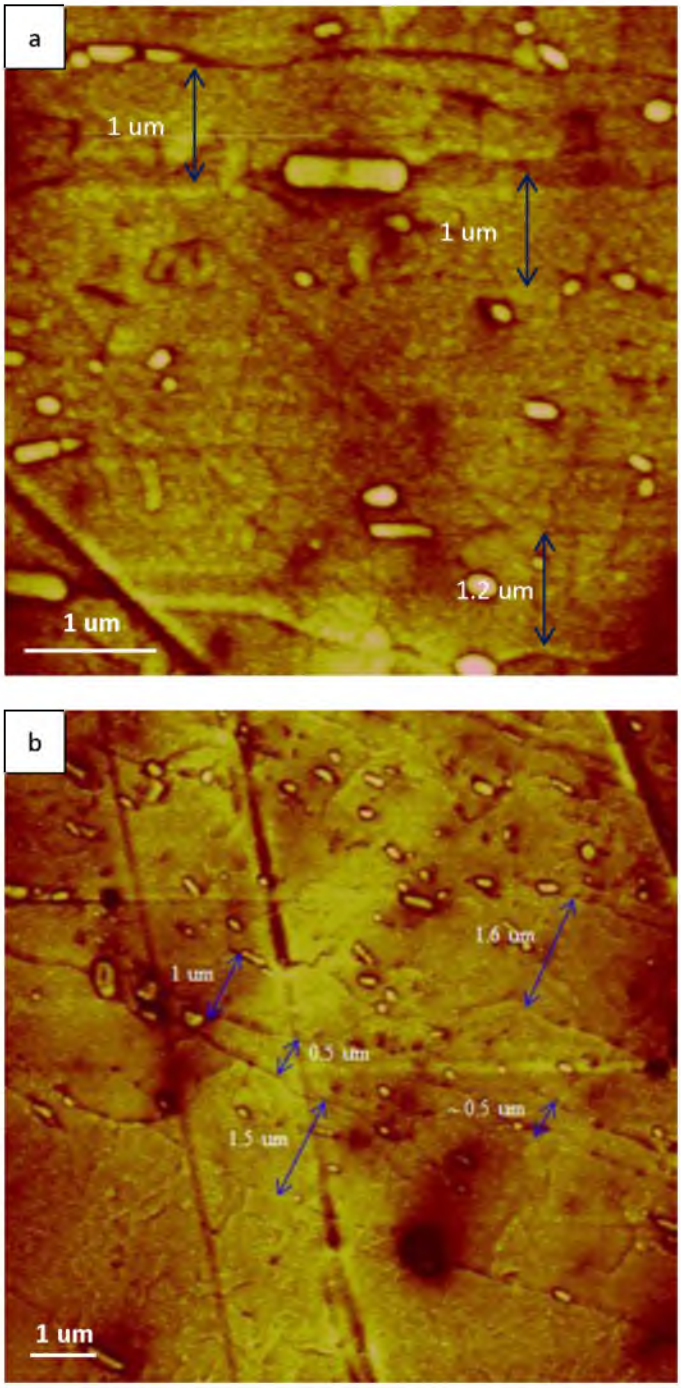

Figure 4.6 AFM images of (a) the as-received sample; and (b) the 5083-H131 sample aged at 70°C for 1 year.

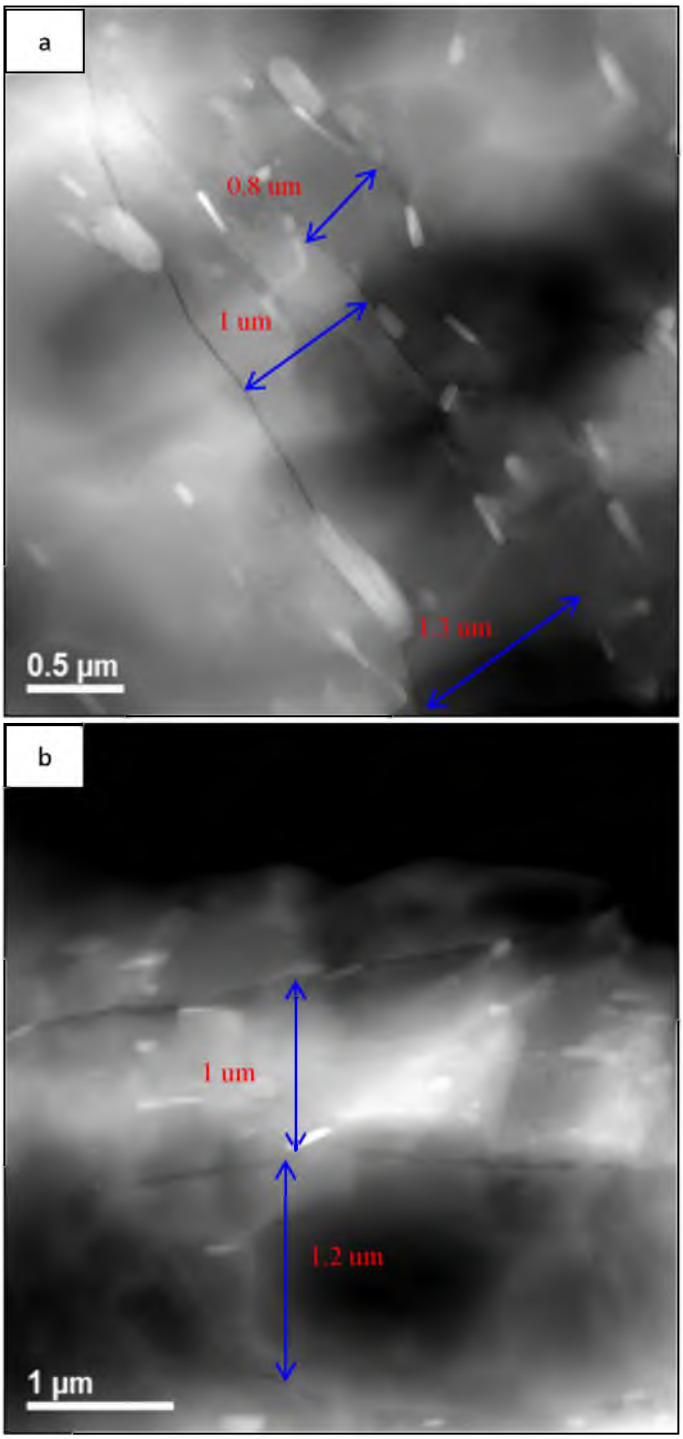

Figure 4.7 TEM images of (a) the 5083-H131 sample aged at 70°C for 1 year; (b) the sample aged at 175°C for 15 days.

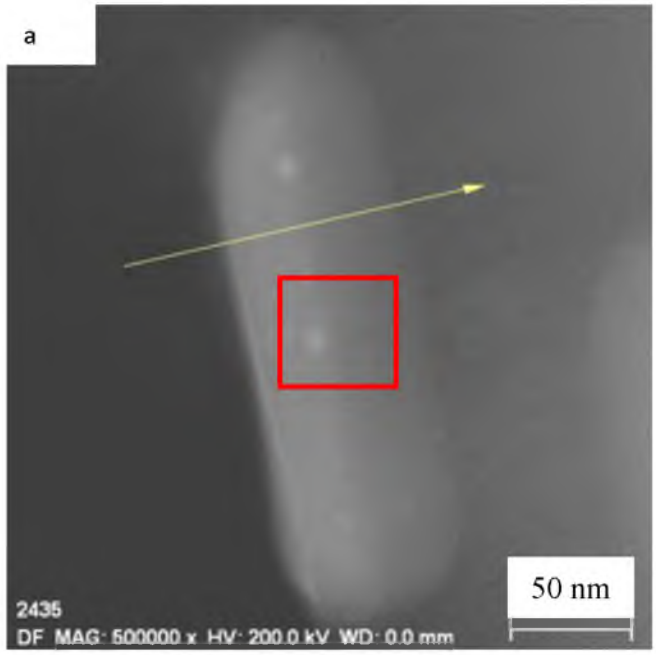

b

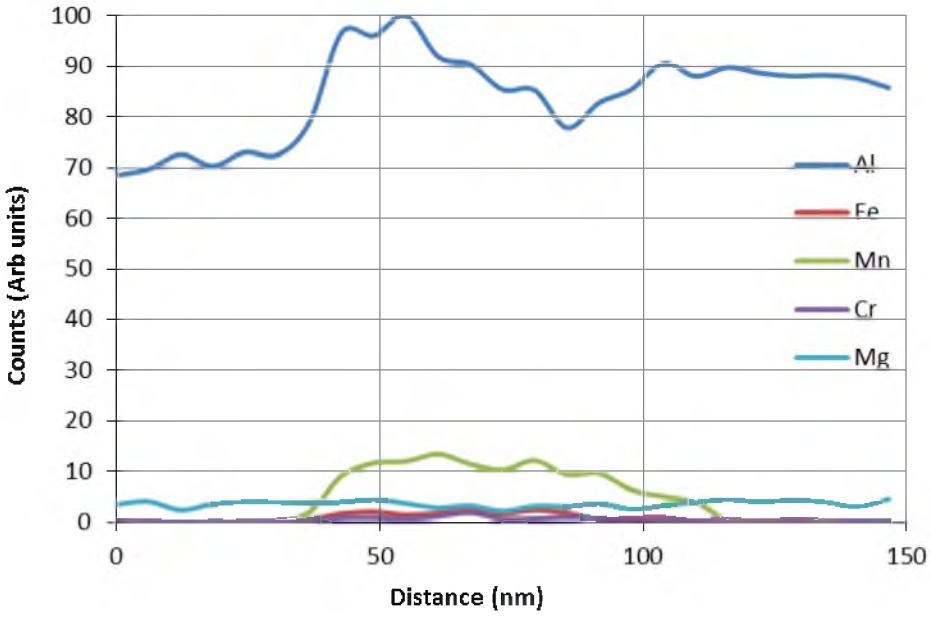

Figure 4.8 STEM-EDS line scan of rod-shaped particles in the as-received sample. The area in the solid red box was quantified by EDS.

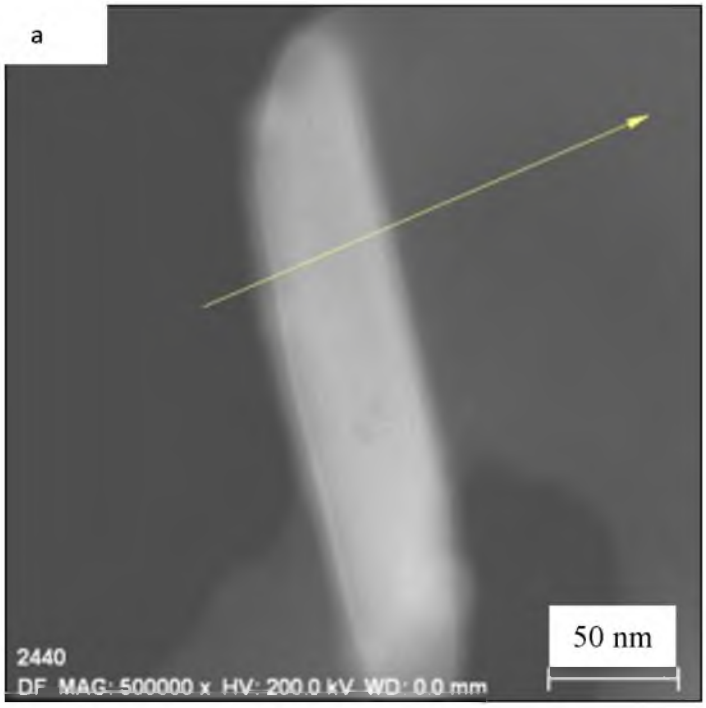

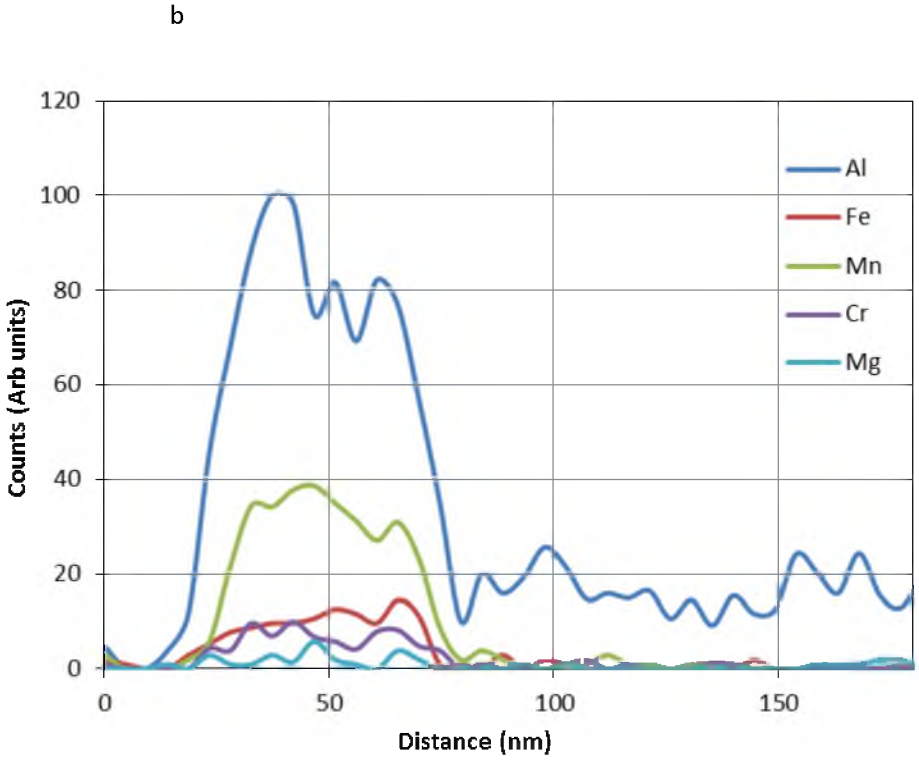

Figure 4.9 STEM-EDS line scan of needle shaped particles in the as-received sample.

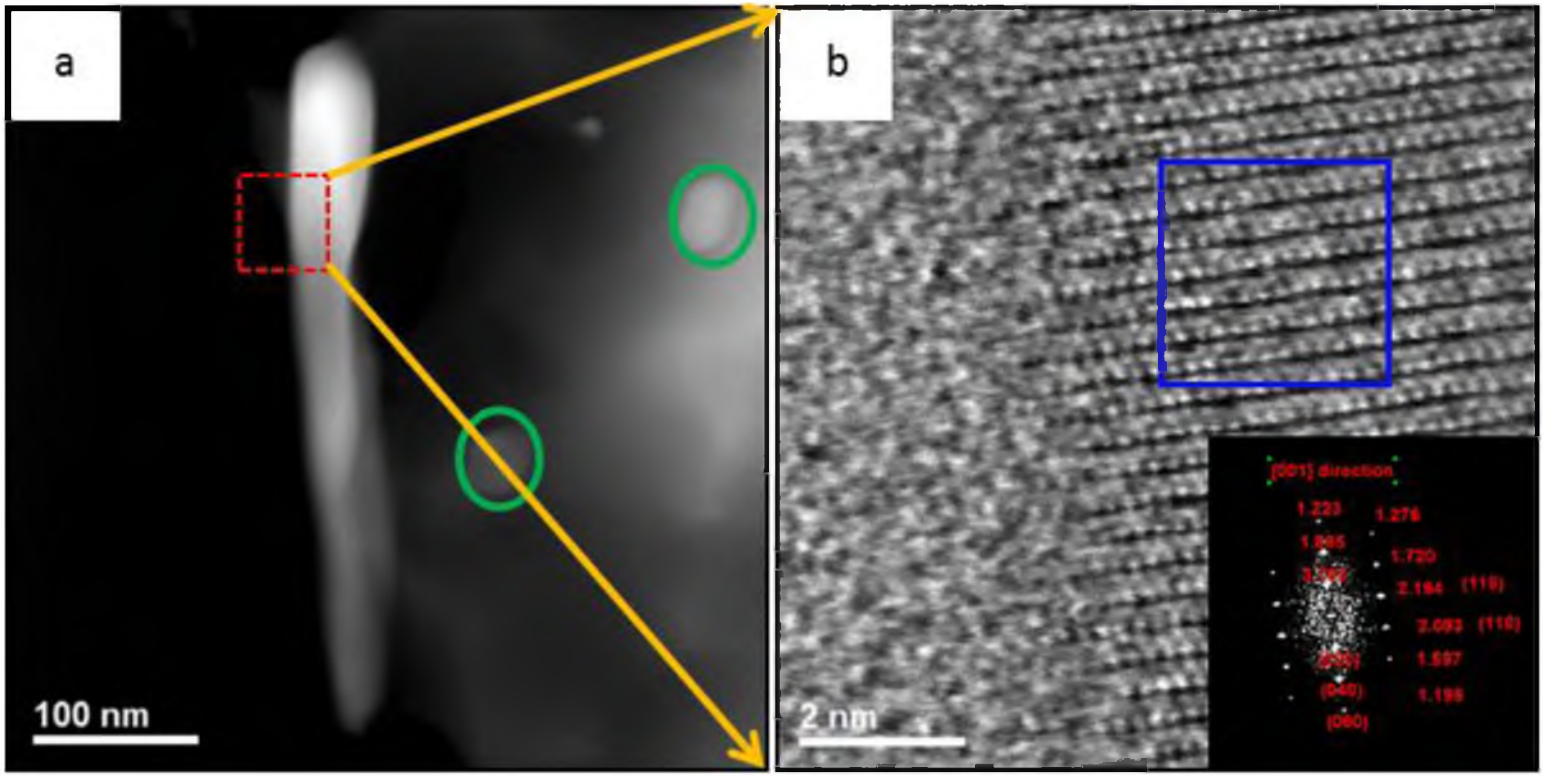

Figure 4.10 Needle shaped Mn particles indexed to be Al6Mn or Al_6(Mn-Fe-Cr).

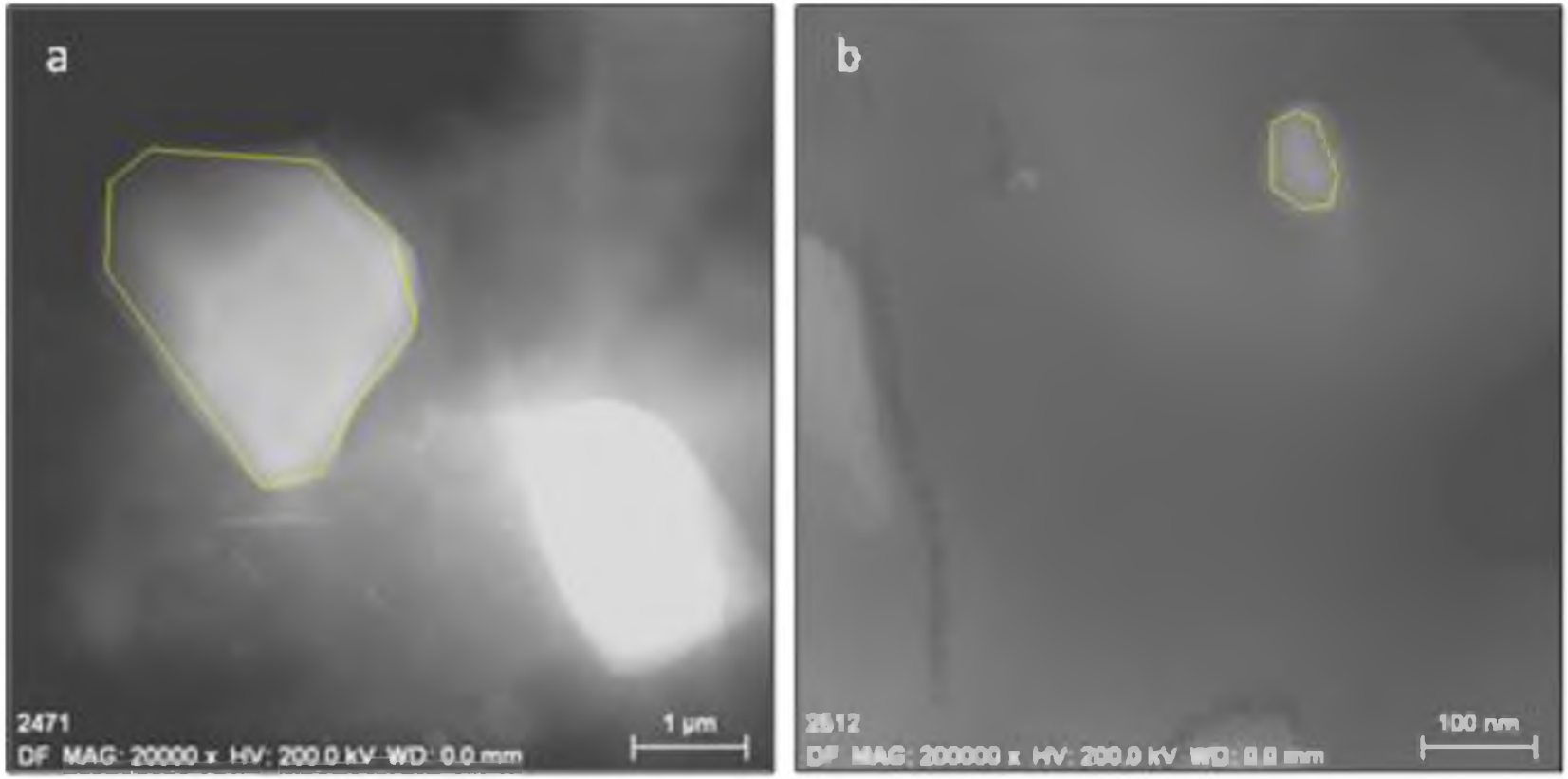

Figure 4.11 Equiaxed particles observed in the sample aged at 70°C for 1 year. The boxed yellow areas were quantified by STEM-EDS.

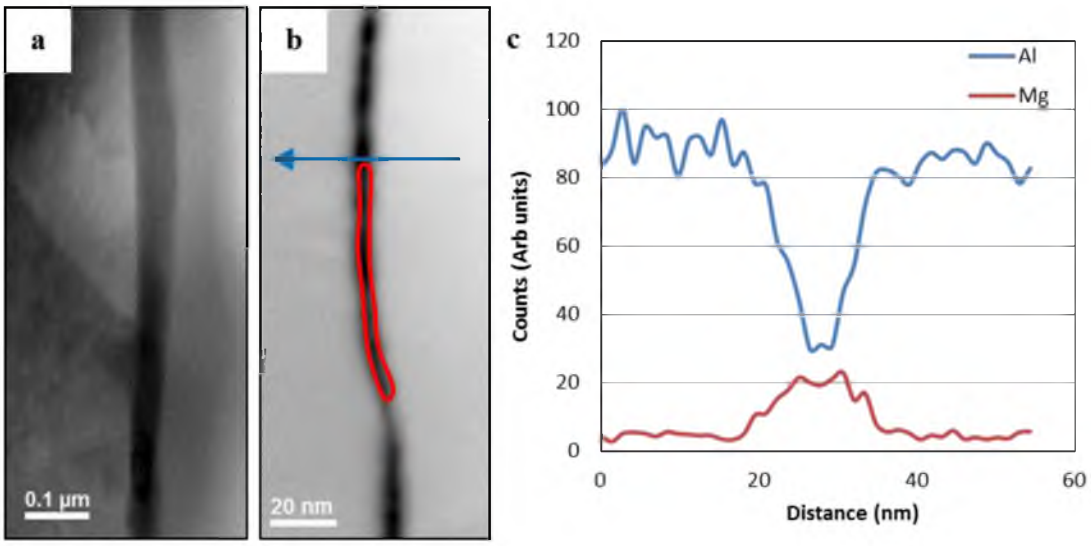

Figure 4.12 High-angle annular dark-field (HAADF) images of grain boundaries of the sample heat treated at (a) 448 K (175 °C) for 15 days, and of the sample heat treated at (b) 343 K (70 °C) for 1 year; (c) EDS line scan corresponding to the solid blue arrow in (b) showing an Al: Mg ratio of 3:2, indicating the grain boundary contains β-phase. The area in the solid red box was quantified by STEM-EDS.

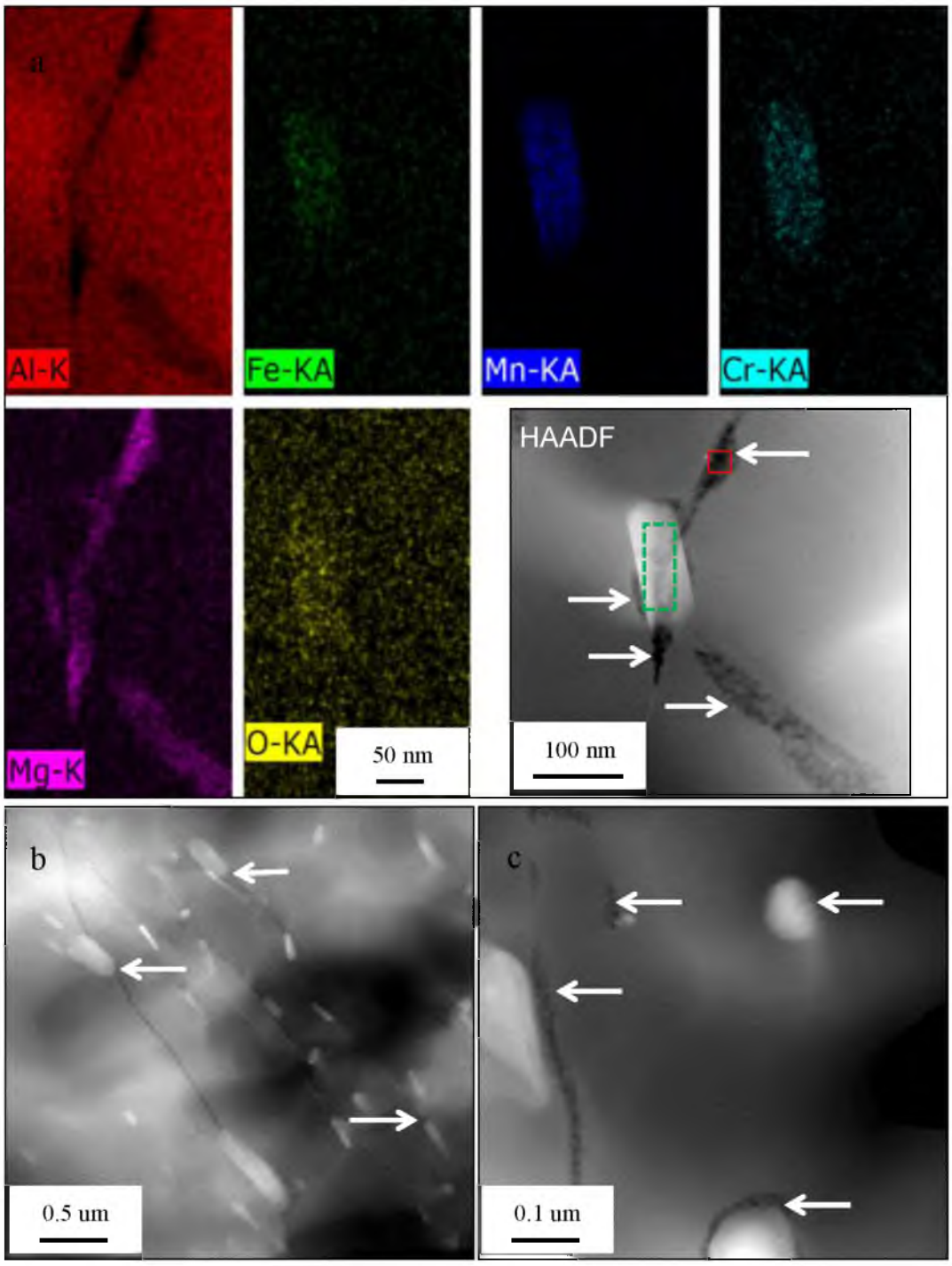

Figure 4.13 (a) A HAADF image of intergranular β-phase around Mn, Fe, and Cr rich particles, and corresponding EDS maps; (b) - (c) extra HAADF images of intergranular and intragranular β-phase. These images were taken from the sample heat treated at 343 K (70 °C) for 1 year. The β-phase is indicated by white arrows. EDS quantification areas are indicated by solid red and dotted green boxes.

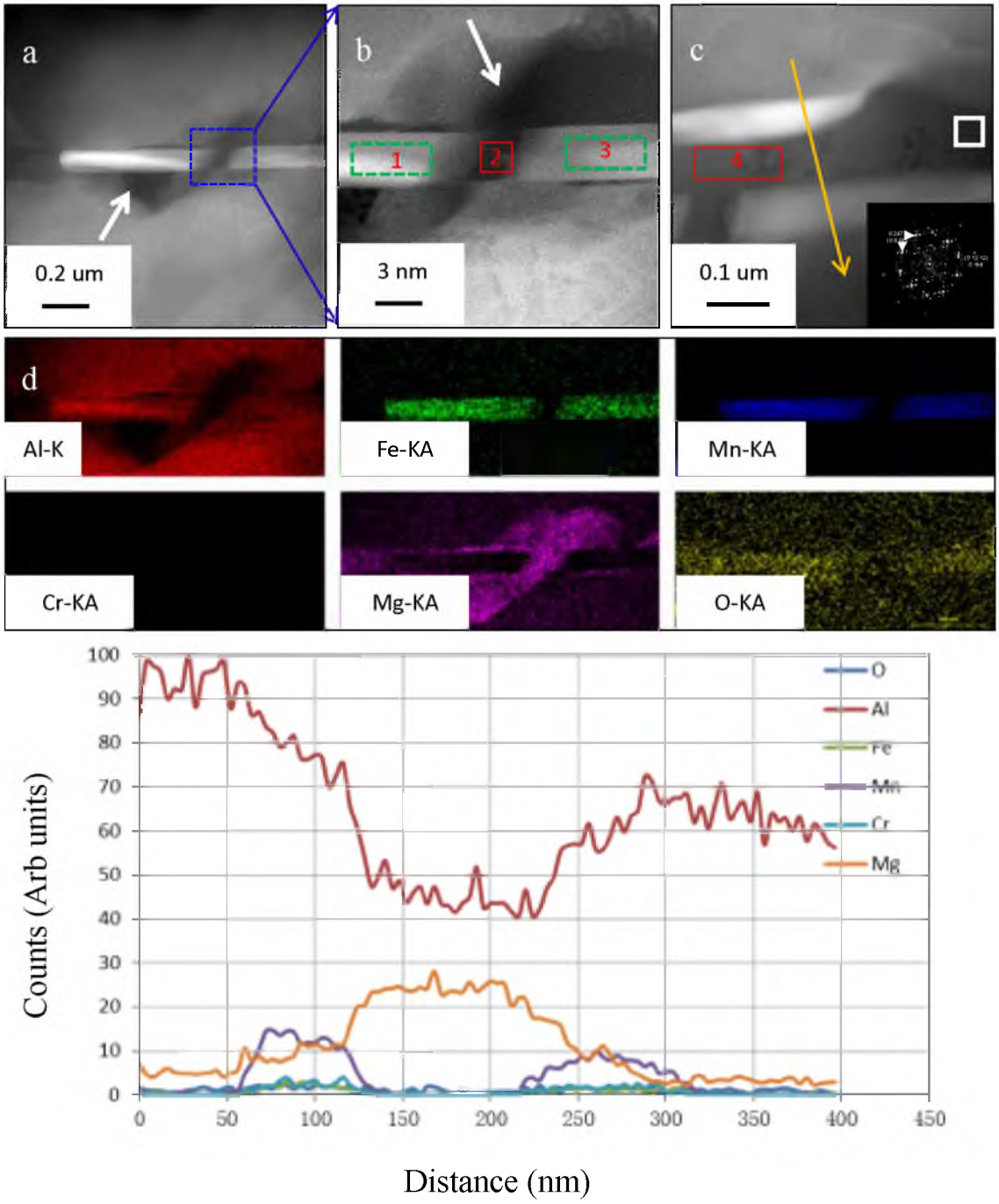

Figure 4.14 Images (a) - (d) were taken from the sample heat treated at 448 K (175 ºC) for 15 days: (a), (b), and (d) HAADF images and EDS mapping of intragranular β-phase around and between one Mn-rich particle; (c) HAADF image with FFT corresponding to solid white boxed area as an inset and EDS line scan (orange line) of intragranular β-phase around and between an Mn-rich particle. EDS quantification areas are shown by solid red and dotted green boxes, labeled as 1, 2, 3, and 4.

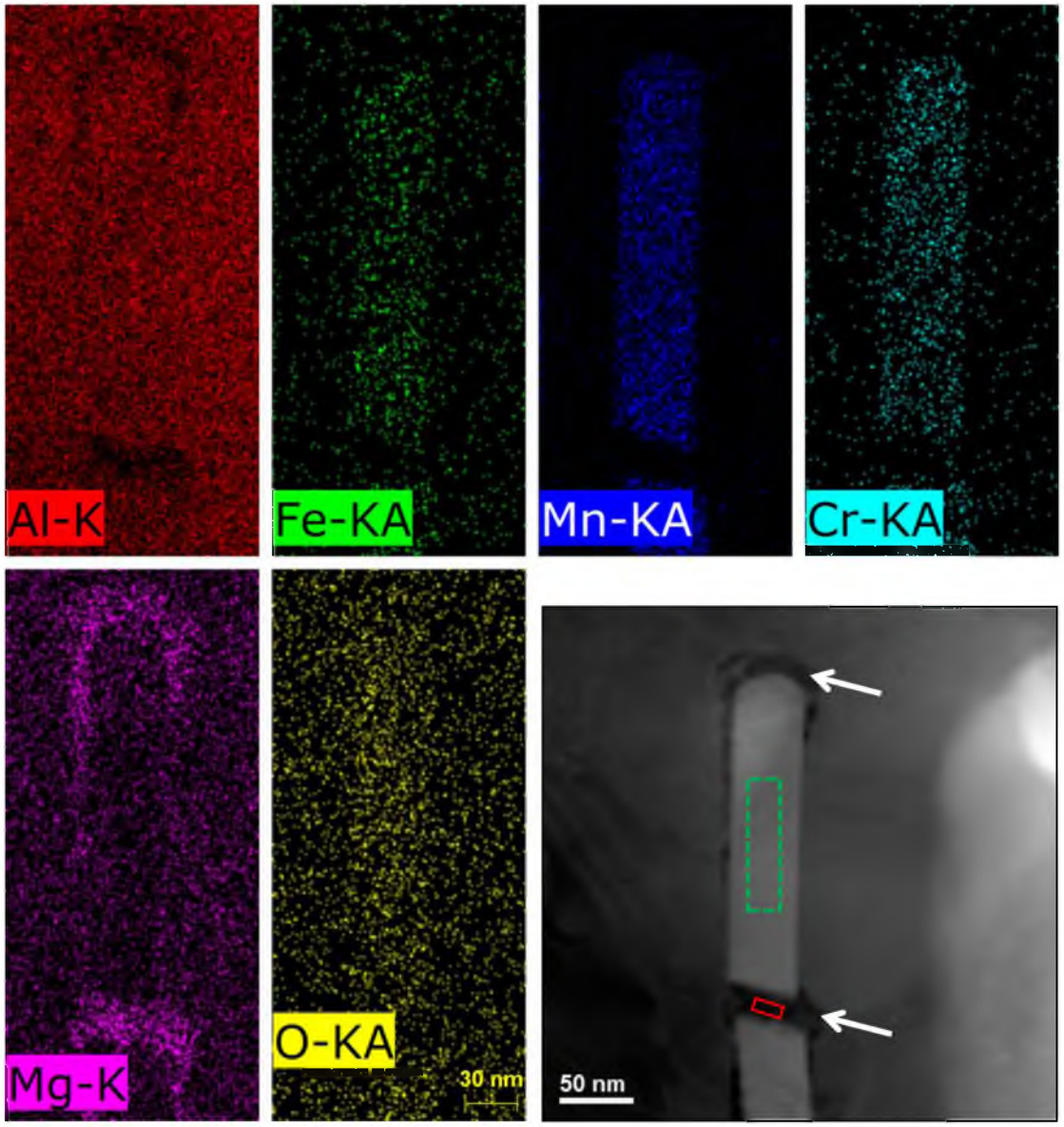

Figure 4.15 HAADF images of intragranular β-phase around and between one Mn-rich particle in 1-year heat-treated sample at 343 K (70 °C). White arrows indicate β-phase. EDS quantification areas are shown by solid red and dotted green boxes.

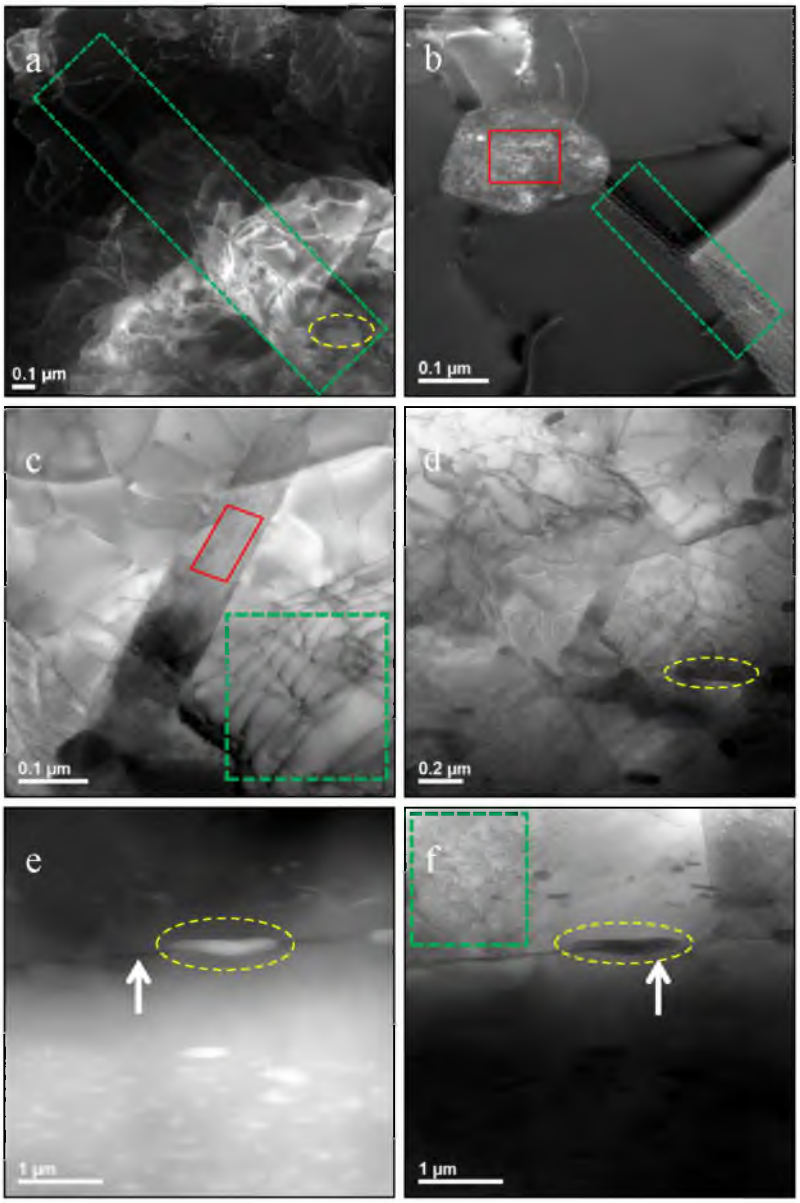

Figure 4.16 Bright-field images ((a)-(d), and (f)) and HAADF images ((e)) of high density of dislocations in the matrix of the sample heat treated at 448 K (175 ℃) for 15 days. Areas in dotted green boxes consist of high density of dislocations. Areas in solid red boxes are rich in Mg. Some Mn-rich particles are circled by dashed yellow lines. White arrows indicate grain boundary β-phase. EDS quantification results are listed in Tables 4.13-4.14.

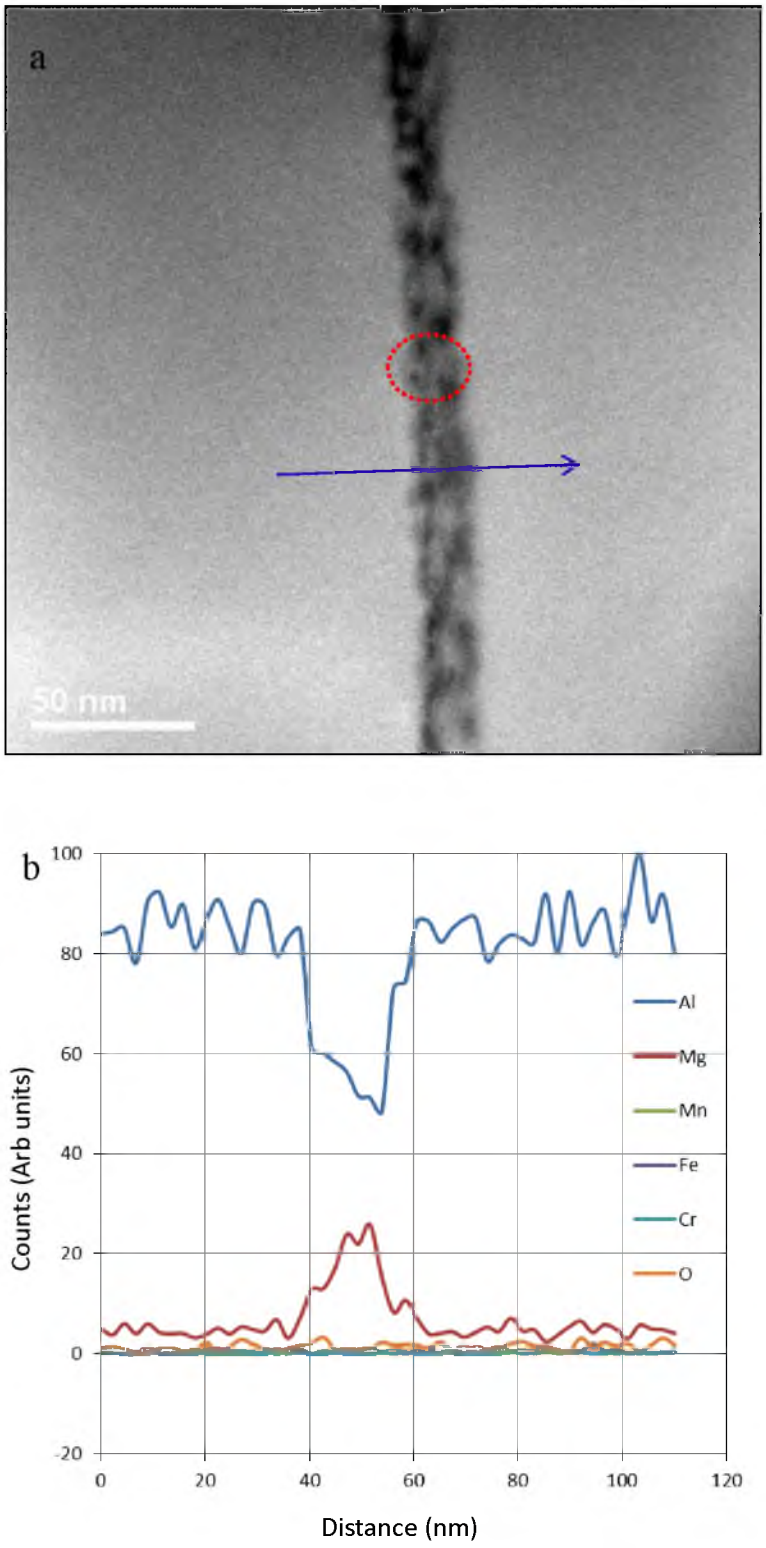

Figure 4.17 High-angle annular dark-field (HAADF) images of grain boundaries of the sample heat treated at 70°C for 1 year (a); (b) EDS line scan corresponding to blue line in (a).

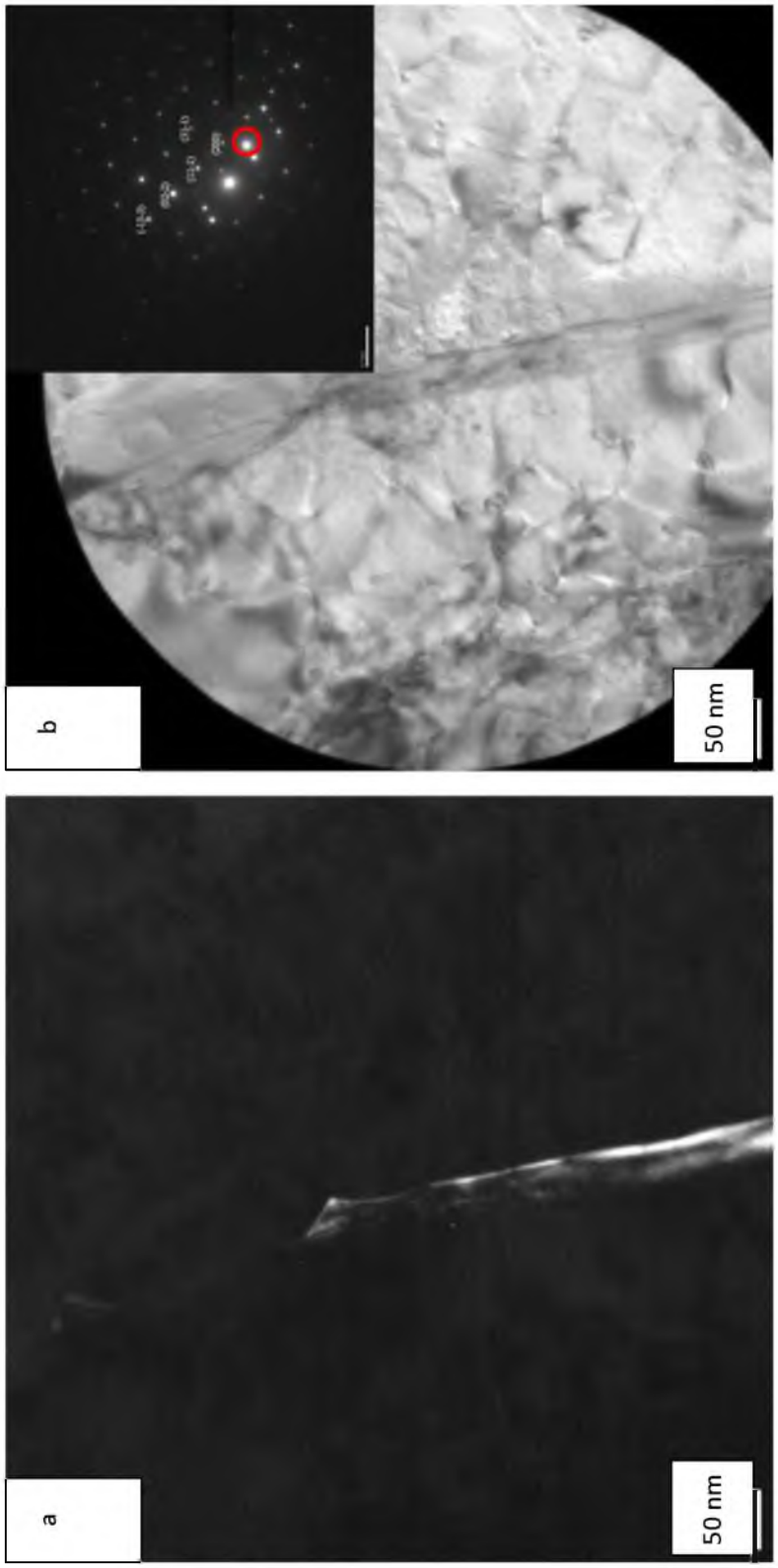

Figure 4.18 (a) Dark-field image and (b) selected area diffraction image with diffraction pattern as an inset of 5083-H131 alloy sample heat treated for 20 months at 70°C.

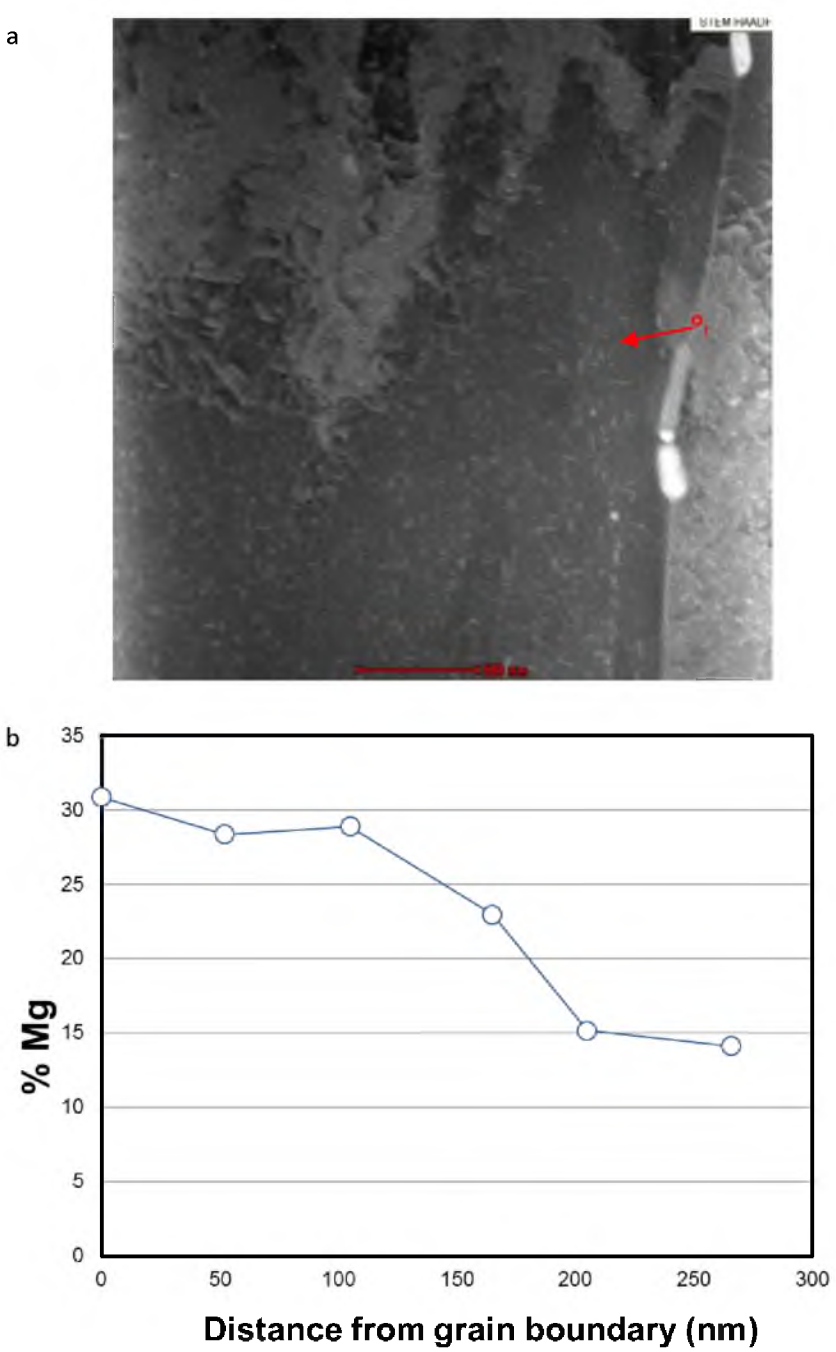

Figure 4.19 (a) STEM-HAADF image of 5083-H131 alloy sample aged at 70°C for 20 months; (b) Mg composition profile away from the grain boundary area in Figure 4.19(a). The red arrow in Figure 4.19(a) represents the direction of Mg composition (wt. %) measurement away from the grain boundary. Six points were picked up along this direction, as plotted in Figure 4.19(b).

Table 4.1 Results of Mg concentration measurement

	1	2	3	4	average
ICP-AES (wt. %)	4.80	4.77	4.90	4.89	4.85 ± 0.05
STEM-EDS (wt. %)	4.98	5.14	4.87	5.13	5.00 ± 0.15

Table 4.2 EDS quantification data of the region in the yellow box in Figure 4.11(a)

Element	[norm. wt.%]	[norm. at.%]	Error in %
Oxygen	0.2	0.4	0.1
Aluminium	73.9	84.0	2.3
Iron	13.1	7.2	0.5
Manganese	10.5	5.9	0.4
Chromium	0.5	0.3	0.1
Magnesium	1.8	2.2	0.1

Table 4.3 EDS quantification data of the region in the yellow box in Figure 4.11(b)

Element	[norm. wt.%]	[norm. at.%]	Error in %
Oxygen	4.4	7.6	0.4
Aluminium	77.5	80.5	2.6
Iron	1.4	0.7	0.2
Manganese	11.1	5.7	0.6
Chromium	1.6	0.9	0.2
Magnesium	4.0	4.6	0.3

Table 4.4 EDS quantification results of the grain boundary area in Figure 4.12(b)

Element	series	[norm. wt.%]	[norm. at.%]	Error in %
Magnesium	K-series	39.71872	41.2449	2.38537
Aluminium	K-series	60.28128	58.7551	3.169733

Table 4.5 EDS quantification data of Mn-Fe-Cr rich particle in Figure 4.13(a)

Element	[norm. wt.%]	[norm. at.%]	Error in %
Aluminium	80.6	86.5	2.6
Manganese	14.8	10.4	0.5
Chromium	3.8	2.6	0.2
Iron	0.8	0.5	0.1
	100	100	

Table 4.6 EDS quantification data of Mg-rich particle in Figure 4.13(a)

Element	series	[norm. wt.%]	[norm. at.%]	Error in %
Aluminium	K-series	60.9	58.4	2.5
Magnesium	K-series	39.1	41.6	1.8
	Sum:	100	100	

Table 4.7 EDS quantification data of Mn-Fe-Cr rich region in box 1 in Figure 4.14

Element	series	[norm. wt.%]	[norm. at.%]	Error in %
Aluminium	K-series	76.1	86.7	2.4
Manganese	K-series	18.4	10.3	0.7
Iron	K-series	5.5	3.0	0.3
	Sum:	100	100	

Table 4.8 EDS quantification data of Mg-rich region in box 2 in Figure 4.14

Element	series	[norm. wt.%]	[norm. at.%]	Error in %
Aluminium	K-series	64.9	62.5	3.9
Magnesium	K-series	35.1	37.5	2.6
	Sum:	100	100	

Table 4.9 EDS quantification data of Mn-Fe-Cr rich region in box 3 in Figure 4.14

Element	series	[norm.t.%]	[norm. at.%]	Error in %
Aluminium	K-series	73.9	85.3	2.4
Iron	K-series	5.4	3.0	0.4
Manganese	K-series	20.7	11.7	0.9
	Sum:	100	100	

Table 4.10 EDS quantification data of Mn-Fe-Cr rich region in box 4 in Figure 4.14

Element	wt.%	at.%	Error in %
Aluminium	63.9	61.5	2.0
Magnesium	36.1	39.5	1.1

Table 4.11 EDS quantification data of Mg-rich particle in Figure 4.15

Element	[norm. wt.%]	[norm. at.%]	Error in %
Magnesium	18.5	20.1	1.6
Aluminium	81.5	79.9	4.0
	100	100	

Table 4.12 EDS quantification data of Mn-Fe-Cr rich particle in Figure 4.15

Element	[norm. wt.%]	[norm. at.%]	Error in %
Aluminium	87.5	93.4	2.9
Iron	0.7	0.4	0.1
Manganese	10.6	5.6	0.6
Chromium	1.2	0.6	0.2
	100	100	

Table 4.13 EDS quantification data of Mg-rich region in the red box in Figure 4.16(b)

Element	series	[norm. wt.%]	[norm. at.%]	Error in %
Oxygen	K-series	4.0	6.4	0.3
Aluminium	K-series	69.0	65.8	2.2
Iron	K-series	0.8	0.4	0.1
Manganese	K-series	0.5	0.2	0.1
Chromium	K-series	0.2	0.2	0.1
Magnesium	K-series	25.5	27.0	0.9
	Sum:	100	100	

Table 4.14 EDS quantification data of Mg-rich region in the red box in Figure 4.16(c)

Element	series	[norm. wt.%]	[norm. at.%]	Error in %
Aluminium	K-series	61.0	58.5	2.9
Magnesium	K-series	39.0	41.5	2.1
	Sum:	100	100	

Table 4.15 EELS measurements of Mg composition away from the grain boundary

Position (nm)	0	52	105	165	205	266
%Mg	30.86	28.34	28.90	22.96	15.16	14.1

Table 4.16 The results of β-phase thickness measurement

Temp.	TEM	SEM[1]	Time (days)
70 °C	7.5	8	125
70 °C	10	11	365
100 °C	13.7	15	45
175 °C	43	40	15

CHAPTER 5

INTERGRANULAR CORROSION OF 5083 AND 5456-H116 ALLOYS

In this chapter, the IGC susceptibility of 5XXX alloys at various sensitisation conditions is evaluated using NAMLT. The IGC susceptibility as a function of sensitization time and temperature is discussed.

5.1 Cross Section Imaging of NAMLT Samples

The surface morphologies of the sensitized samples after the NAMLT are shown in Figure 5.1. As can be seen, both the transverse-short transverse (TST) surface and the transverse direction longitude-short-transverse (LST) surface lost more mass from the nitric acid attack than the longitude-transverse (LT) surface. The TST and LST surfaces experienced significant exfoliation of grains, which is believed to be due to the effect of preferred etching of an almost continuous β-phase network along the grain boundaries [10]. This phenomenon may also be related to the near-surface stress distribution, which resulted from metal rolling processing on these surfaces, as well as the grain dimensions and grain orientations relative to each exposed surface, such that, nitric acid attacked TST and LST surfaces preferentially. However, this inequality in nitric acid attack on

sample surfaces has no effect on the comparison of mass-loss values of different samples since all the tested samples have the same dimensions relative to each surface. In addition, it is reported that although the nitric acid attack is uneven on sample surfaces, mass-loss values are not affected greatly by the difference in sample shape [103].

The images in Figure 5.1 also indicate that the total mass-loss of the sample is partially attributed to the corrosion of the matrix, which is usually believed to be the result of the preferential attack of the β-phase along grain boundaries leading to grain exfoliation. However, it has not been possible to calculate the fraction of the mass-loss induced by the matrix corrosion in the NAMLT thus far [10].

5.2 NAMLT of Constant Thermal Exposed Sample

The effects on sensitization of times (~ 18 months), temperatures (40 to 70°C) and alloying composition were investigated using ASTM G67 mass-loss tests, as shown in Figures 5.2-5.6. Figure 5.2 indicates the effect of heat treatment times and temperatures on the mass-loss results of 5083-H131 alloy samples. Mass-loss generally increased with increasing thermal exposure time and/or temperature before depletion of Mg was observed in the matrix. Specifically, the mass-loss results from samples heat treated at 60°C and 70°C in Figure 5.2 almost reached a plateau, which is an indication of Mg depletion in the matrix and an apparent acceleration effect of temperature on Mg diffusion.

The relationship between sensitization and alloy composition was evaluated using

four different aluminum alloys: 5083-H131, 5083-H321, 5083-H116 and 5456-H116. Because of the high concentration of Mg in alloy 5456-H116, much more β-phase formed, which resulted in the highest mass-loss amongst the four alloys, as indicated in Figures 5.3-5.6. Compared to the temper of H131, the reduced amount of defects in H321 and H116 temper, such as dislocations and stacking faults, that might be potential nucleating sites for β-phase, suggests 5083-H321 and 5083-H116 alloy samples had lower mass-loss. However, it is difficult to tell which one had higher mass-loss between 5083-H321 and 5083-H116 alloys. Note that at 50°C in Figure 5.5, the mass-loss values of all four alloys show a sharp linear relationship with increased exposure time, indicating the rapid onset of β-phase precipitation along the grains because of the high Mg gradient at the initial stage between the matrix and the saturation line in Al-Mg binary phase diagram and thus, the high diffusion driving force. The mass-loss of the 5083-H116 alloy exhibits a linear relationship with increased exposure time by far, regardless of the exposure temperature, which is consistent with results previously reported [104-106]. The dashed orange lines in Figure 5.2 are a classification of the degree of sensitization: unsensitized (< 15 mg/cm^2), indeterminate (15 mg/cm^2 – 25 mg/cm^2), and sensitized (> 25 mg/cm^2).

5.3 NAMLT of Cyclic Thermal Exposed Sample

As mentioned earlier, a program was written and applied to the operation of the thermal exposure furnaces and related devices to represent the heating and cooling cycles

experienced by naval ships during the hottest 6-hour period of the day. Data indicated that typical March days near the Panama Strait had a 40 to 45°C variation during the hottest part of the day for mounted, coated aluminum panels. However, some days had maximum temperatures of 65°C in March and April. Thus, to adequately simulate appropriate temperature ranges, a set of tests was conducted using a 40 to 45°C range, and another set was conducted using a 50 to 70°C range. Figure 5.7 shows that mass-loss generally increased with an increase in either thermal exposure time or temperature. A linear relationship with increased exposure time indicates the onset of β-phase precipitation along grain boundaries at the initial stage, which is similar to that for samples in constant thermal exposure tests.

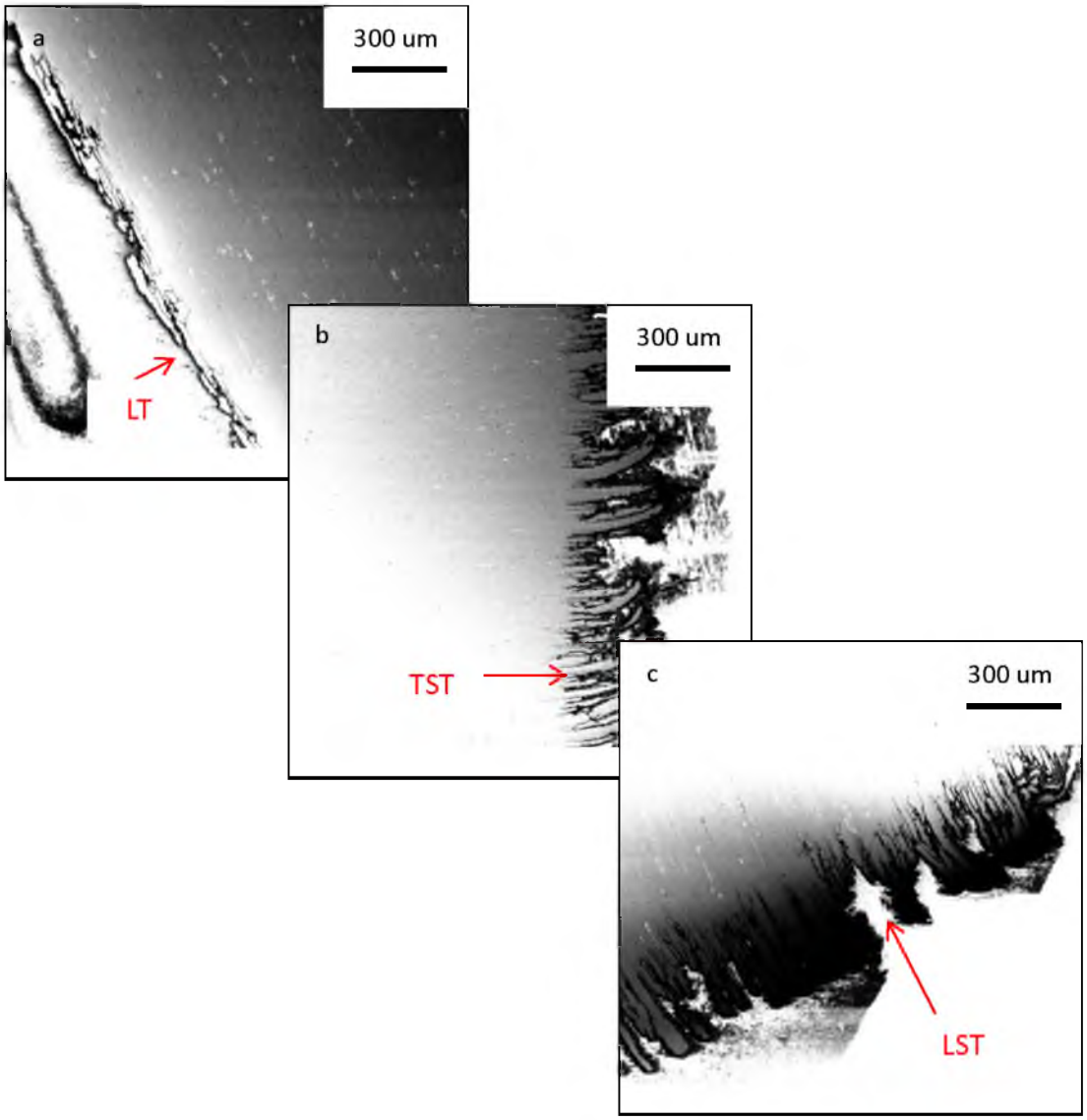

Figure 5.1 Cross sections of ASTM G67 mass-loss test sample of 5083-H131 alloy heat treated at 70°C for 9 months: (a) ND surface, normal to ND; (b) RD surface, normal to RD; (c) TD surface, normal to TD. ND: normal direction; RD: rolling direction; TD: transverse direction. Red arrows in the figure represent directions.

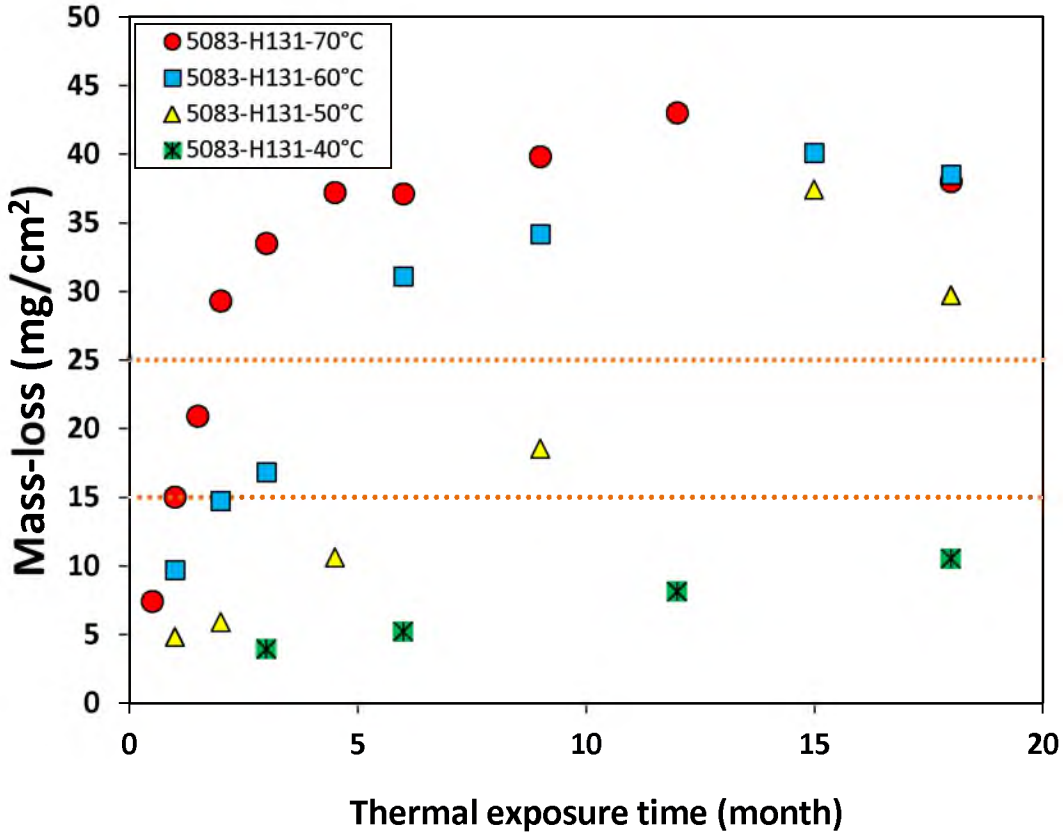

Figure 5.2 ASTM G67 mass-loss tests results of 5083-H131 alloy samples as functions of heat treatment times (up to 18 months) and temperatures of 40°C, 50°C, 60°C, and 70°C. Dotted green lines are the classifications of degree of sensitization as mentioned earlier.

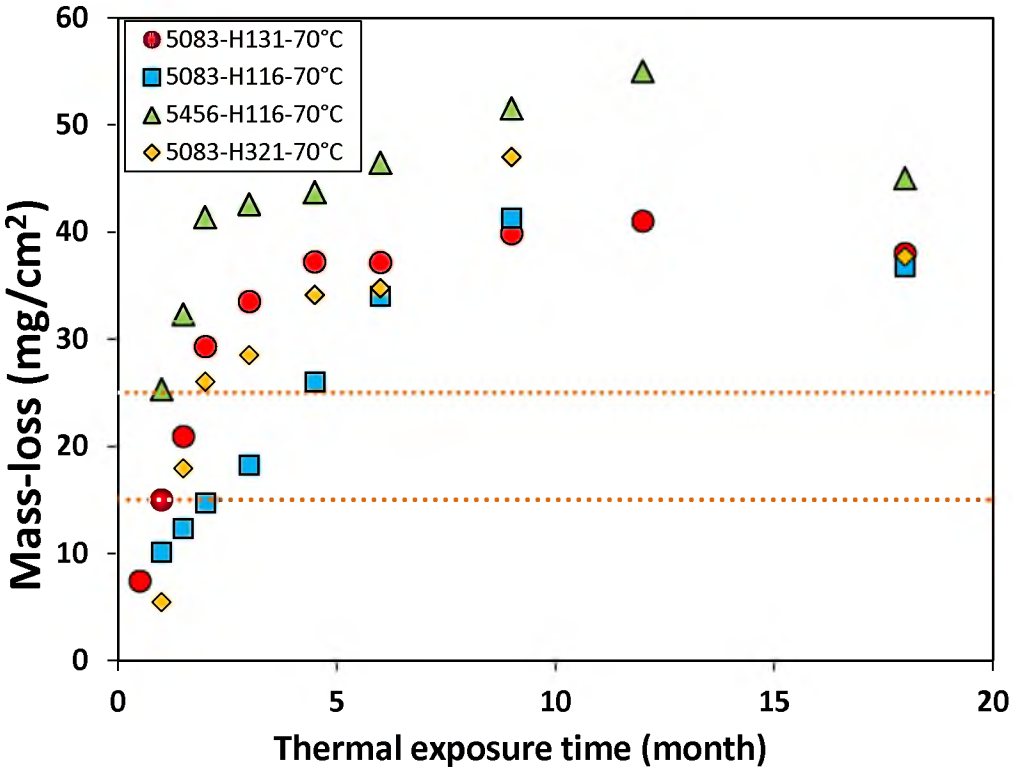

Figure 5.3 ASTM G67 mass-loss tests results of 5083-H131, 5083-H321, 5083-H116, and 5456-H116 alloys as functions of heat treatment times (up to 18 months) at the temperature of 70°C.

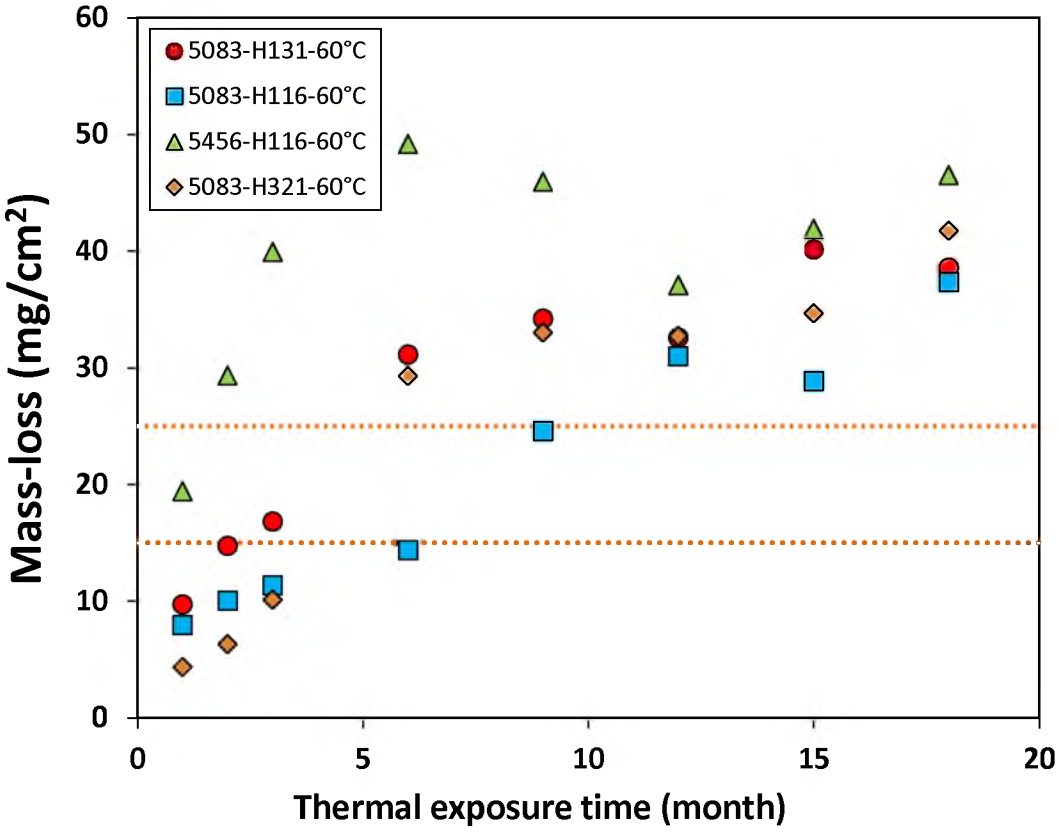

Figure 5.4 ASTM G67 mass-loss tests results of 5083-H131, 5083-H321, 5083-H116, and 5456-H116 alloys as functions of heat treatment times (up to 18 months) at the temperature of 60°C.

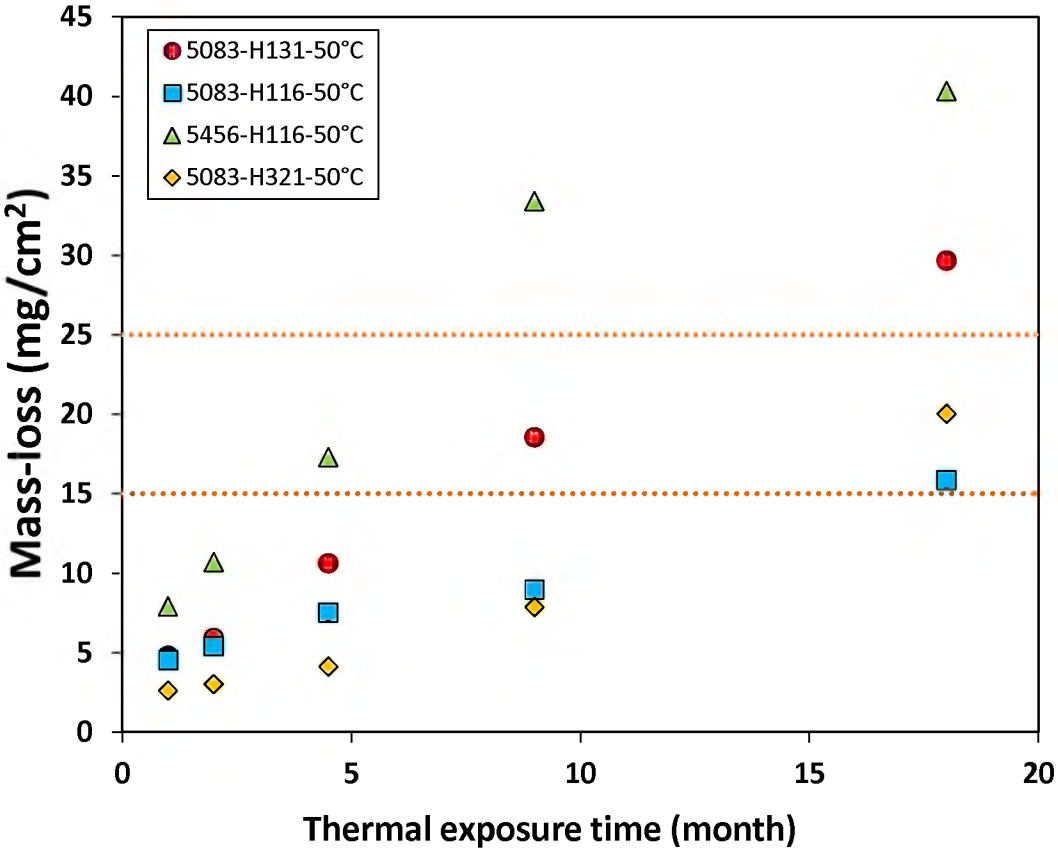

Figure 5.5 ASTM G67 mass-loss tests results of 5083-H131, 5083-H321, 5083-H116, and 5456-H116 alloys as functions of heat treatment times (up to 18 months) at the temperature of 50°C.

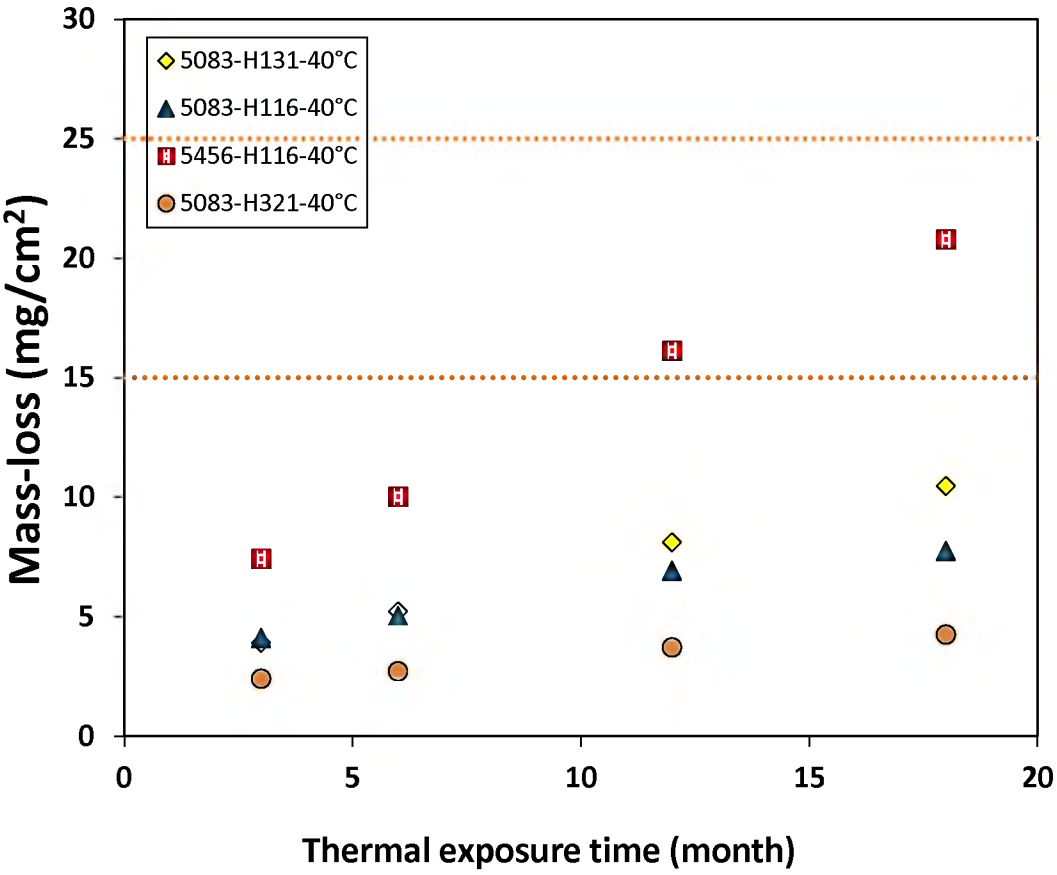

Figure 5.6 ASTM G67 mass-loss tests results of 5083-H131, 5083-H321, 5083-H116, and 5456-H116 alloys as functions of heat treatment times (up to 18 months) at the temperature of 40°C.

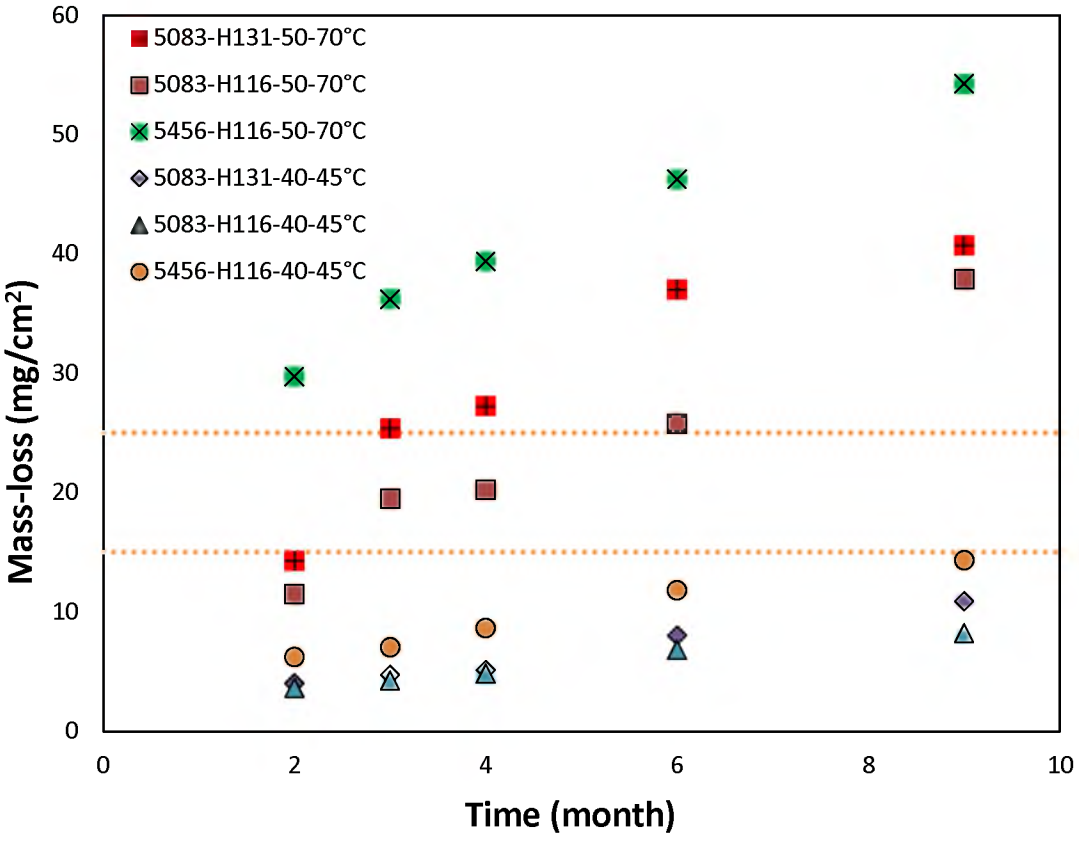

Figure 5.7 ASTM G-67 mass-loss tests results of 5083-H131, 5083-H116, and 5456-H116 alloys as functions of heat treatment time (up to 9 months) and temperature in cyclic thermal exposure.

CHAPTER 6

PRELIMINARY MODELING OF B-PHASE THICKNESS GROWTH

Diffusion rates of Mg are too low to form significant quantities of β-phase at room temperature. However, ships are exposed to temperatures that significantly exceed room temperature (> 40°C) during the hottest part of the day when exposed to warmer climates and sunlight, causing significant magnesium diffusion and sensitization.

A mathematical model has been in development to predict sensitization based on Mg diffusivity parameters. The model follows the fundamental theory of diffusion. The diffusivity parameters obtained in this work can be used in the future to predict β-phase thickness and ASTM G67 corrosion damage for a wide range of thermal exposure time and temperature [107].

The basic assumptions of this model are schematically explained in Figure 6.1. The β-phase nucleation and growth with respect to time is shown in Figure 6.1(a). Mg diffuses out of the bulk (middle of the grain) to form β-phase along the grain boundary, which is shown in Figure 6.1(b). After thermal exposure for a critical time period at a specific temperature level below the solvus line, a continuous/semicontinuous layer of

β-phase gradually forms along the grain boundary facilitating the crack propagation and subsequent material failure. With increase in exposure time, the grain boundary becomes rich in Mg and the region close to it becomes depleted in Mg.

Figure 6.2 shows the Mg concentration profile close to the grain boundary region in a plate-shaped grain, which is in consistent with the EBSD image of grain shape on the LST surface. It is assumed that magnesium diffuses into grain boundaries with an even flux distribution along the entire grain boundary due to rapid diffusion along grain boundaries to β-phase sites. Consequently, a measurement of the average β-phase thickness will give an accurate indication of the magnesium diffusion rate as long as the grain thickness is also considered with a mass balance.

The Mg concentration gradient (C_{bulk} - C_{satd}) is the driving force for diffusion. Diffusion proceeds until the bulk concentration is decreased to the saturation concentration (C_{satd}) at that temperature (C_{satd} is the equilibrium concentration of Mg obtained from the solvus curve of the Al-Mg binary phase diagram). The concentration gradient is a variable quantity and is decreased with time since the bulk is being depleted with Mg with the increase in time. For this, Fick's second law is used to explain the diffusion scenario. The growth rate is solely a function of Mg diffusivity. Effective diffusivity can be measured exactly, once the β-phase thickness (growth rate) is known for a range of thermal exposure times and temperatures. In this work, the β-phase growth rate was measured to estimate the effective Mg diffusivity value. By solving a mass balance equation (increase of Mg along the grain boundary is due to the depletion of Mg

from the bulk), the model can provide β-phase thickness at the grain boundary for a range of thermal exposure times and temperatures. Mg diffusivity can be estimated from this information. Activation energy for Mg diffusion can be obtained by plotting the natural logarithm of diffusivity versus temperature^{-1}. The equations for basic parameters (6.1-6.3) as well as the boundary conditions (6.4-6.6) used for this model are provided in the accompanying equations.

The Mg depleted zone was increased with the increase in thermal exposure time and the depleted Mg accumulated in the grain boundary to form beta phase. This information was utilized to estimate the diffusion coefficient value based on the magnesium mass balance equation (6.7), in which C_{Mg} is the instantaneous Mg concentration in the grain, its expression is given by equation (6.8). The diffusivity parameters were obtained from the mathematical model discussed earlier using the β-phase thickness evaluated experimentally from the high resolution TEM images. Modeling work was initiated based on the parameters (D_o, D_{act}, C_o, *and* C_{act}) obtained from previous work. The β-phase thickness was also estimated theoretically using our mathematical model for the same heat treatment condition. Parametric studies were carried out based on the thickness comparison obtained from theory and experiments and the best possible parameters were fitted in our model to estimate the pre-exponential diffusion coefficient and subsequent prediction for corrosion sensitization.

$$C_{Mg} = f(C_{satd}, D, t, T) \qquad 6.1$$

$$D = D_o \exp(-\frac{Q}{RT}) \quad 6.2$$

$$\frac{\partial C_{Mg}}{\partial t} = D\frac{\partial^2 C_{Mg}}{\partial x^2} \quad 6.3$$

$$\frac{\partial C_{Mid-grain,t}}{\partial x} = 0 \quad 6.4$$

$$C(0,t) = C_{satd} \quad 6.5$$

$$C(x,0) = C_{bulk} \quad 6.6$$

$$(C_{beta} - C_{bulk}) * \frac{thickness}{2} = \int_0^{\text{mid-grain}} (C_{bulk} - C_{Mg}) * dx \quad 6.7$$

$$C(x,t) = \frac{4C_o}{\pi}\sum_{i=0}^{\infty}\frac{1}{2i+1}\sin\frac{(2i+1)\pi x}{h}\exp[-(\frac{(2i+1)\pi}{h})^2 Dt] \quad 6.8$$

where,

C_{bulk} (C_0) is the initial Mg concentration in the bulk;

C_{Mg} is the instantaneous Mg concentration;

C_{beta} is the Mg concentration in β-phase;

C_{satd} is the equilibrium concentration of Mg obtained from the solvus curve of the Al-Mg binary phase diagram;

D is diffusivity value;

D_o is the pre-exponential diffusion coefficient;

T and t are heat treatment temperature and time;

Q is energy barrier for Mg diffusion;

R is the universal gas constant, which is 8.314 $J.mlo^{-1}.K^{-1}$

It is clear that there are several critical parameters which can be obtained from experiments and observations, including grain orientations, initial Mg bulk concentration, final Mg concentration as a function of position, grain size, β-phase thickness, and heat treatment time and temperature. For the determination of these parameters, many amounts of experiments have been performed as mentioned earlier and will be continued in the future for the best determination of these basic parameters and for the subsequent modeling prediction of β-phase thickness and corrosion sensitization.

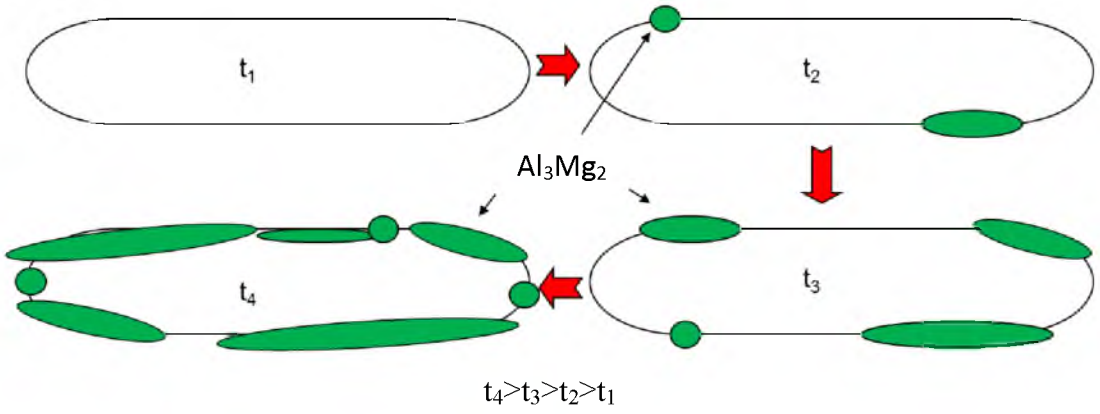

(a)

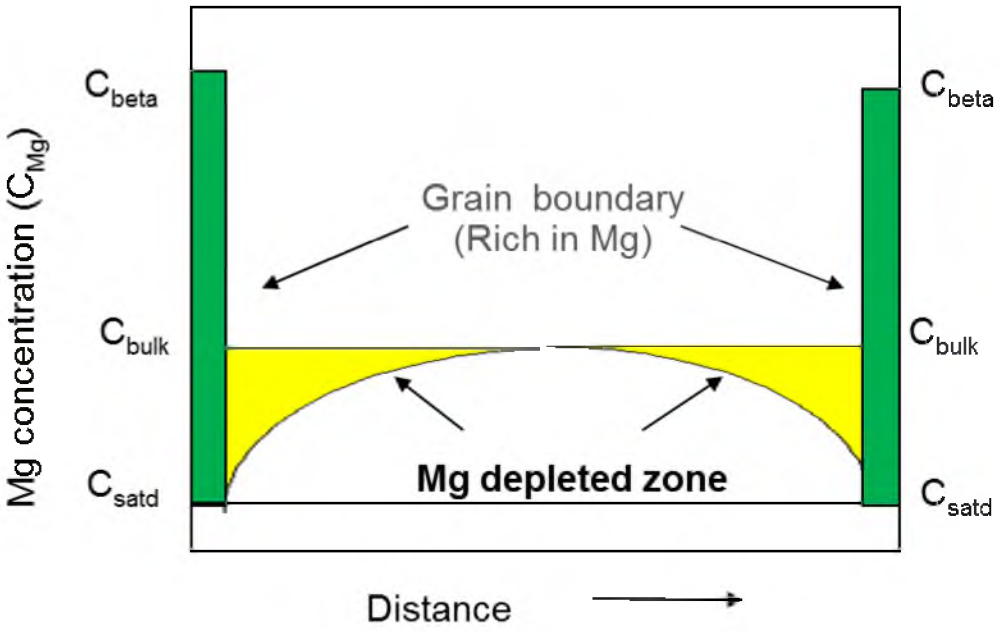

(b)

Figure 6.1 Schematic diagram showing (a) nucleation and growth of beta phase with respect to time; (b) Mg diffusion towards grain boundary from the middle of the grain

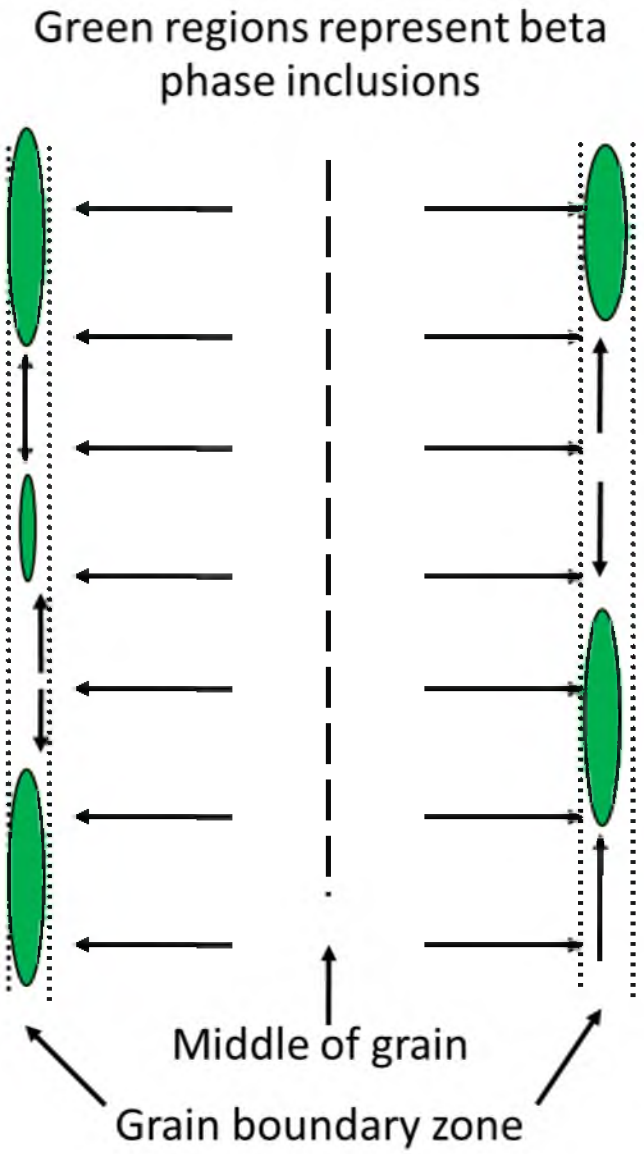

Figure 6.2 Model of Mg distribution profile close to the grain boundary region based on EBSD imaging

CHAPTER 7

CONCLUSIONS

In summary, the present work based on long-term (up to 20,000 hour) thermal exposure testing and ASTM G67 tests of 5083-H131, 5083-H321, 5083-H116, and 5456-H116 at 40°C, 50°C, 60°C, and 70°C provided information of beta phase growth rates and of degree of sensitization as a function of thermal exposure time, temperature, temper of alloys, and alloying elements. Data from extended cyclical (up to 2,500 cycles) testing of 5083-H131, 5083-H321, 5083-H116, 5456-H116 at 45°C and 70°C peak temperatures were performed to determine both beta phase growth rates and ASTM G-67 mass-loss. The precipitation and growth of intergranular and intragranular beta phase was characterized using SEM, TEM, and AFM. Its relationship with pre-existing particles, Al_6Mn, for example, was investigated. Some research work was also performed to evaluate the contribution of dislocations to the beta phase growth. All of the information will allow for reasonable extrapolations to predict sensitization after decades of navy ship service. A summary of accomplishments and conclusions drawn from this work are listed below,

ICP-AES and STEM-EDS measurements gave average Mg concentrations of

4.85 ± 0.05 wt. % and 5.00 ± 0.15 wt. %, respectively. These results indicate that the concentration measurement from these two techniques match well. In addition, our results obtained from EDS quantification reveal that the Al matrix (α-phase) also contains Fe, Mn, and Cr, ranging from 0.5 wt. % to 1.5 wt. %.

Diffusion of Mg is manifested by the thickening of β-phase along the grain boundary because the grain boundary is considered as the preferential site for β-phase nucleation due to the low diffusion barrier.

The β-phase growth rate was monitored using high resolution SEM/TEM. The β-phase thickness was estimated from SEM/TEM images. Basically, the values from both techniques match well.

The variety of precipitates and their subsequent effects on β-phase nucleation and growth kinetics was investigated. Existence of various intermetallic particles was observed in both baseline and thermally exposed (70°C and 175°C) samples. These particles are usually rod shaped or equiaxed, and are rich in Mn, Fe, and Cr. Indexing of lattice planes observed in a few of these particles suggested the composition is Al_6Mn or Al_6(Mn, Fe, Cr). It was found that the β-phase precipitation occurs between the preexisting Mn rich particles based on high resolution TEM imaging.

Dislocation networks were observed to accelerate lengthening and thickening kinetics of intergranular and intragranular allotriomorphs. The thickness of beta phase that is connected to dislocations is higher than that of the beta phase without connection to dislocations.

The β-phase precipitated below 200°C as long as sufficient time had elapsed. However, further investigation into the effect of temperature on phase transformations and intragranular β-phase precipitation is needed, and may be facilitated by more advanced characterization techniques, including *in situ* STEM imaging.

ASTM G67 tests were carried out to quantify the degree of sensitization. Sensitization behavior varies with the variation of thermal exposure time and temperature. Higher mass-loss values were obtained from ASTM G67 tests of 5456 alloys due to its high concentration of Mg compared to 5083 alloys. The nitric acid attack in ASTM G67 tests on TST surfaces and LST surfaces was observed to be greater than that on the LT surfaces.

The basic model for the determination of diffusivity values, the prediction of β-phase thickness growth, and corrosion sensitization prediction was reported by previous work [108]. In the present work, several critical parameters were determined, such as initial Mg bulk concentration is around 5 wt. %, grain size is around 1 um, β-phase thickness determined using TEM listed in Table 4.15, etc. All of these will be used to improve the model.

REFERENCES

1. R.A. Sielski: *Ships and Offshore Structures*, 2008, vol. 65, pp. 57-65.

2. R. Haghayeghi, E.J. Zoqui, and H. Bahai: *J. Alloys Compd.*, 2009, vol. 481, pp. 358-64.

3. S. Kar, A. Rodchanarowan and M.L. Free: *NACE International*, Atlanta, Georgia, 2009.

4. M.C. Carroll, P.I. Gouma, M.J. Mills, G.S. Daehn, and B.R. Dunbar: *Scripta Mater.*, 2000, vol. 42, pp. 335-40.

5. J. S. Vetrano, M. J. Danielson, D. R. Baer, and R. H. Jones: *TMS Annual Meeting*, San Diego, California, 1999.

6. J.L. Searles, P.I. Gouma, and R.G. Buchheit: *Metall. Mater.Trans. A,* 2001, vol. 32, pp. 2859-67.

7. R.H. Jones, D.R. Baer, M.J. Danielson, and J.S. Vetrano: *Metall. Mater. Trans. A*, 2001, vol. 32, pp. 1699-711.

8. M. Liu, P. Schmutz, S. Zanna, A. Seyeux, H. Ardelean, G. Song, A. Atrens, and P. Marcus: *Corr. Sci.,* 2010, vol. 52, pp. 562-78.

9. R.L. Holtz, P.S. Pao, R.A. Bayles, and T.M. Longazel: *DoD Corrosion Conference*, Palm Springs, California, 2011.

10. L. Tan, and T.R. Allen: *Corr. Sci.,* 2010, vol. 52, pp. 548-54.

11. K.A. Yasakar, M.L. Zheludkevich, S.V. Lamaka, and M.G.S. Ferreira: *Electrochim*

Acta, 2007, vol. 52, pp. 7651-59.R. Goswami, G. Spanos, P.S. Pao, and R.L. Holtz: *Mater. Sci. Eng. A*, 2010, vol. 527, pp. 1089-95.

12. E. Sikora, X.J. Wei, and B.A. Shaw: *Corr.,* 2004, vol. 60, pp. 387-98.

13. J. Buczynski, and R.G. Kelly: *DoD Corrosion Conference*, Palm Springs, California, 2011.

14. K. Osamura, and T. Ogura: *Metall. Mater. Trans. A*, 1984, vol. 15, pp. 835-38.

15. M. Bouchear, D. Hamana, and T. Laoui: *Phil. Mag. A*, 1996, vol. 73, pp. 1733-40.

16. P. van Mourik, M.N. Maaswinkel, T.H. de Keijser, and E.J. Mittemeijer: *J. Mater. Sci.*, 1989, vol. 24, pp. 3779-86.

17. S. Nebti, D. Hamana, and G. Cizeron: *Acta. Metall. Mater.*, 1995, vol. 43, pp. 3583-88.

18. J.D. Embury, and R.B. Nicholson: *Acta. Metall.*, 1963, vol. 11, pp. 347-54.

19. G. Itoh, B. Cottereau, and M. Kanno: *Mater. Trans.*, *JIM*, 1991, vol. 31, pp. 1041-49.

20. Standard Specification for High Magnesium Aluminum-Alloy Sheet and Plate for Marine Service and Similar Environments, B928/B928M, *ASTM International*, 2007.

21. J.S. Vetrano, S.M. Bruemmer, L.M. Pawlowski, and I.M. Robertson: *Mater. Sci. Eng. A*, 1997, vol. 238, pp. 101-07.

22. R.B. Niederberger, J.L. Basil, and G.T. Bedford: *Corr.*, 1996, vol. 22, pp. 68-73.

23. Alloy Phase Diagrams, ASM Handbook, *ASM International*, 1992.

24. D.R. Baer, C.F. Windisch, Jr., M.H. Engelhard, M.J. Danielson, R.H. Jones, and J.S. Vetrano: *Journal of Vacuum Science and Technology*, 2000, vol. A18, pp. 131-36.

25. L.I. Kaigorodova: *The Physics of Metals and Metallography*, 1994, vol. 78, pp. 490-96.

26. A.J. Davenport: *Aluminium Alloys, Pts 1 and 2 - Research through Innovation and Technology*, 2006, pp. 641-46.

27. H. Uhlig: *Uhlig's Corrosion Handbook.* 2 ed., John Wiley & Sons, New York, 2000.

28. D.O. Sprowls and R.H. Brown: *NACE International*, Houston, Texas, 1969.

29. A. Dauger, E. K. Boudili, and M. Roth: *Scripta. Metall.,* 1976, vol. 10, pp. 1119-23.

30. R. Nozato, and S. Ishihara: *Trans. Japan. Inst.*, 1980, vol. 21, pp. 580-88.

31. M. Bernole: Master's Thesis, Faculty of Science, University of Rouen, Rouen, Upper Normandy, France, 1974.

32. M. van Rooyen, J. A. Sinte Maartensdijk, and E. J. Mittemeijer: *Metall. Trans.,* 1988, vol. 19A, pp. 2433-43.

33. T. Sato, Y. Kojima, and T. Takahashi: *Metall. Trans.,* 1982, vol. 13A, pp. 1373-75.

34. M. Bernole, J. Raynal, and R. J. Graf: *J. Microscopic*, 1969, vol. 8, pp. 831-40.

35. L. A. Kurtasova, V.M. Polyanskiy: *Phys. Met. Metall,* 1989, vol. 68 (2), pp. 178.

36. N.R.M.R. Bhargava, I. Samajdar, S. Ranganathan, and M.K. Surappa: *Metall. Mater. Trans. A*, 1998, vol. 29A, pp. 2835-42.

37. R.A. Patterson: *Corr.*, 1981, vol. 37, pp. 455-61.

38. Jennifer Louise Searles: Master's Thesis, Ohio State University, Columbus, Ohio, USA, 2000.

39. G. Itoh, B. Cottereau, and M. Kanno: *Mater. Trans. JIM*, 1990, vol. 31, pp. 1041-49.

40. A. Eikum and G. Thomas: *Acta metall.,* 1964, vol. 12, pp. 537-45.

41. R. Goswami, G. Spanos, P.S. Pao, and R.L. Holtz: *Mater. Sci. Eng. A*, 2009, vol. 527, pp. 1089-95.

42. T. Mae, M. Ihara, K. Komura, S. Toriyama, S. Sunada, and K. Arai: *Mater. Trans. JIM*, 1996, vol. 37, pp. 1781-88.

43. H. Yukawa, Y. Murata, M. Morinaga, Y. Takahashi, and H. Yoshida: *Acta Mater.* 1995, vol. 43, pp. 681-88.

44. M. Conserva and M. Leoni: *Metal. Trans. A*, 1975, vol. 6A, pp. 189-95.

45. M. C. Carroll, P. I. Gouma, G. S. Daehn, and M. J. Mills: *Mater. Sci. Eng. A*, 2001, vol. 425, pp. 319-21.

46. M. C. Carroll, R. G. Buchheit, G. S. Daehn, and M. J. Mills: *Mater. Sci. Forum*, 2002, vol. 1443, pp. 396-402.

47. Tsuchida and H. Tanaka: *TMS*, Warrendale, PA5, 1992.

48. Stress Corrosion Cracking: Materials Performance and Evaluation, *ASM International*, Materials Park, Ohio, 1992.

49. Z. Szklarska-Smialowska: *Corr. Sci.,* 1999, vol. 41, pp. 1743-67.

50. M. Pourbaix: *NACE International*, Houston, Texas, 1974.

51. E. H. Hollingsworth and H. Y. Hunsicker: *ASM International*, Materials Park, Ohio, 1987.

52. Y. Yuan: Ph.D Dissertation, University of Birmingham, Birmingham, England, 2005.

53. O. Seri: *Corr. Sci.,* 1991, 36, 1789-1803.

54. G. S. Frankel: *J Electrochem. Soc.,* 1998, vol. 145, pp. 2186-98.

55. N. Birbilis and R. G. Buchheit: *J Electrochem. Soc*., 2005, vol. 152, pp. B140-51.

56. G. S. Frankel and Z. Xia: Corr., 1999, vol. 55, pp. 139-50.

57. K. Nisancioglu: *J Electrochem. Soc*., 1990, vol. 137, pp. 69-77.

58. J. O. Park, C. H. Paik, Y. H. Huang, and R. C. Alkire: *J Electrochem. Soc.,* 1999, vol. 146, pp. 517-23.

59. T. Suter and R. C. Alkire: *J Electrochem. Soc.*, 2001, vol. 148, pp. B36-42.

60. R. G. Buchheit, R. K. Boger, M. C. Carroll, R. M. Leard, C. Paglia, and J. L. Searles: *JOM,* 2001, vol. 53, pp. 29-33.

61. F. Andreatta, H. Terryn, and J. H. W. de Wit: *Electrochim. Acta*, 2004, vol. 49, pp. 2851-62.

62. W. Zhang and G. S. Frankel: *Electrochim. Acta*, 2003, vol. 48, pp. 1193-210.

63. J. R. Flores, C. E. Caicedo-Martinez, O. Steenhaut, H. Terryn, and J. H. W. de Wit: in *3rd International Symposium-Aluminium Surface Science and Technology (ASST 2003) Proceedings*, Bonn, Germany, 2003.

64. E. H. Dix, W. A. Anderson, and M. B. Shumaker: *Corrosion*, 1959, vol. 15, pp. 55-62.

65. W.W. Binger, E.H. Hollingsworth, and D.O. Sprowls: *American Society for Metals*, 1967, vol. 1, pp. 209-76.

66. J. Wloka, and S. Virtanen: *Surface and Interface Analysis*, 2008, vol. 40, pp. 1219-25.

67. N. Birbilis, and R. G. Buchheit: *J Electrochem. Soc.*, 2008, vol. 155, pp. C117-26.

68. Annual Book of ASTM Standards, *ASTM*, Philadelphia, PA, 2002.

69. E. Bumiller and R.G. Kelly: *ECS*, Honolulu, Hawaii, 2008.

70. J. R. Galvele and S. M. de Micheli: *Corr. Sci.,* 1970, vol. 10, pp. 795-807.

71. K. Tohma, Y. Sugai, and Y. Takeuchi: *Japan Insti. Of Light Metals*, 1981, vol. 31, pp. 157-63.

72. M. Stephenson: Master's Thesis, The University of Manchester, Manchester, England, 2000.

73. A. F. Beck and P. R. Sperry: Fundamental Aspects of Stress Corrosion Cracking, *NACE International*, Houston, Texas, 1969.

74. R. Dif and M. Reboul: *EUROCORR*, Trondheim, Norway, 1997.

75. M. O. Speidel and M. V. Hyatt: *Advances in Corrosion Science and Technology*, Plenum Press, New York City, New York, 1972, vol. 2, pp. 115.

76. E. C. W. Perryman and S. E. Hadden: *J Inst. Of Metals*, 1950, vol. 77, pp. 207-15.

77. J. C. Chang and T. H. Chuang: *Metall. Mater. Trans. A,* 1999, vol. 30A, pp. 3191-99.

78. M. Popovic and E. Romhanji: *J Mater. Process. Tech.*, 2002, vol. 275, pp. 125-26.

79. P. Doig and J. W. Edington: *Proc. R. Soc. Lond. A*, 1974, vol. 339, pp. 37-47.

80. R. H. Jones, J. S. Vetrano, and C. F. Windisch, Jr: *Corr.*, 2004, vol. 60, pp. 1144-54.

81. R. Dif, T. Warner, and G. M. Raynaud: *6th International Conference on Aluminium Alloys,* Toyohashi, Japan, 1998.

82. N. J. H. Holroyd: Environment-Induced cracking of Metals, *NACE International*, Houston, Texas, 1990.

83. M. O. Speidel: *Metall. Trans. A*, 1975, vol. 6A, pp. 631-51.

84. T. D. Burleigh: *Corr.*, 1991, vol. 47, pp. 89-98.

85. T. Magnin: *Mater. Sci. Forum*, 1996, vol. 83, pp. 217-22.

86. X. Y. Liu, G. S. Frankel, B. Zoofan, and S. I. Rokhlin: *Corr. Sci.*, 2004, vol. 46, pp. 405-25.

87. W. Gruhl, and Z. Metallkde: *Corr. Sci.,* 1984, vol. 75, pp. 819-26.

88. E. N. Pugh: *Corr.*, 1985, vol. 41, pp. 517-26.

89. R. G. Song, W. Dietzel, B. J. Zhang, W. J. Liu, M. K. Tseng, and A. Atrens: *Acta Mater.*, 2004, vol. 52, pp. 4727-43.

90. R. G. Newman: Marcel Dekker, Inc., New York City, New York, 1995, pp. 311.

91. B. Phull: in ASM Handbook: Corrosion: Fundamentals, Testing and Protection, *ASM International*, Materials Park, Ohio, 2003.

92. A. Turnbull: *Br. Corros. J.,* 1992, vol. 27, pp. 27–35.

93. K. Mizuno, A. Nylund, and I. Olefjord: *Corr. Sci.*, 2001, vol. 43, pp. 381-96.

94. A. Perovic, D. D. Perovic, G. C. Weatherly, and D. J. Lloyd: *Scripta Mater.*, 1999, vol. 41, pp. 703–08.

95. D.A. Porter, and K.E. Easterling: *Phase Transformations in Metals and Alloys*, third ed., CRC press, New York City, New York, 2008.

96. J.R. Bradley, J.M. Rigsbee, and H.I. Aaronson: *Metal. Mater. Trans. A*, 1997, vol. 8, pp. 323-33.

97. R. Birringer, and P. Zimmer: *Acta Mater.*, 2009, vol. 57, pp. 1703-16.

98. P. Zimmer, and R. Birringer: *Appl. Phys. Lett.*, 2008, vol. 92, pp. 081912.

99. R. Birringer, M. Hoffmann, and P. Zimmer: *Phys. Rev. Lett.*, 2002, vol. 88, pp. 206104.

100. J.M. Zuo, and J.C. Mabon: *Microsc. Microanal.*, 2004, vol. 10, pp. 1000-01.

101. M.J. Starink and A.M. Zahra: *Acta Mater.,* 1998, vol. 46, pp. 3381-97.

102. H. L. Jr. Craig*: ASTM STP 516, ASTM*, 1972, vol. 17.

103. Y. Zhu, S. Kar, M. L. Free, K. Prisbrey: *DoD Corrosion Conference*, Palm Spring, California, 2011.

104. Y. Zhu, D. A. Cullen, S. Kar, M. L. Free, L. F. Allard: *NACE International Corrosion Conference*, Salt Lake City, Utah, 2012.

105. Y. Zhu, D. A. Cullen, S. Kar, M. L. Free, L. F. Allard: *Metal . Mater. Trans. A*, August, 2012, published online.

106. D. Sampath, S. Moldenhauer, H.R. Schipper, K. Mechsner, and A. Haszler: *Mater Sci. Forum*, 2000, pp. 331-37, pp. 1089-94.

107. S. Kar: Ph.D. Dissertation, The University of Utah, Salt Lake City, Utah, USA, 2012.